OBSERVATIONS AND MODELING OF PLASMA FLOWS DRIVEN BY SOLAR FLARES

by

Sean Robert Brannon

A dissertation submitted in partial fulfillment
of the requirements for the degree

of

Doctor of Philosophy

in

Physics

MONTANA STATE UNIVERSITY
Bozeman, Montana

January 2016

©COPYRIGHT

by

Sean Robert Brannon

2016

All Rights Reserved

DEDICATION

To Molly Catherine Arrandale.

ACKNOWLEDGEMENTS

I would like to begin by thanking my academic advisor and committee chair, Prof. Dana Longcope. His knowledge of physics is without peer, and he was kind enough to patiently bestow his time and advice to me time and again as I hammered my way painfully through this process. I would also like to extend my gratitude to my graduate committee, especially Profs. David McKenzie and Charles Kankelborg for their invaluable support along the way and for listening when I had concerns. Of course, I must thank the MSU Department of Physics and the MSU Solar Group, for providing me with a community of peers to whom I could always turn when I needed help. I am forever indebted to all of the staff who have tirelessly worked to shield me from the horrors of bureaucracy; this goes double for Margaret Jarrett, who was always there for me with a kind heart and sound advice when I didn't know where else to turn. My family, especially Mom and Dad, who always encouraged me along the way even when they had no idea what solar physics is. All of my friends and classmates, especially Ritoban and Nickolas, who made physics fun even as we complained about it. And finally, most importantly, to my fiancé Molly: you are the love of my life, my confidant, and my best friend. I look forward every day to our journey together, and to whatever life brings us next.

TABLE OF CONTENTS

1. INTRODUCTION 1

Overture 1
Structuring in the Solar Atmosphere 5
Evolution of a Solar Flare 11
Plasma Flows Driven by Solar Flares 18
The Narrative of My Story 26

2. MODELING PROPERTIES OF CHROMOSPHERIC EVAPORATION DRIVEN BY THERMAL CONDUCTION FRONTS FROM RECONNECTION SHOCKS 30

Contribution of Authors and Co–Authors 30
Manuscript Information Page 31
Introduction 32
Flare Loop Model 37
Simulation Setup 41
1-D Fluid Equations 41
Numerical Integration 43
Viscosity and Conductivity 45
Initial Loop Atmosphere 48
Initial Piston Shock 51
Simulation Results 53
Hydrodynamics 53
Differential Emission Measure 61
Synthetic Doppler Velocities 64
Observational Data Fit 70
Scaling Laws 73
Discussion 79
Acknowledgements 86

3. SPECTROSCOPIC OBSERVATIONS OF EVOLVING FLARE RIBBON SUBSTRUCTURE SUGGESTING ORIGIN IN CURRENT SHEET WAVES 87

Contribution of Authors and Co–Authors 87
Manuscript Information Page 88
Introduction 89
Observation 94
Instrument 94
Flare 95

TABLE OF CONTENTS – CONTINUED

Wavelength Correction 100
Results 102
Ribbon Evolution 102
Spectral Line Fitting 107
Doppler Velocities 113
Additional Spectral Lines 115
East Ribbon 118
Interpretation 121
Discussion 129
Acknowledgements 136

4. OBSERVATIONS OF PSEUDO-BALLISTIC DOWNFLOWS IN A M-CLASS FLARE WITH THE INTERFACE REGION IMAGING SPECTROGRAPH 137

Contribution of Authors and Co–Authors 137
Manuscript Information Page 138
Introduction 139
Instrument 144
Flare Details 145
Results 151
Flare Evolution 151
Spectral Intensity Evolution 156
Doppler Velocities and Line Widths 159
Plasma Density 165
Cooling Time 168
Synthetic Spectra 171
Discussion 176
Acknowledgements 182

5. DISCUSSION 183

REFERENCES CITED 190

LIST OF TABLES

Table Page

2.1. Simulation labels and properties. 75

LIST OF FIGURES

Figure Page

1.1. Large-scale structuring of the solar atmosphere 6

1.2. Small-scale structuring of the solar atmosphere 9

1.3. Schematic diagram of a solar flare 13

2.1. Schematic diagram of shock tube model 39

2.2. Artificial loop atmosphere 50

2.3. Hydrodynamic simulation evolution 55

2.4. Conductive-to-freestreaming flux ratio 60

2.5. Differential emission measure evolution 62

2.6. Flow velocity and synthetic Doppler velocity 66

2.7. Evolution of the flow reversal point 69

2.8. Fit to observational data 71

2.9. Results of parameter survey 77

3.1. SDO/AIA 1600 Å image of the flare ribbons 96

3.2. SDO/HMI magnetogram of the flare active region 98

3.3. SDO/AIA 171 Å image of the post-flare loops and ribbons 99

3.4. IRIS SJI 1400 Å image of the flare ribbons 101

3.5. Time series of SJI 1400 Å images 103

3.6. Time-distance stack plots of intensity evolution 106

LIST OF FIGURES – CONTINUED

Figure Page

3.7. Selected spectral plots 109

3.8. Time-distance stack plot of Doppler velocity evolution 114

3.9. Time slices of Doppler velocities 116

3.10. Intensity stack plots for East Ribbon 119

3.11. Phase portrait of sawtooth velocity and position 122

3.12. Schematic diagram of proposed scenario 126

4.1. HMI context magnetogram of AR 12297 before flare 147

4.2. AIA 1600 Å context image of AR 12297 during flare 148

4.3. AIA 171 Å context image of AR 12297 after flare 149

4.4. IRIS SJI 1400 Å context image during flare 150

4.5. Time series of IRIS SJI and SG images 153

4.6. Time-distance stack plots for Fe XXI and Si IV intensity 157

4.7. Spectra from representative pixels within the bullet 161

4.8. Time-distance stack plots for Doppler velocity and NTB 163

4.9. Time-distance stack plot for O IV density analysis 166

4.10. Synthetic spectral Doppler shifts 173

ABSTRACT

One of the fundamental statements that can be made about the solar atmosphere is that it is structured. This structuring is generally believed to be the result of both the arrangement of the magnetic field in the corona and the distribution of plasma along magnetic loops. The standard model of solar flares involves plasma transported into coronal loops via a process known as chromospheric evaporation, and the resulting evolution of the flare loops is believed to be sensitive to the physical mechanism of energy input into the chromosphere by the flare. We present here the results of three investigations into chromospheric plasma flows driven by solar flare energy release and transport. First, we develop a 1-D hydrodynamic code to simulate the response of a simplified model chromosphere to energy input via thermal conduction from reconnection-driven shocks. We use the results from a set of simulations spanning a parameter space in both shock speed and chromospheric-to-coronal temperature ratio to infer power-law relationships between these quantities and observable evaporation properties. Second, we use imaging and spectral observations of a quasi-periodic oscillation of a flare ribbon to determine the phase relationship between Doppler shifts of the ribbon plasma and the oscillation. The phase difference we find leads us to suggest an origin in a current sheet instability. Finally, we use imaging and spectral data of an on-disk flare event and resulting flare loop plasma flows to generally validate the standard picture of flare loop evolution, including evaporation, cooling time, and draining downflows, and we use a simple free-fall model to produce the first direct comparison between observed and synthetic downflow spectra.

1. INTRODUCTION

"How shining in itself must have been that which was within the Sun as I entered it, showing not by color but by light! Were I to summon genius and skill and practice I should never tell of it so that it might be imagined, but we can believe it, and let us long for the sight; and if our imagination is too low for such a height it is no wonder, for never did eye see light greater than the Sun."

— Dante Alighieri, *Paradiso* (Canto X)

Trans. John D. Sinclair

1.1. Overture

The Sun has been a central character in the stories humanity has told since long before the dawn of written histories. Ancient peoples were well aware of the importance of the Sun to the existence of life, and of its power in influencing human affairs. In antiquity, the Sun was often cast in a religious role as a god, or at least as an object or vehicle controlled by a god. In the ancient Egyptian culture, for example, Sun worship was ubiquitous; multiple religious traditions existed there, including that the Sun was the visible manifestation of the god Ra (most usually his body or eye) and that the god of creation, Amun, lived within it. The earliest Greeks referred to the Sun as Helios, believing it to be the chariot of the god Apollo; the Romans later took this tradition, renaming it Sol Invictus ("Unconquered Sun"). Even in modern

day Abrahamic religions, the Sun plays an important role in the driving away of evil and as a symbol of the power of God (as in the above quote from Dante). Nor was Sun worship restricted to Europe: the Chinese, the Aztecs, Hindus, and Buddhists all have their own stories about the creation of the Sun, its position within the cosmos, and its relationship to humanity.

The study of the Sun as a secular astronomical object, however, is much more recent. The first description of the Sun in a non-religious manner can be attributed to the Greek philosopher Anaxagoras in the fifth century BCE, who believed that the Sun was an enormous ball of flaming metal. (Our understanding has improved somewhat since then.) Two hundred years later another Greek, Eratosthenes, used geometry to estimated the distance from the Earth to the Sun; the result was unfortunately written somewhat ambiguously, referring to "of stadia myriads 400 and 80000" where a myriad is 10,000 and which could therefore translate to either 4,080,000 stadia (750,000 km) or 804,000,000 stadia (just over 150 million kilometers). Were it the latter distance that he meant, he would have been very nearly correct: the currently accepted value for the mean distance of the Sun from the Earth is 149.6 million kilometers.

Around that same time, Aristarchus of Samos proposed the first recorded *helio-centric* model of the Solar system, in which the planets (including Earth) revolve around the Sun instead of around the Earth. A century later, however, Ptolemy

would incorrectly supplant both of these ideas: his estimate for the solar distance was twenty times too small, and his now infamous *geocentric* model (known as the Ptolomaic system) of planetary motion held sway for another 1,500 years. In Europe, at least, it was only after the scientific enlightenments of Copernicus and Kepler and Newton in the 16th and 17th centuries CE that the Earth was displaced as the center of planetary motion and the Sun ushered into its rightful place in the Solar System.

And so it remains. As we now know, the Sun is indeed the dominant object in the Solar System. Moreover, it is not as serene of an object as its apparently featureless, white disk in the sky would have us believe. In fact, even that visible surface, known as the *photosphere*, is not without interest: giant sunspots, larger as the Earth, appear and disintegrate over the course of days. The region above the photosphere is not quiet either. Magnetic fields, visible as great arcing loops filled with million degree plasma, erupt through the surface and twist, break, and snap back down. As these fields break and reconnect, they release tremendous amounts of stored energy in the form of enormous explosions called solar flares. A flare can release as much energy over its hour-long life as all of the human species currently would use in a thousand years. These flares are also connected to ejections of plasma away from the Sun, which stream out into the Solar System and have profound implications for human civilization and space exploration.

The entirety of solar physics is far too large a field to contemplate covering in a single doctoral-level dissertation. Even the rather more narrow topic of solar flares has many branches and avenues of research which, although related, are far beyond our purpose and scope here. But to answer any great question requires first the answering of many small questions, and for that reason we therefore focus our investigations on a seemingly insignificant slice of solar physics which we have suggested in our title: "Observations and modeling of plasma flows driven by solar flares". We will therefore not dwell overlong on the mechanisms by which solar flares occur, or how the magnetic fields came to be in the configuration they are in, or how the solar atmosphere is organized. Instead, we will narrow our focus to just the subsequent consequences for the flare loop plasma: how it is heated and accelerated and the properties of the flows that develop, how the plasma in the chromosphere can be used to determine properties and motions in the coronal, and how the loop plasma evolves during the immediate aftermath of a flare.

In the remaining sections of this Introduction, we will briefly discuss the theoretical and observational underpinnings for this research. We will begin in Section 1.2 with a brief discussion of the structuring of the solar atmosphere and the primary mechanisms responsible for it. Next, in Section 1.3, we will present an overview of the standard model for solar flare evolution, from magnetic reconnection and flare loop formation to the loop filling and draining process. Finally, in Section 1.4, we

will review key historical results, both observational and computational, in the topic of flare-driven plasma flows. At the end of the Introduction, in Section 1.5, we will briefly summarize the following four chapters of this dissertation.

1.2. Structuring in the Solar Atmosphere

One of the fundamental statements that can be made about the solar atmosphere is that it is *structured*. To the lowest order of approximation, it is useful to consider the structure of the solar atmosphere as a series of concentric spherical shells, with the density generally decreasing with height (due to gravitational stratification) and the temperature generally increasing with height (due to heating mechanisms which are not fully understood) (Aschwanden, 2005). In order of ascending height, these layers are referred to as the *photosphere*, the *chromosphere*, the *transition region*, and the solar *corona*.

The coolest layer is the photosphere, captured in visible light in Figure 1.1(a) by the *Atmospheric Imaging Assembly* (AIA) on board the *Solar Dynamics Observatory* (SDO) satellite. The photosphere is the visible surface of the Sun, and is the source of the visible continuum spectrum at a temperature of ∼5,800 K. A precise location is assigned to the photosphere from the origin of the continuum at 5,500 K. Above lies the chromosphere, captured in Figure 1.1(c) by SDO/AIA in 304 Å He II emission, is ∼2,000 km thick, has an average density of $\sim 10^{11}$ cm^{-3}, and varies in temperature

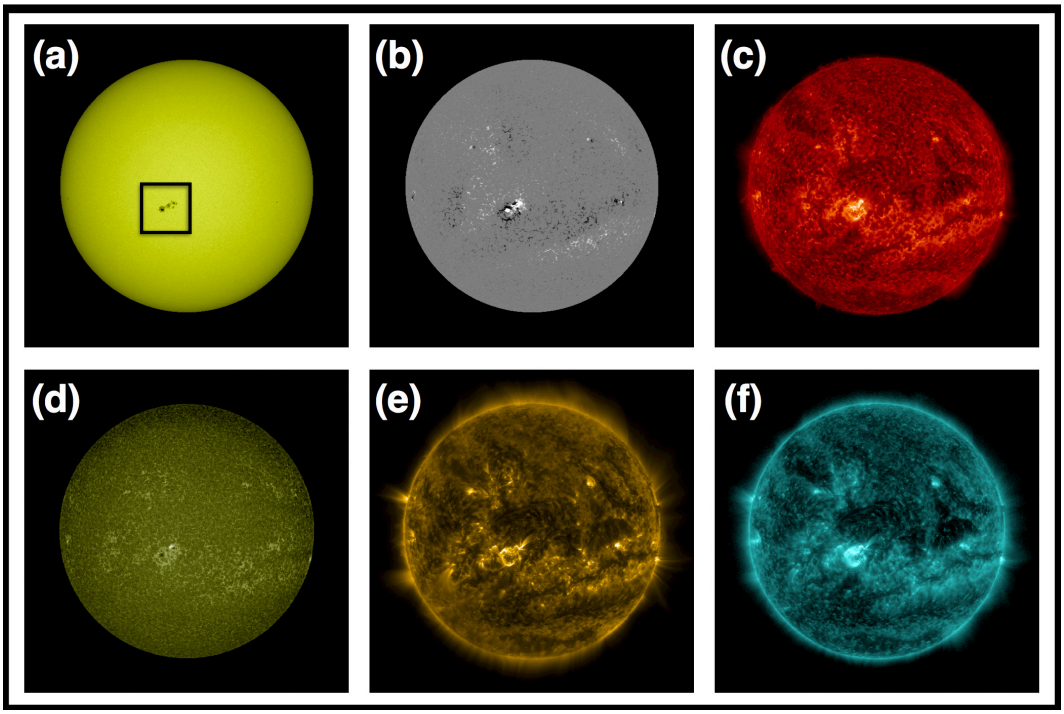


Figure 1.1. Images of the Sun in different wavelengths, taken by the SDO/AIA and SDO/HMI instruments. Panel (a) the photosphere (6,000 K) in visible light; (b) the line-of-sight magnetic field at the photosphere; (c) the chromosphere in 304 Å (He II, 50,000 K); (d) the transition region in 1600 Å (C IV, 100,000 K); (e) the ambient corona in 171 Å (Fe IX, 1 MK); (f) the ambient and flaring corona in 131 Å (Fe VIII, 0.5 MK; Fe XX, 10 MK; Fe XXIII, 16 MK). Inset box in Panel (a) indicates zoom region for Figure 1.2, centered on an active region.

from ∼5,000 K (slightly lower than the photosphere) to over 20,000 K (Vernazza et al., 1981; Fontenla et al., 1990). Next, there is a very thin (<200 km) layer where the plasma temperature increases rapidly from the chromospheric temperature of ∼10,000 K to nearly 1,000,000 K (1 MK) (Vernazza et al., 1981; Fontenla et al., 1990). The plasma density, meanwhile, falls by an equal amount to $\sim 10^9$ cm^{-3}. This is the transition region (TR), shown in Figure 1.1(d) in 1600 Å C IV emission (∼ 100,000 K)

from SDO/AIA. Together, the chromosphere and the transition region are sometimes referred to as the *interface region*, and are a rich source of far-ultraviolet (FUV) and extreme-ultraviolet (EUV) spectral emission lines which carry information concerning the plasma conditions there (De Pontieu et al., 2014). Finally, the outermost layer is the corona, which consists of a very hot (>1 MK), tenuous plasma extending outward to several solar radii before transitioning into the outward flowing solar wind. In Figure 1.1(e), we see the 1 MK ambient component of the corona can be seen in 171 Å (Fe IX), and in Figure 1.1(f) a combination of the ∼0.5 MK (Fe VIII) ambient and the superheated 10-16 MK (Fe XX and Fe XXIII) flaring components of the corona in 131 Å emission.

Even a cursory inspection of Figure 1.1, however, reveals that the solar atmosphere is nowhere near as homogeneous as the concentric-shell model we have outlined above would suggest. The black box in Figure 1.1(a) indicates one such inhomogeneity: a *sunspot* group located near disk center. Comparing this location across the different wavelengths (and plasma temperatures) in Figure 1.1(c)–(f) shows that the sunspot group is correlated with a patch of bright emission, especially in 304 Å, 171 Å, and 131 Å. These bright patches, known as *active regions*, are places of intense activity and are often correlated with explosive events called *solar flares* (we will discuss flares in more detail in Section 1.3).

It is commonly understood that the entire solar atmosphere is threaded with magnetic fields. In Figure 1.1(b) we display the line-of-sight (LOS) magnetic field magnitude measured by the *Helioseismic and Magnetic Imager* (HMI) on board SDO; in this image white (black) represents magnetic field pointed towards (away from) the instrument. As we can see, the active region indicated by the black box corresponds to a patch of strongly dipolar magnetic field. Although we will not discuss it further in this dissertation, active regions are locations where the magnetic field may become significantly distorted away from its equilibrium state, known as a *potential field*. The result of this non-potential field is the storage of free magnetic energy which, when released suddenly, may result in solar flares (Tarr, 2013).

Further structuring of the atmosphere also appears on smaller scales within active regions. In Figure 1.2(a)–(f) we show the same six images for the black zoom box indicated in 1.1. In these images, particularly Panels (e) (171 Å) and (f) (131 Å), we see large arcs of bright plasma which loop from one magnetic polarity to the other. These are known as *coronal loops*, and they form the basic unit of coronal structuring in the solar atmosphere (Aschwanden, 2005). It is obvious from an inspection of these images that coronal loops display a wide variety of different behaviors. First, loops appear grouped into "families", which all begin and end in roughly the same magnetic polarity and typically share a similar size and shape. Different families of loops display will generally display very different properties. However, even within

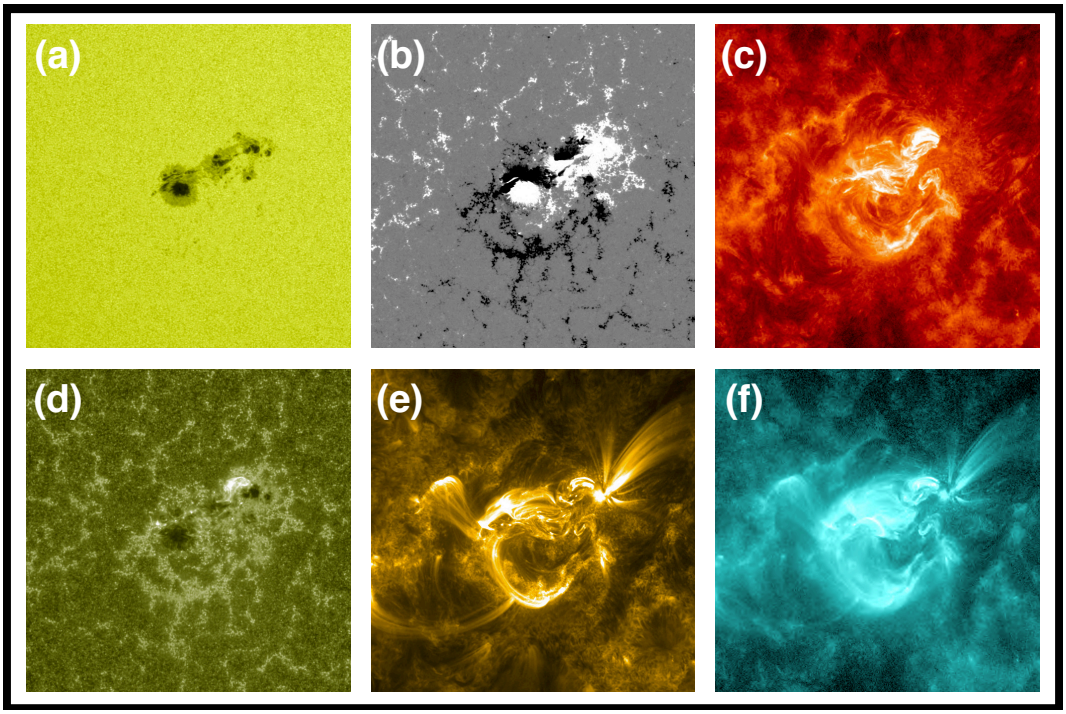


Figure 1.2. Same as Figure 1.1, for zoom region indicated in Panel (a).

a family of loops there are often significant differences in the properties of adjacent loops.

On this scale, the magnetic fields also play an important role in creating structuring. First, it is generally believed that the coronal loops we observe in Figure 1.2 are often produced when magnetic fields in an active region undergo a large-scale restructuring (a process known as *reconnection*) to produce new loops of magnetic field with different connectivity. The energy released in the restructuring is thought to be responsible for the brightness of the loops in the various wavelengths shown in Figure

1.2. This same process also releases energy to drive solar flares. Second, in a magnetic field a plasma is subject to two different sources of pressure: the ordinary gas dynamic pressure p_g which may act in all three dimensions and a magnetic pressure p_m which only acts perpendicular to the magnetic field B. The relative importance of these two pressures to the evolution of the plasma is described by the *plasma-β* parameter, given by

$$\beta = \frac{8\pi p}{B^2}. \tag{1.1}$$

Throughout much of the portion of the solar atmosphere relevant for coronal loops (including the upper chromosphere, TR, and lower corona), $\beta \ll 1$ (Gary, 2001). In this *low-β* regime, the ionized particles are generally confined to move only along the field lines, meaning that the plasma is trapped by the magnetic field to appear on the loops formed during reconnection.

Although the dominant nature of the magnetic field in the solar atmosphere explains why the plasma appears structured into bright loops along the magnetic field lines, it does not address the mechanisms by which plasma is located along the loops in the first place. The radiative intensity of a given ion species in a plasma is proportional to the number density of ions and electrons in the plasma, given by

$$I \propto n_i n_e \sim n_e^2 \tag{1.2}$$

where in the second relation we have assumed that the plasma is electrically neutral (the *quasineutrality* condition, generally valid in the near-perfect electrical conductivity in the solar corona). Thus, the radiative intensity of the solar atmosphere, and hence the appearance of structures like coronal loops, is strongly dependent on the spatial distribution of the plasma. A central question of solar coronal physics is therefore the following: *what mechanisms are responsible for filling coronal loops with plasma and creating the different loop plasma distributions that we observe?* This question leads us to examine in more detail the explosive energy releases known as solar flares.

1.3. Evolution of a Solar Flare

Solar flares are among the most energetic explosive events that occur within the Solar System, and have a profound impact on the local space environment within which the Earth resides. The first recorded example of a solar flare was on September 1st 1859, and was independently observed in England by Richard C. Carrington and Richard Hodgson (Carrington, 1859; Hodgson, 1859). The Carrington flare (as it is now referred to) was the prototypical example of a class of flares known as "white-light" flares, meaning that it was large enough to measurably enhance the Sun's emission in the visible part of the spectrum. It is now understood that the vast majority of solar flares are significantly smaller than the Carrington flare. For several decades,

observations of solar flares were performed primarily using the chromospheric Hα spectral line, and were thus understood as a chromospheric phenomenon. With the advent of space-based X-ray and ultraviolet (UV) observational instruments, it was discovered that flares emit the majority of their radiative energy in high-temperature (>1 MK) spectral lines, and the understanding of flares as coronal events began to develop.

The standard picture of the evolution of a solar flare begins with the reconnection of magnetic field lines in the corona (Carmichael, 1964; Sturrock, 1966; Hirayama, 1974; Kopp & Pneumann, 1976), forming a series of flare loops. A schematic diagram of this process is shown in Figure 1.3 (reprinted from Lin & Forbes (2000)). Once reconnected, the loops are then free to retract at the Alfvén speed, compressing and heating the plasma to several tens of MK near the loop tops (Semenov et al., 1998; Longcope et al., 2009). The energy released during this process is generally thought to be transported down the flux tube from the reconnection site by some combination of non-thermal electron beams (Brown, 1973) and thermal conduction (Craig & McClymont, 1976; Forbes et al., 1989). Whatever the mechanism, once the energy reaches the transition region (TR) and chromosphere at the flare loop footpoints it becomes deposited in the cool dense plasma located there, heating it and resulting in an over pressure which drives upflows known as *chromospheric evaporation* (Sturrock, 1973). The evaporated chromosphere plasma, which is now at flare temperatures, fills

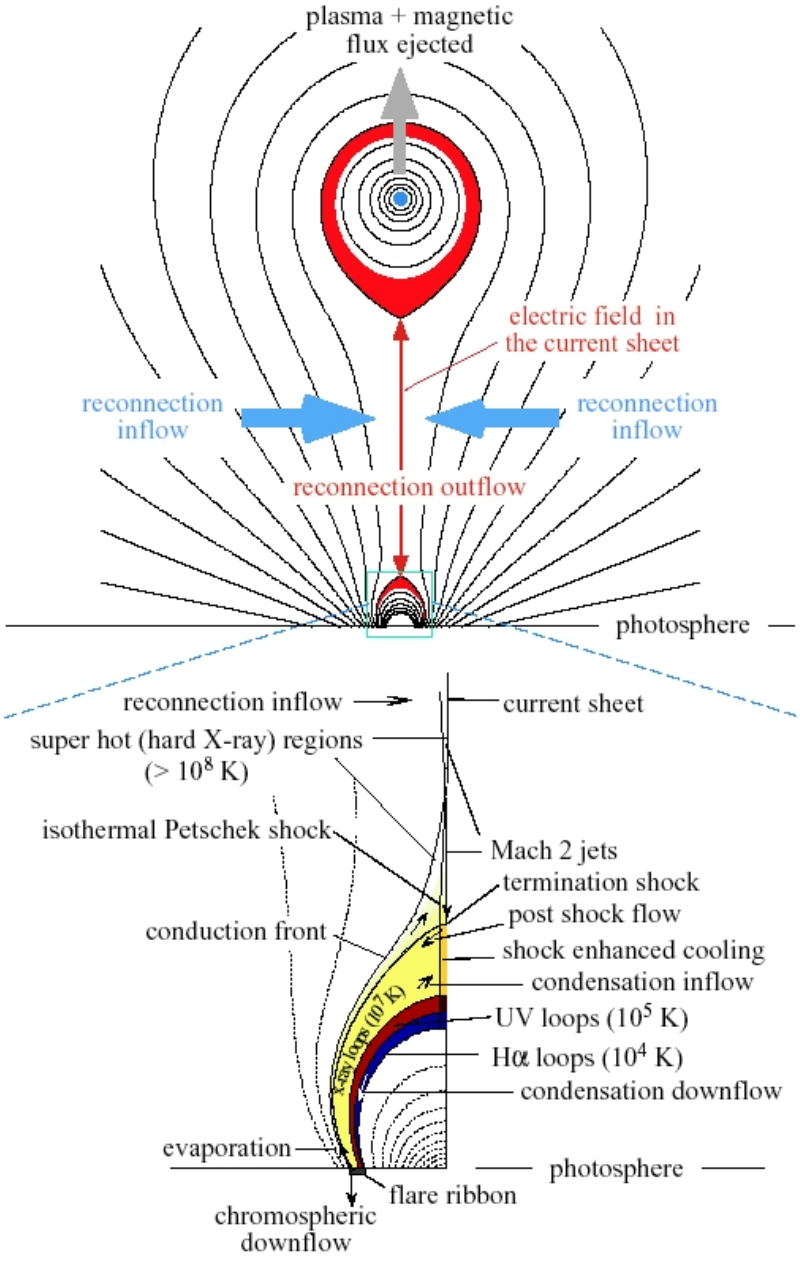


Figure 1.3. Schematic diagram of a solar flare. Reprinted from Lin & Forbes (2000).

the loop from one or both foot points and results in the loop appearing bright in hot coronal spectral lines.

The exact details of the reconnection process are still not thoroughly understood on a theoretical level, and there does not yet exist any analytical solution for steady reconnection in the solar corona during a flare using the magnetohydrodynamic equations including resistivity. However, there are several partially competing models that have been proposed, which assume some substantial simplifications. The first of these is *Sweet-Parker reconnection*, first proposed by Sweet (1958) and later modified and extended by Parker (1963a). This model assumes that the reconnection region is much longer than it is thick, as shown by the red arrowed line in the upper diagram in Figure 1.3 (adapted and reprinted from Lin & Forbes (2000)). After some additional approximations, the Sweet-Parker model predicts an energy dissipation rate that is on the order of 10^{22}-10^{24} erg s^{-1}, which is significantly smaller than the 10^{26}-10^{31} erg s^{-1} observed in actual flares.

Another proposed reconnection model, *Petschek reconnection* (Petschek, 1964), somewhat alleviates this issue by assuming that the reconnection region dimensions are approximately the same (such that the red arrowed line in Figure 1.3 would instead be a small box), resulting in a reconnection and energy dissipation rate about 1,000 times greater than for Sweet-Parker. This begins to approximate the range for weaker flares but is still significantly slower than is expected for larger events.

Several proposed mechanisms exist to posit an accelerated reconnection process, most of which attempt to break up the extended Sweet-Parker current sheet into numerous smaller Petschek-style reconnection sites. These include so-called "impulsive bursty" reconnection models (Priest, 1985), which depend on an plasma instability such as the *tearing mode* instability (Furth et al., 1963) to break up the current sheet (see, e.g., Kliem et al. (2000)).

Regardless of the exact details of the reconnection, what is clear from the observations is the aftermath. As shown in the inset box and lower diagram in Figure 1.3, the freshly reconnected field lines form loops. The endpoints of the loops are referred to as the loop *footpoints*, and the entire set of reconnected loops is known as the *flare arcade* (Priest, 1982). The plasma at the very top of the loop has already been heated to very high ($>10^7$ K) temperatures by resistivity in the reconnection region, generating non-thermal electrons (NTEs) and a hard X-ray source at the loop top (Aschwanden, 2005). When the loop first forms it is not in mechanical equilibrium, but rather experiences magnetic tension which causes it to snap down much like a rubber band (Semenov et al., 1998; Longcope et al., 2009). In Longcope et al. (2009) the authors showed that the contracting loop actually releases more energy than the initial reconnection, and that this energy goes into heating, compressing, and accelerating the loop plasma by means of slow magnetosonic shocks.

The plasma at the loop top is now very hot ($>10^7$ K) and appears in the high-temperature channels such as 131 Å. There is thus a substantial temperature gradient between the hot post-shock plasma at the top of the loop and the much cooler ($\sim 10^6$ K) ambient coronal plasma that was already in the loop. This temperature gradient results in a *thermal conduction front* (TCF; Craig & McClymont, 1976; Forbes et al., 1989; Tsuneta, 1996) which propagates down the loop (Figure 1.3) towards the loop footpoints. Generally, the magnetic pressure of a flaring loop dominates over the plasma pressure (the low plasma-β regime; Gary, 2001), and thus the TCF is confined to move only along the field lines and not perpendicular to it. Also confined to the loop are the NTEs generated by the reconnection; these are therefore referred to as *NTE beams* (Brown, 1973). The net result of these two energy transport mechanisms is to move the energy generated near the flaring loop top by the reconnection and contraction shocks down the field lines towards the loop footpoints.

We recall that below the corona lies the chromosphere, which is nearly two orders of magnitude cooler and denser than the overlying coronal region of the loop. The footpoints of the loops are thus anchored in the denser plasma of the chromosphere, which acts as a mass reservoir for the loop. Within a second or less after the flare loop forms, the energy being transported by the TCFs and NTEs becomes deposited in the upper chromosphere and transition region. Although the density at the footpoints does not change, the plasma is heated to several MK nearly instantaneously. This

results in a significant overpressure developing in the transition region and upper chromosphere, and is responsible for driving flows of the heated dense plasma upward into the loop and downward (via momentum balance) into the lower chromosphere (Fisher, 1987) as shown in Figure 1.3. Historically, the upflows have been referred to as *chromospheric evaporation* (Sturrock, 1973) and the downflows as *chromospheric condensation* (Fisher, 1989); however, these processes in reality have little to do with the commonly understood definitions of "evaporation" or "condensation" in terms of phase transitions.

The evaporation/condensation process results in two important observational features of the solar flare. The first are the flare ribbons (Forbes & Priest, 1984) located at the loop footpoints as noted in Figure 1.3. These bright bands which appear in the chromosphere during a flare are generally understood to be energized footpoint plasma which has been heated and compressed by the downflowing condensation front. Meanwhile, the evaporation upflows are moving heated plasma upward away from the chromosphere and into the upper portion of the flare loop. This process, along with the compressed post-shock plasma at the loop top, eventually results in the loop becoming filled with hot ($>10^6$ K) and dense ($>10^{10}$ cm^{-3}) plasma, and creates the bright EUV and X-ray flare loop in coronal temperature channels. Later, as this plasma cools through a combination of conductive, radiative, and enthalpy flux losses (Antiochos & Sturrock, 1978; Antiochos, 1980; Bradshaw & Cargill, 2010), the

loop is observed to transition from higher temperature channels to lower temperature channels. The thermal loss results in the loop plasma losing pressure support and beginning to fall back down towards the chromosphere, a process known as *coronal rain* (Foukal, 1978). Eventually, the loop drains and disappears altogether.

1.4. Plasma Flows Driven by Solar Flares

As we have previously discussed, the properties of the plasma flows induced during a solar flare crucially determine the subsequent evolution and appearance of the flare loop. In the last three decades, significant effort has been dedicated to investigating the physical characteristics of the plasma flows which are induced by solar flares. The primary goal of this endeavor has been to understand both the direct and indirect effects of flare energy release on the solar atmosphere. Ultimately, these studies attempt to establish causal relationships between properties of the flare and the resulting plasma flows, which may be used to determine conditions in the solar atmosphere and to distinguish between different models of solar flare evolution. The number of studies dedicated to plasma flows induced by solar flares is vast, and a complete review is well beyond the scope of this introduction. Since the topic forms the core of the research presented in this thesis, however, we will discuss the results of some of the most essential studies.

Chromospheric evaporation, which we briefly described in Section 1.3, remains the generally accepted model for explaining how flare loops are filled with high-temperature plasma, resulting in both the observed X-ray and UV spectral line emission and line shifts. The flare-driven evaporation theory was first proposed by Neupert (1968) and subsequently expanded in Sturrock (1973), and was opposed to alternative models of flare loop filling such as coronal condensation. Over the next two decades, numerous investigations confirmed the chromospheric evaporation model and constrained properties of the plasma flows. For example, the first quantitative estimate of the total mass of evaporated plasma during a flare was made by Acton et al. (1982), which concluded that the observed mass was sufficient to explain the total soft X-ray emission for that flare. Other studies established the balances of both momentum (Zarro et al., 1988) and energy (Canfield et al., 1991) in observations of flare-driven evaporative flows.

One particularly important property established during this period was the velocity-temperature distribution of evaporative flows during flares (Antonucci et al., 1985, 1990; Tanaka, 1987). The general result of these studies was to show that the bulk of the evaporated plasma has a temperature of 13–18 MK and initial upflow velocities of 250–430 km s^{-1}. There was also a high-temperature (18–32 MK) component with a faster upflow velocity of 520–790 km s^{-1}. Thus, the broad relationship is for evaporation velocity to increase with plasma temperature. Unfortunately, many spectral

studies conducted during this time were limited by instrumentation to a small set of temperatures, sometimes only investigating a single spectral line for a given flare event (Ichimoto & Kurokawa, 1984; Zarro & Canfield, 1989). Even studies using multiple spectral lines were hampered by the spatial resolution of the instrumentation. The *Hard X-ray Imaging Spectrometer* on the *Solar Maximum Mission* (SMM), for example, had a spatial resolution of $\sim 8''$, and the *Bragg Crystal Spectrometer* (BCS) on board *Yohkoh* was a full-disk instrument. The velocity-temperature distribution across the full range of coronal (ambient and flaring) and transition region temperatures for a single loop footpoint during a flare was thus not well-resolved.

This situation changed in September 2006 with the launch of the *Hinode* satellite with a package of optical, X-ray, and EUV instrumentation. This included the EUV imaging spectrometer *Hinode/EIS*, which can record at least two dozen useful spectral lines with formation temperatures ranging from 50,000 K (He II) up to nearly 20 MK (Fe XXIV) with a spatial resolution of $\sim 2''$. Several studies in the last decade have used *Hinode/EIS* observations to establish the velocity-temperature distribution, for both flare-driven upflows and downflows, with unprecedented temperature resolution for several different flares; these include Milligan et al. (2006), Milligan & Dennis (2009), Milligan (2011), and Li & Ding (2011). One significant result of all these studies was to constrain the temperature at which upflows transitions into downflows at the loop footpoint. This temperature varies substantially between different flares

but are in all cases at or above that of the ambient corona, ranging from between 1–2 MK for one event (Milligan & Dennis, 2009) to over 6 MK for another (Li & Ding, 2011). As it turns out, this transition temperature can serve to discriminate between different models of the energy deposition in the chromosphere.

The observational studies of chromospheric evaporation flows we have discussed above have been complemented by numerous computational simulations of flare loops, with some of the most significant work being performed in the 1980s. Generally speaking, the majority of these simulations may be grouped into two categories, classified by the assumed energy transport mechanism driving the flows. As discussed in Section 1.3, this mechanism is either a TCF driven by plasma heating at the loop top, or a NTE beam generated within the loop. Examples of early studies of simulations using TCFs include Nagai (1980), which established the role of the conduction front in driving the chromospheric response; Cheng et al. (1984), which studied the dynamics in the case of asymmetric heating; MacNeice (1986), which calculated intensities of the O V 1371 Å line; and Fisher (1986), which found an upper limit of $2.35c_s$ for the upflow velocities. Studies during the same period involving NTE beams include MacNeice (1984), which showed that the evaporating plasma can increase the beam absorption rate; Nagai & Emslie (1984), which focused on modeling the observed line emission and differential emission measure; and Fisher et

al. (1985a,b,c), which established the existence of redshifted condensation fronts in the chromosphere.

Simulations using the NTE beam model proved popular for two reasons. First, they enjoyed some success reproducing the observed flow characteristics in many flare events; and second, the presence of NTE beams during flares has independent observational support (e.g. Canfield & Gunkler (1985)). However, there are also two significant problems with NTE beam-driven simulations. The first is that there currently exists no self-consistent mechanism of generating NTEs via the reconnection process, meaning that the NTE beam must be introduced completely *ad hoc*. The other major issue in some events is that the population of NTEs cannot deliver sufficient energy to the chromosphere to drive the observed evaporation.

Simulations of evaporation driven by TCFs also have enjoyed broad support over the last several decades, for similar reasons as the NTE beam models. Unlike NTE-driven evaporation, however, models for the reconnection energy release have existed for some time (as discussed in Section 1.3). Additionally, more recent work has established mechanisms for converting free magnetic energy stored in the loops into slow magnetosonic shocks and thermal heating of the coronal plasma (Semenov et al., 1998; Longcope et al., 2009), which generates TCFs. Thus, there exist self-consistent pathways to translating properties of the reconnection into properties of the resulting TCF-driven evaporation, without *ad hoc* assumptions.

Published studies of simulations utilizing either of these two heating mechanisms have generally been quite successful matching results to specific observations of flare evaporation flows. However, there has heretofore been little work using simulations to systematically study relationships between input parameters and the properties of the resulting evaporation flows. Initially, this was due to limited computational power; simulations simply took too long to run and so could not be efficiently used to study parameter spaces for multiple parameters. The continuously increasing speed of computers now means that a simulation model can be run quickly for many different parameters, permitting investigations into the relationships between input parameters (which are often related to quantities that are difficult to measure directly) and resulting properties of the evaporation flows (which are obtained via direct observation). Simulations may therefore be used to understand the underlying physics connecting flare energy release and transport to the resulting evaporation flows, and further to indirectly diagnose conditions in the pre-flare corona via observations of the chromospheric footpoint plasma.

Observations of plasma motions at flare loop footpoints are not limited to evaporative flows along the loop. As discussed in the previous Section, the energized chromospheric plasma at the loop footpoints begins radiating strongly across a wide range of spectral lines, from UV to X-ray, forming bright bands to either side of the flare loop arcade which are known as flare ribbons. The flare ribbon emission

is generally understood to represent footpoints of loops which have recently undergone magnetic reconnection in the corona (Forbes & Priest, 1984). Therefore, as the flare continues to reconnect new field lines on top of the previous ones (see Figure 1.3), the flare ribbon moves outward away from the polarity inversion line (Kopp & Pneumann, 1976). This link between ribbon and reconnection means that the ribbon structure in the chromosphere is an indirect image of the reconnection current sheet structure located much farther up in the corona (Forbes & Priest, 1984). Numerous studies have thus been focused on using ribbon evolution to diagnose conditions in the reconnection region (see, e.g., Schmieder et al. (1987), Falchi et al. (1997), Isobe et al. (2005), and Miklenic et al. (2007)), in particular the reconnection rate (Qiu et al., 2002).

In addition to this large-scale behavior, observations from the *Transition Region and Coronal Explorer* (*TRACE*, Handy et al. 1999) have revealed that flare ribbons can also exhibit small-scale substructure and motions. In particular, some flare ribbons were found to break into multiple small sources, dubbed *compact bright points* (Warren & Warshall, 2001; Fletcher & Warren, 2003; Fletcher et al., 2004), and in at least one case these were shown to exhibit random motions superimposed on the ribbon spreading (Fletcher et al., 2004). Compact bright points have been interpreted as a result of the magnetic canopy influencing the footpoint paths, and Fletcher et

al. (2004) used bright point intensities to measure the local reconnection rate (as opposed to the more global measurements provided by Qiu et al. (2002)). Additionally, Li & Zhang (2015) used an observation of an X-class flare to identify a quasi-periodic oscillation in the flare ribbon, which they interpreted as a signature of slipping reconnection in the current sheet driving repeated impulsive footpoint heating. These observations therefore represent an untapped potential to use spectral observations of ribbon motions to diagnose coronal dynamics.

Finally, as discussed in Section 1.3, the end result of the evaporation from the chromosphere is to fill the flare loop with hot plasma. This plasma subsequently cools through a combination of radiative, conductive, and enthalpy flux losses, and eventually it loses pressure support in the loop and begins to fall back down the loop towards the chromospheric footpoints. This process, known as coronal rain, has been thoroughly observed in off-limb prominences using both imaging (Brueckner, 1981; Winebarger et al., 2001, 2002) and spectral (Brekke et al., 1997a) techniques. On-disk measurements of flare loop draining, however, have proven harder to obtain, although Czaykowska et al. (1999) did observe redshifts indicative of loop draining for one event. Thus, there is significant room for improvement in terms of using spectral observations of redshifted draining plasma to constrain flow velocity models in post-evaporation flare loops.

In summary, despite significant advances in both instrumentation and computational modeling, significant and fundamental questions concerning the properties of flare-driven plasma flows remain open. There are three in particular to which we now draw attention. First, what are the precise relationships between initial conditions in the corona and the subsequent flows which fill the loop, and can the flow properties be used to infer properties of the corona? Second, how do we use observations of the chromosphere, particularly the flare ribbons which represent the loop footpoints, to diagnose coronal dynamics? Third, and finally, what models of the coronal downflow velocities are consistent with observations of post-evaporation flare loop redshifts?

1.5. The Narrative of My Story

I opened this introduction with a quote from Canto X of the *Paradiso*, in which Dante describes his arrival with Beatrice at the fourth circle of heaven (the Sun) and speaks with the Wise. Following this theme, I have, in the spirit of Dante's *Commedia*, divided the story of my research into three roughly equal chapters (or *canticles*, to follow his example). Each of these three chapters represents a separate, yet generally related, study of chromospheric and flare plasma dynamics, with each one relating to a different phase in the evolution of a solar flare.

I will begin in Chapter 2 with my earliest research, in which I developed a 1-D hydrodynamic simulation code in order to study shock-induced thermal conduction

fronts and the properties of the associated chromospheric evaporation (Brannon & Longcope, 2014). This work improves on earlier studies of conduction-based evaporation simulations in two ways. First, those prior studies simply applied thermal heating *ad hoc* to various locations in the loop and reported the simulation results for the evaporation. However, as discussed above, it is now understood that the process of magnetic reconnection and loop contraction induces slow magnetosonic shocks that compress and heat the plasma (Longcope et al., 2009; Longcope & Bradshaw, 2010; Guidoni & Longcope, 2010), and that these shocks are the source of the thermal conduction fronts. In Brannon & Longcope (2014) we include these shocks to drive the thermal conduction fronts, thereby providing a more consistent source for the evaporation energy. The other improvement over previous work is that prior studies focused on one or two simulations, making it difficult to make broad conclusions about the impact of various parameters on the resulting evaporation properties. We therefore performed 25 different simulations varying two different parameters, the post-shock temperature and the coronal temperature, and used the results to extract scaling relationships with observable evaporation properties.

In Chapter 3 I move on to analyzing an observation from the Interface Region Imaging Spectrograph (IRIS) instrument launched in June 2013. In this imaging and spectroscopic observation of a flare ribbon, we found an unusual coherent wave pattern in the ribbons, previously unobserved in any event, coupled with a similarly

coherent pattern of alternating red and blue Doppler shifts (Brannon et al., 2015). The relative phases of the wave pattern and the Doppler shifts lead us to conclude that the ribbon wave was the chromospheric imprint of dynamics in the coronal reconnection current sheet during the flare, specifically a Kelvin-Helmholtz or tearing-mode instability. Although these instabilities have been proposed to occur in the corona before, and some studies have reported direct observations of them in progress, this is to our knowledge the first study proposing that the chromospheric ribbons at the loop footpoints may be used to indirectly observe instabilities in the corona.

The third and final part of my research is presented in Chapter 4, in which I describe an analysis of another IRIS observation of flare loops. In this study, I investigate spectroscopic observations of the entire process of evaporation at flare temperatures, followed by the cooling of the loop by conduction and radiation, and finally concluding with a well-resolved Doppler velocity profile at chromospheric temperatures. Although each of these processes (evaporation, cooling, and draining) has been reported on previously, this appears to represent the first time the entire process has been observed with a single spectroscopic instrument on-disk (as opposed to off-limb). Finally, we use the velocity profile to constrain a simple model of the loop draining, in which we assume that the velocities are due to the plasma accelerating freely under gravity from the loop top, and we construct synthetic IRIS spectra to compare with the observations.

I will at last end with Chapter 5, which is a brief discussion and retrospective. In that chapter I will reflect on the arc of my graduate research, on the impact it may have on the field of solar flare observations and modeling, and future avenues of related research which I or other scientists may choose to investigate.

2. MODELING PROPERTIES OF CHROMOSPHERIC EVAPORATION DRIVEN BY THERMAL CONDUCTION FRONTS FROM RECONNECTION SHOCKS

Contribution of Authors and Co–Authors

Manuscript in Chapter 2

Author: Sean Brannon

Contributions: Conceived and implemented study design. Constructed code to analyze data sets. Wrote first draft of the manuscript.

Co–Author: Dr. Dana Longcope

Contributions: Helped to conceive study. Provided feedback of analysis and comments on drafts of the manuscript.

Manuscript Information Page

Sean Brannon, Dana Longcope
The Astrophysical Journal
Status of Manuscript:
___Prepared for submission to a peer–reviewed journal
___Officially submitted to a peer–reviewed journal
___Accepted by a peer–reviewed journal
_x_Published in a peer–reviewed journal

Published by the American Astronomical Society
Published February, 2014, ApJ 792, 50

ABSTRACT

Magnetic reconnection in the corona results in contracting flare loops, releasing energy into plasma heating and shocks. The hydrodynamic shocks so produced drive thermal conduction fronts (TCFs) which transport energy into the chromosphere and drive upflows (evaporation) and downflows (condensation) in the cooler, denser footpoint plasma. Observations have revealed that certain properties of the transition point between evaporation and condensation (the "flow reversal point" or FRP), such as temperature and velocity-temperature derivative at the FRP, vary between different flares. These properties may provide a diagnostic tool to determine parameters of the coronal energy release mechanism and the loop atmosphere. In this study, we develop a 1-D hydrodynamical flare loop model with a simplified three-region atmosphere (chromosphere/transition region/corona), with TCFs initiated by shocks introduced in the corona. We investigate the effect of two different flare loop parameters (post-shock temperature and transition region temperature ratio) on the FRP properties. We find that both of the evaporation characteristics have scaling-law relationships to the varied flare parameters, and we report the scaling exponents for our model. This provides a means of using spectroscopic observations of the chromosphere as quantitative diagnostics of flare energy release in the corona.

2.1. Introduction

The generally accepted picture of the solar flare process begins with the reconnection of magnetic field lines in the solar corona. The freshly reconnected flare loop is then free to retract under magnetic tension, which heats and compresses the loop-top plasma, forming hydrodynamic shocks (Longcope et al., 2009) and accelerating electrons near the loop apex. In the case of shocks, the steep temperature gradient between the ambient coronal plasma and the hotter post-shock plasma results in thermal conduction fronts (TCFs) that rapidly propagate down each leg of the loop (Craig & McClymont, 1976; Forbes et al., 1989; Tsuneta, 1996). In the case of

accelerated electrons, the result is a large flux of non-thermal particles (NTPs) that precipitate down the loop towards the footpoints (Brown, 1973).

Although the question of which of these two models constitutes the dominant energy transport mechanism has not been resolved, the end result is similar; namely, the transport of energy down the loop which is subsequently deposited in the cooler and denser plasma in the transition region (TR) and chromosphere that lie at the loop footpoints. This deposition of energy creates a significant overpressure in the TR and upper chromosphere, and drives flows of heated plasma both up and down the loop (Fisher, 1987). These upflows and downflows are historically referred to as chromospheric evaporation (Sturrock, 1973) and condensation (Fisher, 1989), respectively, and should be distinguished from unrelated flows in the corona (such as *coronal rain*) that are driven by thermal instabilities due to radiative losses. Finally, the evaporation of heated dense plasma from the chromosphere fills the loop and forms the bright coronal flare loops that are visible at temperatures of several million kelvin (MK).

A critical component to understanding the subsequent flare loop development is a detailed knowledge of the characteristics of chromospheric flows during a flare. One tool for determining these characteristics are observations of Doppler spectral line shifts, which give the flow velocities within the loop at different plasma temperatures. Ideally, the Doppler line shifts would be observed with sufficient resolution

(in temperature) to give a velocity profile near the point separating upflows from downflows, which would be useful in constraining the mechanism driving the flows. Unfortunately, it has proven difficult to obtain this data. Most studies instead prefer to investigate evaporation using only a small set of spectral lines, sometimes only a single one (Zarro & Canfield, 1989; Wülser et al., 1994; Czaykowska et al., 1999). Other studies concentrate instead on using observations to calculate other properties of the flare loop, such as the total quantity of evaporated plasma (Acton et al., 1982).

In the last few years, however, high-resolution spectral observations of flare footpoints have become possible thanks to the Extreme-ultraviolet Imaging Spectrometer (EIS) located onboard the *Hinode* spacecraft. The large number of spectral lines available with this instrument has allowed for Doppler-shifts to be derived for plasma across a broad temperature range for several different flares (Milligan et al., 2006; Milligan & Dennis, 2009; Milligan, 2011; Li & Ding, 2011). Inspection of the velocity-temperature data in these papers reveals three interesting features. First, the temperature of the point separating upflows from downflows (which we dub the "flow reversal point" or FRP) is at or above 1 MK but varies widely among observed flares (in Li & Ding (2011) it was well over 6 MK), hinting at a possible connection to properties of the flare loop. Second, the flows are broadly distributed in temperature, from 10^5 K for downflows to over 10^7 K for upflows. Finally, these studies used a

sufficient number of spectral lines to allow a rough calculation of the velocity derivative with respect to plasma temperature, which like the flow conversion temperature varies between different flares.

Significant effort has also been devoted to modeling chromospheric evaporation using computer simulations. These simulations have generally invoked one of two candidates for energy transport: non-thermal particle (NTP) precipitation (MacNeice, 1984; Nagai & Emslie, 1984; Fisher et al., 1985a,b,c), and thermal conduction front (TCF) heating (Nagai, 1980; Cheng et al., 1984; MacNeice, 1986; Fisher, 1986). NTP models have had some success explaining flow observations. However, no model yet exists which is capable of self-consistently tracking the conversion of magnetic energy, released by reconnection, into a population of NTPs. Lacking this feature, simulations must resort to introducing the non-thermal electrons *ad hoc*, with a user-specified energy flux and spectrum. Properties of the evaporation flows, such as flow conversion temperature, naturally depend on this *ad hoc* choice.

The case of TCFs is notably different owing to the existence of comprehensive models of reconnection energy release. Large scale models of reconnection, such as the early model of Petschek (1964), have used hydrodynamic equations and thus omitted energetically significant non-thermal populations. In these models, kinetic energy is converted to thermal energy at MHD shocks, raising the post-shock loop top plasma temperature and originating TCFs due to steep temperature gradients. It is therefore

possible to use these models to study how the properties of chromospheric evaporation depend on the magnetic reconnection providing the energy. As yet, however, there are no generally accepted relationships that predict evaporation velocities from flare energy. Now that observations of footpoint velocities during a flare have been made with sufficient detail to determine characteristic properties of the flows, we wish to use this characterization to infer the properties of coronal energy release.

In this paper, we use a numerical simulation code to investigate the relationship between observable properties of chromospheric evaporation during a flare and the initial properties of the flare loop. Our goal is to systematically cover a parameter space of simulation inputs in order to extract a scaling-law relationship with the output observed quantities. First, in Section 2.2, we develop a simplified model of a flare loop, reducing the more complex 2-D dynamics to a 1-D shocktube. In Section 2.3 we describe the details of our numerical simulation code, including our simplified loop atmosphere model and shock initialization. Then, in Section 2.4, we detail the evolution of one particular simulation including the basic hydrodynamics and the differential emission measure, develop a consistent method of extracting synthetic Doppler velocities similar to observations, and compare the results to one particular set of observed flow velocities. Finally, in Section 2.5 we describe the parameter survey we use to extract scaling law relationships between inputs and synthetic observations, and determine the best-fit parameters.

2.2. Flare Loop Model

The idealized flare loop model we use in this paper is an extension of the thin-flux-tube model developed in Longcope et al. (2009). In that model a brief, localized reconnection event is assumed to have occurred between two adjacent magnetic flux tubes previously separated by a current sheet. The sheet exists between field lines whose directions differ by less than 180° (i.e. field which is not perfectly anti-parallel). The result is a "Λ"-shaped loop such as the one shown in the upper schematic in Figure 2.1 (adapted from Figure 2 in Longcope et al. (2009)) by the long dashed lines. In this picture the current sheet is located above the dashed line in the plane of the diagram, and the reconnection angle ζ between the field lines is defined as indicated. This angle, apparent when viewing the current sheet from the side, differs from the narrow opening angle between shocks when the sheet is viewed edge-on. The latter angle has been a focus of steady-state modeling such as the seminal work of Petschek (1964); this is *not* the angle ζ. Also note that a similar "V"-shaped field line would also have resulted from the reconnection, however we omit that portion in our schematic. This model also assumes that the ratio of gas pressure to magnetic pressure, known as the plasma-β parameter and defined by

$$\beta = \frac{8\pi p}{B^2} \tag{2.1}$$

where B is the magnetic field strength, is much less than unity. This is generally true of the pre-flare corona and transition region (TR) (Gary, 2001). The plasma-β will have increased in the retracting flux tubes (i.e. outflow jets), but provided the reconnecting field was sufficiently far from anti-parallel it will still be less than unity (Longcope et al., 2009). Within the TCFs, which will be our primary concern, β will lie between the initial value and that of the compressed, heated loop-top. Under the assumption of small β, both the plasma and the thermal conductive flux are constrained to move only along the field line. It is also assumed in order to justify a one-dimensional treatment that the tube of reconnected flux is "thin" in the sense that the scale of variations along the loops are generally much greater than their widths. Finally, in addition to the background model developed in Longcope et al. (2009), we introduce a cool, dense chromosphere at the feet of the loop (shown as the blue portion of the tube in the upper schematic in Figure 2.1), which acts as a mass reservoir.

After the initial reconnection event the subsequent contraction of the field line under magnetic tension results in a shorter loop shown by the colored portion in the schematic, with the ambient coronal plasma indicated in yellow. As the loop contracts, free magnetic energy is released into accelerating the plasma downward and inward; the inward motion corresponds to motion parallel to the axis of the flux tube (Longcope et al., 2009). Starting from the initial configuration, as the contracting loop

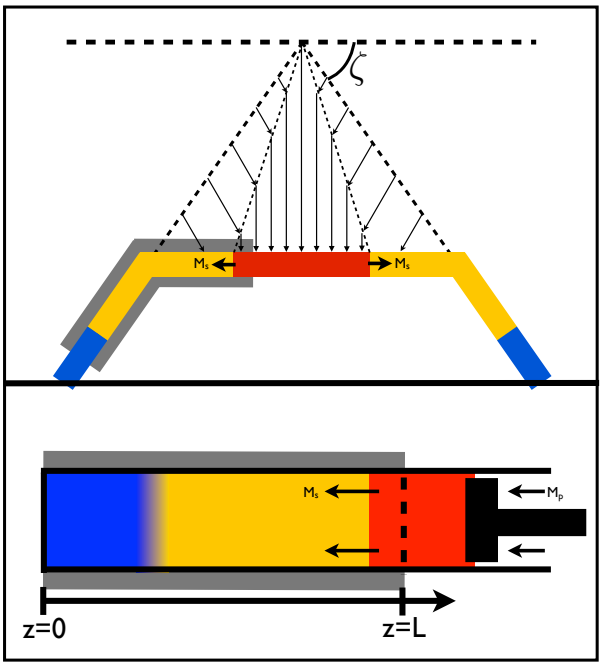


Figure 2.1. Top: schematic diagram of a reconnected flare loop, with initial flux tube geometry shown by the long dashed lines and the reconnection angle ζ is defined as indicated. Colored portion shows the later flux tube position after contraction, with yellow and blue respectively indicating coronal and chromospheric plasma. Solid arrows indicate trajectory of accelerated coronal plasma before and after the slow-mode shocks (short dashed line), and the red region indicates the hot, compressed post-shock plasma. Bottom: schematic diagram of the simplified "shocktube" model used in this paper, after neglecting gravity and loop geometry (color-coding is identical). The gas dynamic shock is driven by an assumed piston (far right) moving leftward at M_p. The gray box in both schematics indicates the simulation region.

passes each of the angled solid arrows the plasma at that location is accelerated by the rotational discontinuity down and inward toward the loop center; the subsequent trajectory of the plasma is the solid arrow itself. Eventually this accelerated plasma piles up at the loop top, as shown by the red region in the schematic, resulting in heating and compression of the plasma and the formation of two slow magnetosonic shocks resembling simple gas dynamic shocks. These shocks propagate out along the loop at a hydrodynamic Mach number M_s, determined in terms of the reconnection angle ζ by Longcope et al. (2009) as

$$M_s = \sqrt{\frac{8}{\gamma\beta}} \sin^2 (\zeta/2) \,, \tag{2.2}$$

and they follow the trajectories given by the short dashed lines. Note that the effect of the shocks is to alter the flow of the loop plasma from downward and inward to purely downward motion (Longcope et al., 2009). At the same time, strong temperature gradients across the shock fronts, going from multi-MK post-shock plasma to $\sim$1 MK in the pre-shock coronal plasma, give rise to fast-moving thermal conduction fronts (TCFs) which move out along the loop ahead of the shocks.

Since our interest is in the effects of a shock-initiated TCF on the chromosphere, and not in the overall dynamics of the loop evolution, we narrow our focus to only that section of the flare loop indicated by the gray box in the upper schematic of Figure 2.1. We also adopt a reference frame that is co-moving with the contracting loop, so that the ambient coronal plasma (yellow) is stationary and the post-shock plasma (red) is

being driven down the loop. We further simplify the model by neglecting gravitational stratification of the plasma. The resulting horizontal "shocktube" model of the flare loop is shown in the lower schematic in Figure 2.1, with the region of interest again indicated in gray. In this model, the post-shock plasma behaves as though driven by a piston, located to the right of the region of interest and moving leftward at a Mach number M_p (referring to the pre-shock coronal plasma), and the shock front moves leftward down the tube at M_s. Finally, we include a simplified model of the TR and chromosphere (blue in the schematic), the details of which will be discussed in Section 2.3.4.

2.3. Simulation Setup

2.3.1. 1-D Fluid Equations

Following the above discussion we consider a one-dimensional shocktube of plasma with uniform cross-section and total length L, parameterized by a coordinate $0 \leq z \leq L$, as shown in the lower schematic of Figure 2.1. We wish to numerically simulate the plasma hydrodynamics within the tube, beginning at an initial time $t_0 = 0$ forward to some later time t. We begin by assuming that the plasma is everywhere of sufficient collisionality to be adequately described as a single-fluid with pressure p, proton number density n, average flow velocity v, and temperature T. In this case, we recall

the 1-D hydrodynamic equations for an ideal fluid, given by

$$\frac{\partial n}{\partial t} = -\frac{\partial}{\partial z}\left[nv\right]; \tag{2.3}$$

$$\frac{\partial v}{\partial t} = -v\frac{\partial v}{\partial z} - \frac{1}{m_p n}\left(\frac{\partial p}{\partial z} - \mu\frac{\partial^2 v}{\partial z^2}\right); \tag{2.4}$$

$$\frac{\partial T}{\partial t} = -v\frac{\partial T}{\partial z} - \left(\gamma - 1\right)T\frac{\partial v}{\partial z} + \frac{\gamma - 1}{k_b n}\left\{\frac{\partial}{\partial z}\kappa\frac{\partial T}{\partial z} + \mu\left|\frac{\partial v}{\partial z}\right|^2 + \dot{Q}^{(ext)}\right\}, \tag{2.5}$$

where m_p is the proton mass, k_b Boltzmann's constant, μ is the parallel dynamic viscosity, and κ the thermal conductivity (discussed in Section 2.3.3). We adopt gas constant $\gamma = 5/3$ for a fully ionized monatomic plasma. Note that we do not include gravity in Equation (2.4), and hence we neglect gravitation stratification. We also do not treat explicit coronal heating or plasma radiation in Equation (2.5), and instead have included a single heating/cooling source term $\dot{Q}^{(ext)}$ (discussed in Section 2.3.4) that is responsible for the equilibrium loop atmosphere. Finally, we close the system with the ideal gas law,

$$p = 2k_b nT. \tag{2.6}$$

For this study, we define a system of dimensionless variables, where the coronal number density n_{cor}, temperature T_{cor}, sound speed $c_{s,cor}$, and proton mass m_p are scaled to unity. From the equation for sound speed, $c_s = \sqrt{\gamma p/m_p n}$, we see that the coronal pressure is rescaled to $p_{cor} = 0.6$. Length z is rescaled by the coronal ion mean free path, given by

$$\ell_{mfp}^{(cor)} = \frac{4}{3}\frac{\mu}{m_p n c_s} = 58.5 \text{ km}\left(\frac{T_{cor}}{1\times10^6}\right)\left(\frac{1\times10^9}{n_{cor}}\right) \tag{2.7}$$

after using the classical Spitzer viscosity (Spitzer & Härm, 1953), and time t is rescaled to the sound transit time $\ell_{mfp}/c_{s,cor}$. Note that these new variables do not alter the form of Equations (2.3)–(2.6), except that k_b is formally replaced by $1/2\gamma$ via Equation (2.6). Throughout the remainder of this section, we shall assume the use of the dimensionless variables.

2.3.2. Numerical Integration

To numerically integrate the hydrodynamic Equations (2.3)-(2.5), we first construct a staggered grid G_i of total length $L = 100 \cdot \ell_{mfp}$ and uniform cell size $\Delta z = 0.05$ which defines the simulation region. The total size of the grid defined in this way is 2000 cells, to which we add two additional sets of static cells on either end to enforce the boundary conditions. These static cells are reset to their initial values after each time step. The lower boundary $z = 0$ is completely closed ($v = 0$, $\kappa = 0$), and the treatment of the upper boundary will be discussed in Section 2.3.5. The values for the hydrodynamic variables are defined at each point on the staggered grid: bulk quantities such as p and μ are defined at cell centers, and flux quantities such as v and κ are defined at cell edges. We have tested our code using both 2000 and 4000 cells and found that the results do not substantially differ. We have also tested that the staggered scheme conserves mass, momentum, and energy over the simulation region, which it generally does to within $\pm 0.1\%$ during the simulation.

With the grid and fluid variables defined, we numerically integrate Equations (2.3)–(2.5) using an explicit midpoint-stabilized stepping-algorithm for all terms except for thermal conductivity in Equation (2.5). Were a fully explicit scheme used the timestep size Δt would be chosen to satisfy the Courant conditions (Courant et al., 1967),

$$\Delta t \leq \min\left(\frac{\Delta z_i}{c_{s,i}}, \frac{\Delta z_i}{v_i}, \frac{n_i \Delta z_i^2}{\mu_i}, \frac{n_i \Delta z_i^2}{\gamma\left(\gamma-1\right)\kappa_i}\right) \tag{2.8}$$

where the minimum is taken over the full set of grid points G_i. The first two conditions are the sound wave and flow velocity timescales, and the third is the viscous timescale. The final condition is the conductive timescale, which is in general significantly smaller than any of the other three. This is because the Prandtl number, which defines the ratio of viscosity to the thermal conductivity, is typically of order $Pr \sim 0.01$ for a plasma. This results in a conductive timescale that is at least 100 times smaller than any of the other timescales, and also results in prohibitive runtimes for an explicit numerical code.

We circumvent this issue by first expanding the thermal conductive term in Equation (2.5) as

$$\left(\frac{\partial T}{\partial t}\right)_{cond} = \frac{\gamma\left(\gamma-1\right)}{n}\frac{\partial}{\partial z}\kappa\frac{\partial T}{\partial z} = \frac{\gamma\left(\gamma-1\right)}{n}\left\{\frac{\partial T}{\partial z}\frac{\partial \kappa}{\partial z} + \kappa\frac{\partial^2 T}{\partial z^2}\right\}, \tag{2.9}$$

and then implementing an implicit *Crank-Nicolson* integration method (Crank & Nicolson, 1947) for the second-derivative term (the first term is folded into the normal explicit solver). This semi-implicit scheme permits us to effectively ignore the

conductive Courant condition and use only the minimum of the first three terms in Equation (2.8). As the numerical integration proceeds, the values for p, v, n, and T for the entire grid are saved every $t_{frame} = 0.01$. The entire simulation is allowed to run until the thermal conduction front, which begins at the top of the tube and propagates down, reaches the lower boundary, at which point the closed boundary condition would begin reflecting waves back up the tube. More realistic models of the solar atmosphere than we will employ here (Section 2.3.4) show that the density in the lower chromosphere does increase rapidly Vernazza et al. (1981); Fontenla et al. (1990), and this presumably would result in wave reflections as the TCF propagates into those layers. However, the boundary reflection in our simulations results from far simpler physics than is expected in the lower chromosphere, and we have no reason to believe that the properties of these reflections would be at all similar to real reflections in a flare loop. For this reason, we have opted to simply end the simulation when the TCF reaches the lower boundary.

2.3.3. Viscosity and Conductivity

A major obstacle to keeping the hydrodynamics well-resolved in any flare loop simulation that includes both the corona and the chromosphere is the fact that the ion mean free path given in Equation (2.7), which governs the length scale over which hydrodynamic quantities may vary significantly, becomes decidedly smaller as we move down from the corona into the chromosphere. In general, the chromospheric

temperature is of order 100 times lower than in the corona and the density 100 times higher. Using the standard Spitzer formula for viscosity $\mu = \mu_0 T^{5/2}$ (Spitzer & Härm, 1953), and noting that $c_s \propto T^{1/2}$ for a plasma, then we see from Equation (2.7) that

$$\ell_{mfp} \propto \frac{T^2}{n}, \tag{2.10}$$

which results in a mean free path that is six orders of magnitude smaller in the chromosphere than in the corona. For our grid spacing of $\Delta z = 0.05$ this implies that there would be ∼50,000 mean free paths per grid cell in the chromosphere, which is inadequate to resolve fine structure hydrodynamics such as shocks.

One popular method to circumvent this issue is to use a non-uniform adaptive grid that can add or subtract grid points of varying size during the simulation to increase resolution where needed. Several established methods exist for running hydrodynamic simulations with adaptive grids, e.g. PLUTO (Mignone et al., 2007), although it is not entirely clear that such methods are able to adequately resolve shock structures in the chromosphere. Moreover, given the 1-D low plasma-β nature of our hydrodynamic model, there are no additional benefits to using an adaptive grid scheme. We therefore adopt a different approach, modifying the standard Spitzer formula for viscosity by adding an additional term of the form

$$\mu = \mu_0 \left(T^{5/2} + \alpha n c_s \right). \tag{2.11}$$

We see from Equation (2.7) that the effective mean free path then becomes

$$\ell_{mfp}^{(eff)} = \frac{4}{3}\mu_0 \left(\frac{T^{5/2}}{nc_s} + \alpha \right), \tag{2.12}$$

and in the corona, where we demand T_{cor}, n_{cor}, and $c_{s,cor}$ and now $\ell_{mfp}^{cor,eff}$ are all scaled to unity, we can solve for μ_0 as

$$\mu_0 = \frac{3}{4\left(1+\alpha\right)}. \tag{2.13}$$

To determine α, we consider the mean free path in the chromosphere. In this region, due to the low temperature and high density, the first term in Equation (2.12) essentially vanishes, leaving

$$\ell_{mfp}^{(chr)} = \frac{4}{3}\mu_0\alpha. \tag{2.14}$$

If we now impose the condition that $\ell_{mfp} \geq \ell_0$ for all points in the tube, where ℓ_0 is a lower bound that artificially boosts the mean free path in the chromosphere, we can then solve for α using Equations (2.13) and (2.14) to obtain

$$\alpha = \frac{\ell_0}{1-\ell_0}. \tag{2.15}$$

We find through experimentation that $\ell_0 = 0.01$ seems to result in adequate resolution of the hydrodynamics in the chromosphere, which thus sets $\alpha = 1/90$ and $\mu_0 = 0.7425$. We also performed test runs with $\ell_0 = 0.005$, with the observed result that shocks became poorly resolved in the chromosphere (manifested as a slowly growing sawtooth behind the shock) and a roughly 10-20% increase in the flow reversal properties described in Section 2.4.3.

To determine the thermal conductivity in this model, we first recall the definition of the Prandtl number,

$$Pr = \frac{4}{3}\frac{\mu}{k_b \kappa} = \frac{8\gamma}{3}\frac{\mu}{\kappa}; \tag{2.16}$$

we adopt $Pr = 0.012$ for the duration of this paper. Note that the modified version of μ in Equation (2.11) would result in different Prandtl numbers for the corona and the chromosphere if we used the standard Spitzer formula for conductivity $\kappa = \kappa_0 T^{5/2}$. Consequently, we modify the thermal conductivity in the same manner as the viscosity, with

$$\kappa = \kappa_0 \left(T^{5/2} + \alpha n c_s\right). \tag{2.17}$$

Substituting this expression into the expression for the Prandtl number and solving for κ_0 results in $\kappa_0 = 275$.

2.3.4. Initial Loop Atmosphere

The left-hand portion of the simulation region contains the TR and chromosphere, as shown in Figure 2.1. It is well known that the structure of a static TR and chromosphere depends critically on radiation, gravity, and even ionization states (e.g. Vernazza et al. (1981), Fontenla et al. (1990), etc.). This layer responds very rapidly to the heat flux from flare reconnection, however, and these mechanisms therefore play little role in the evaporation dynamics. The main factor determining the dynamic response is, instead, the pre-flare distribution of mass density. We therefore use a

simplified physical model tuned to produce a relatively realistic initial density distribution. The chief aspect we seek to reproduce is the very large ratio of temperatures and densities, which we quantify as

$$R = \frac{T_{cor}}{T_{chr}} = \frac{1}{T_{chr}}. \tag{2.18}$$

Since we omit gravity the initial pressure is uniform and the density ratio is the inverse of the temperature ratio. The initial distribution is given by the expression

$$\log_{10} T_{atmo} = \frac{1}{2} \log_{10} \left(\frac{1}{R} \right) \left[1 - \tanh \left(\frac{z - z_{TR}}{d} \right) \right]. \tag{2.19}$$

where z_{TR} is the center of the TR and d is a measure of its thickness. Throughout this study we shall set $z_{TR} = 25$ (one-quarter of the way up the tube from the left-end) and $d = 2.5$. In Figure 2.2 we plot the temperature profile $\log_{10} T_{atmo}(z)$ for $R = 250$ as the solid line, and by inspection we see that our choice of $d = 2.5$ results in a TR that is $\sim$10 coronal mean free paths thick.

The steep temperature gradient across the TR naturally results in a strong thermal conductive flux, given by

$$F_c = -\kappa \frac{\partial T}{\partial z}, \tag{2.20}$$

which transfers thermal energy from the hot corona to the much cooler chromosphere. This thermal flux (divided by 30) for the $R = 250$ atmosphere is plotted as the dotted line in Figure 2.2, and clearly shows that the majority of the thermal flux occurs in the upper portion of the TR. This feature is a result of the temperature profile being

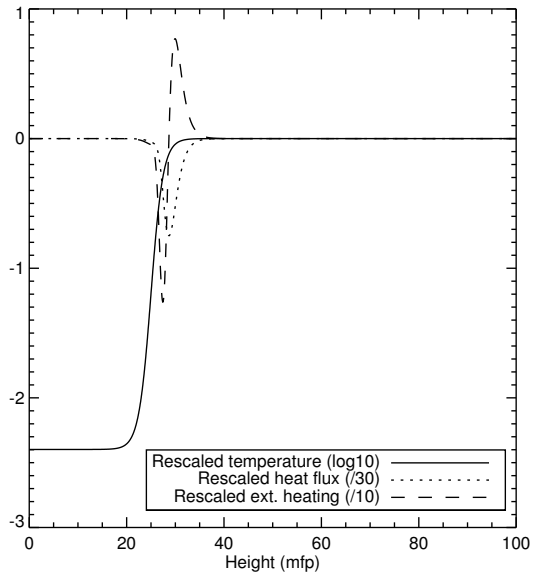


Figure 2.2. General properties of the artificial initial loop atmosphere (chromosphere, TR, and corona) as described in Section 2.3.4, in rescaled units and for a temperature ratio of $R = 250$. Solid line: log-plot of the rescaled temperature profile. Dotted line: rescaled heat flux within the TR (divided by 30). Dashed line: rescaled external heating (divided by 10) supplied to the atmosphere as a proxy for coronal heating (positive) and chromospheric radiation (negative).

defined on a log-scale, which implies that the strongest gradients in the TR will be at the higher temperature.

In order to maintain the initial temperature profile, Equation (2.19), against the action of the thermal conductive flux we introduce an *ad hoc* heating term to Equation (2.5),

$$\dot{Q}^{(ext)} = -\frac{\partial}{\partial z}\left[\kappa \frac{\partial T_{atmo}}{\partial z}\right]. \tag{2.21}$$

This term (divided by 10) is plotted as the dashed line in Figure 2.2, and consists of a source ($\dot{Q} > 0$) in the upper layer and sink ($\dot{Q} < 0$) in the lower layer. These artificial

elements stand in for coronal heating and chromospheric radiation, respectively. We keep Equation (2.21) constant throughout the run, although we find that if we turn it off during the flare simulation there is no discernible difference in the chromospheric response. This indicates that the heating mechanism is not an essential property in determining evaporation evolution, but rather the initial mass-temperature distribution of plasma in the TR.

2.3.5. Initial Piston Shock

The right-hand portion of the simulation region contains the downward-propagating piston shock, which will serve to initiate and drive the thermal conduction front (TCF) into the TR and chromosphere. The classical picture of a piston shock, as shown in Figure 2.1, is of a plug of compressed fluid being driven at velocity $v = -M_p$ down into an ambient fluid at rest with $v = 0$. M_p is the Mach number of the driving piston speed as measured in the rest fluid. The shock itself is the interface between these two regions of differing flow velocity, and it propagates ahead of the piston at speed M_s given by

$$M_s = \frac{M_p\left(\gamma+1\right)}{4} + \sqrt{\left(\frac{M_p\left(\gamma+1\right)}{4}\right)^2 + 1}. \tag{2.22}$$

The plasma compression across the shock results in an increased post-shock pressure and density, as given by the *Rankine-Hugoniot* conditions:

$$p_{ps} = \frac{2\gamma M_s^2 - \left(\gamma-1\right)}{\gamma\left(\gamma+1\right)}, \tag{2.23}$$

$$n_{ps} = \frac{(\gamma + 1) M_s^2}{(\gamma - 1) M_s^2 + 2}. \tag{2.24}$$

The post-shock temperature T_{ps} is given by Equation (2.6).

In the classical piston shock, the jump in velocity from $v = 0$ to $v = -M_p$ is instantaneous; the shock is a strict discontinuity in the fluid variables from pre-shock to post-shock. For a numerical simulation, however, we need to construct a smooth transition for the fluid velocity and other variables across the shock, preferably over a length scale of a few mean free paths, to ensure adequate numerical resolution of the shock (Guidoni & Longcope, 2010). In this model we initialize the shock by superimposing the post-shock plasma conditions over the upper 20% of the tube, scaled by a transition in the velocity centered at $z = 90$ of the form

$$v(z) \sim \tanh\left[\frac{z - 90}{\lambda}\right] \tag{2.25}$$

where λ is the initial length scale of the shock. We adopt $\lambda = 2.5$ for the remainder of this study, which results in an initial shock that is initially $\sim$10 mean free paths thick (which is identical but unrelated to the TR thickness). The post-shock region is maintained at (p_{ps}, n_{ps}, T_{ps}) by a flux of plasma at speed $-M_p$ coming across the upper boundary ($z = 100$). This flux is the result of the boundary condition we enforce for the static cells on the right-hand side of the grid, which are reset at each timestep to the original post-shock conditions. We have tested our code by simulating shocks in the absence of the TR and thermal conduction, and found that shocks do

indeed propagate at the correct speed M_s while remaining well-resolved due to the presence of viscosity in the shock region.

2.4. Simulation Results

To discuss the various features of the simulated loop dynamics, we focus first on a single simulation. The qualitative results of the evolution of this particular simulation are similar for most of the runs performed in this study. We consider a TR temperature ratio $R = 250$ and piston Mach number $M_p = 2.0$, and assume an ambient coronal temperature of $T_{cor} = 2.5$ MK and number density $n_{cor} = 10^9$ cm^{-3}. Restoring conventional dimensions to variables (assumed throughout this section) results in a total length for the simulation region $L = 36.6$ Mm, a coronal sound speed $c_{s,cor} = 270$ km s^{-1}, and a post-shock temperature $T_{ps} = 9.2$ MK. The total duration of the simulation (from the initial state to the TCF reaching the lower boundary) is $t_{sim} = 38.0$ seconds. This is slightly longer than typically quoted evolution timescales of a few seconds to roughly half a minute for models of explosive evaporation and condensation shocks (Fisher, 1987; Longcope, 2014), and thus our simulation timescale captures the entire development phase for the evaporation flows.

2.4.1. Hydrodynamics

The hydrodynamic evolution of the simulation region is shown in Figure 2.3; seven different times are plotted and color-coded according to the legend for pressure

(upper left plot), velocity (upper right plot), number density (lower left plot), and temperature (lower right plot). At the initial simulation time, $t = 0.00$ sec (black line), as we move up the tube from $z = 0$ Mm we note first the cool, dense chromosphere at 10^4 K and density 2.5×10^{11} cm^{-3}. Beginning at $\sim$7 Mm, we encounter the artificial TR, which appears only in density and temperature and continues to $\sim$11 Mm. Above the TR, we have the constant temperature and density corona, which occupies more than 50% of the length of the tube. Finally, centered between 31–34 Mm, we note the initial piston shock which accelerates the post-shock plasma to -540 km s^{-1} (negative as the shock is propagating down the tube), and which heats and compresses the plasma to 9.2 MK and 3×10^9 cm^{-3}.

By $t = 0.14$ sec (purple), we see the very rapid development of the TCF in the plasma temperature. Within this time, the TCF has propagated down to $\sim$20 Mm and has closed nearly half the distance between the initial shock position and the TR. We see from the density and velocity profiles in Figure 2.3 that the shock itself has not moved downward very far (indeed, the density profile for the shock is scarcely different than at the initial time). This is made clearer in the pressure profile where we note that the plasma pressure rises once between 20–31 Mm due to the presence of the TCF, and subsequently rises again across the shock between 31–35 Mm. This decomposition of a shock, in the presence of thermal conduction, into a TCF and a

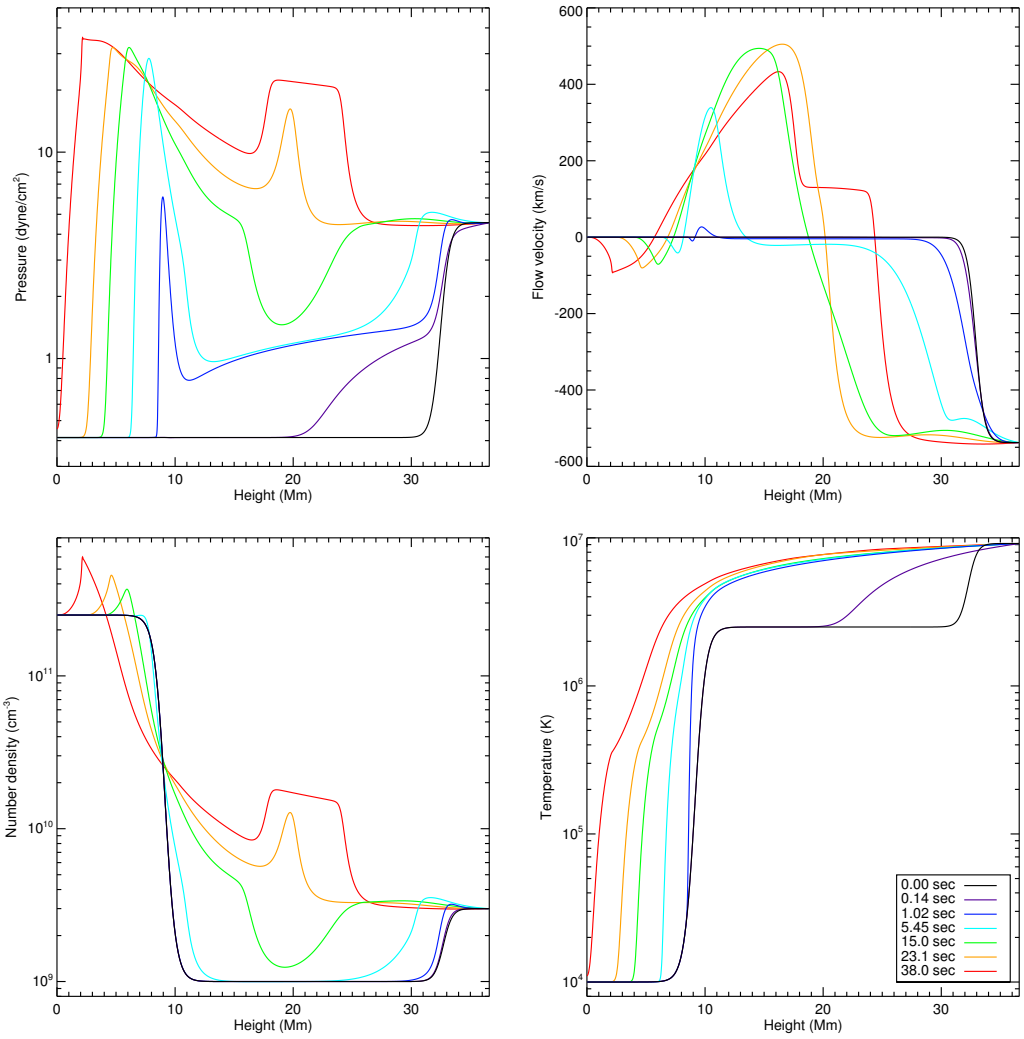


Figure 2.3. Hydrodynamic evolution of the simulation considered in Section 2.4 and as described in Section 2.4.1. Plasma profiles (as functions of position within the tube) are shown at seven different times during the simulation for pressure (upper left), flow velocity (upper right), number density (lower left), and temperature (lower right). Different times are delineated by color-coding of the profiles, and the color scheme is indicated by the legend at lower right.

so-called *isothermal sub-shock* is common and has been observed in previous models (Longcope et al., 2009; Guidoni & Longcope, 2010).

After $t = 1.02$ sec of evolution (blue), the TCF has propagated downward far enough that it encounters the cooler and denser TR plasma, which results in two distinct effects. First, the TCF slows dramatically due to the reduced thermal conductivity in the TR and chromosphere; indeed, the TCF takes 1 second to descend the $\sim$20 Mm between the initial piston shock and the TR, but takes another 37 seconds to clear the TR and chromosphere and reach the lower tube end. Second, the TCF begins rapidly depositing thermal energy into the stationary TR plasma. This rapid rise in plasma temperature in the upper TR, coupled with the stationary density profile, results in the development of a large overpressure clearly visible centered at $\sim$9 Mm. This TR overpressure is responsible for the initiation of the chromospheric evaporation upflows (visible between 9–11 Mm) and associated condensation downflows (visible between 8.5–9 Mm).

As the simulation continues to $t = 5.45$ sec (cyan), we see that the TCF has completely cleared the TR and has begun to directly heat the chromosphere. Meanwhile, the evaporation and condensation has continued to develop and we see clearly that the upflows have higher speeds and a broader spatial distribution than the downflows. This is a reflection of the momentum balance in the TR: the TCF deposits thermal energy to the TR but no net momentum, and as evident in the density profile the

condensation is occurring in a denser region than the evaporation. Also in the density profile at this time, we note the development of an evaporation front, located at ∼12 Mm, which is beginning to enhance the density of the upper TR and lower coronal regions, and a barely visible rarefaction region and condensation front in the lower TR.

We now jump forward to $t = 15.0$ sec (green). By this time, the evaporation region has grown to encompass nearly one-third of the tube, and has developed upflow speeds of ∼500 km s^{-1}. This is somewhat faster than observed velocities for plasma at these temperatures (<10 MK); Antonucci et al. (1985) and Tanaka (1987) report the bulk of the evaporation (13–18 MK) moving at 250–430 km s^{-1}. Meanwhile, the condensation region is restricted to speeds less than 100 km s^{-1}. In the density profile we now see the fully developed three-part structure of condensation (enhanced densities between 4.5–6.5 Mm), rarefaction (decreased densities between 6.5–9 Mm), and the evaporation front (which has strongly enhanced densities up to ∼16 Mm). There has also begun to be significant interaction between the upward propagating evaporation front and the downward propagating subshock (centered at ∼23 Mm), with mildly enhanced densities in between. Finally, at this point in the simulation, we begin to observe the direct effects of the artificially-enhanced thermal conductivity κ, which manifests as a "shoulder" in the TCF located between 5–6 Mm.

By $t = 23.1$ sec (orange), the upflows have reached and passed the maximum speed during this simulation of $\sim$510 km s^{-1}. For later times the maximum upflow speed in the tube is below this. This is the result of the downward propagating subshock finally encountering the evaporation front and passing through it, which is especially evident in the pressure and density profiles at $\sim$19 Mm. The strongly negative post-shock velocities thus begin to cancel the positive evaporation velocities, although the enhanced pressure that results from the combined compression of the shock and evaporation front means that some positive velocities will remain in the post-shock region.

At the end of this particular simulation, $t = 38.0$ sec (red), the TCF has fully passed through the chromosphere and has developed a distinct two-step profile due to the enhanced thermal conductivity. However, the TCF "shoulder" remains somewhat below the lower-bound of the evaporation region, and thus is not likely influencing the development of the evaporating plasma. Meanwhile, the piston subshock and evaporation front have fully passed each other, resulting in a region of highly enhanced density ($\sim 1.6 \times 10^{10}$ cm^{-3}) between 18–24 Mm. The maximum upflow speed has been reduced to $\sim$440 km s^{-1}, and a uniform upflow speed of $\sim$130 km s^{-1} has developed in the region between 18–24 Mm.

Finally, to conclude our discussion of the hydrodynamic evolution of the simulation we consider the ratio of the thermal conductive flux F_c, given by Equation (2.20),

to the free-streaming saturation limit, given in non-dimensional form by Longcope & Bradshaw (2010) as

$$F_c^{(fs)} = \frac{3}{2}\gamma^{-3/2}\sqrt{\frac{m_p}{m_e}}\left(nT^{3/2}\right), \tag{2.26}$$

where m_p/m_e is the ratio of proton to electron masses. The ratio $F_c/F_c^{(fs)}$ is plotted in Figure 2.4 for the same times and with the same color scheme as in Figure 2.3. We observe that at $t = 0.0$ sec there are two peaks in the flux ratio: one for the TR centered at 10.5 Mm, and another representing the shock centered at 32.5 Mm. We also note that the ratio is greater than unity for a narrow range of positions centered on the initial piston shock, indicating that the thermal flux across the shock is larger than the saturation value. This might indicate a substantial problem were the thermal flux to remain supersaturated for the duration of the simulation. However, by $t = 0.14$ sec, we see that the flux ratio has been reduced to <0.4 everywhere in the tube, due to the development of the TCF discussed above which quickly smoothes out the initial steep temperature gradient. This fast TCF and thermal flux development is characteristic of all simulations performed for this study, and we do not believe that this initial violation of the free-streaming saturation limit by the piston shock is of concern for the later tube evolution.

Later, as the TCF reaches the TR (1.02 sec), we note an enhancement of the flux ratio at $\sim$11 Mm as the TCF begins depositing thermal energy into the cooler TR plasma. This peak slowly begins to subside as the TCF clears the TR (5.45 sec and

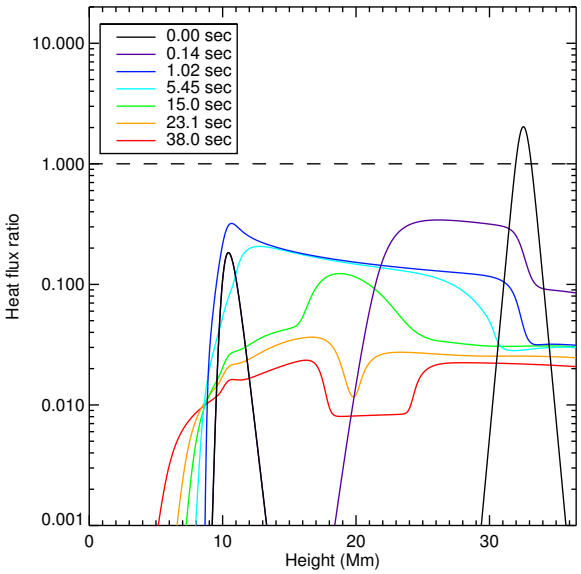


Figure 2.4. Ratio of the conductive thermal flux to the saturated freestreaming limit during the simulation discussed in Section 2.4, as described in Section 2.4.1. Both the times and the color scheme are identical to Figure 2.3.

on), although it is never fully eliminated, remaining as a small "bump" at ∼11 Mm. Curiously, we also observe that the later evolution of the flux ratio (t = 15.0, 23.1, & 38.0 sec) somewhat mirrors that of the density and pressure. This is especially notable for positions between 15–25 Mm, where we notice the density enhancement due to the interaction of the evaporation and subshock fronts mirrored as a suppression of the flux ratio. This behavior is not indicative of any change in the thermal flux, as the TCF has long since flattened the temperature profile to nearly isothermal. Rather, it is due to the increased density resulting in a larger saturation limit, lowering the flux ratio at those positions.

2.4.2. Differential Emission Measure

Although the full hydrodynamic evolution (as shown in Figure 2.3 and described above, for example) would be the preferred method to understand the plasma dynamics in a flare loop, we are limited by observational techniques in our ability to extract information about those quantities. One observational method of tracking the plasma evolution, which combines information about the density and temperature, is the *differential emission measure* (DEM), defined as

$$DEM(T) = n_e^2 \left| \frac{dT}{dz} \right|^{-1}, \tag{2.27}$$

where n_e is the electron number density (identical to the proton number density n in our fully-ionized hydrogen plasma). In Figure 2.5 we show the evolution of the DEM as a function of temperature in the tube, for the same times and with the same color scheme as in Figures 2.3 & 2.4.

At the initial time, $t = 0.00$ sec, the clearest features of the DEM are the three sharp spikes located at 10^4 K, 2.5 MK, and 9.2 MK. These peaks correspond to the uniform temperature chromosphere, corona, and post-shock regions seen in Figure 2.3. Also notable is the DEM minimum located at $\sim$ 2 MK which is a somewhat higher temperature than seen in other observational and modeled DEMs, although the overall magnitude of our DEM is comparable (Emslie & Nagai, 1985; Brosius et al., 1996). We attribute this higher-temperature minimum to the fact that our model

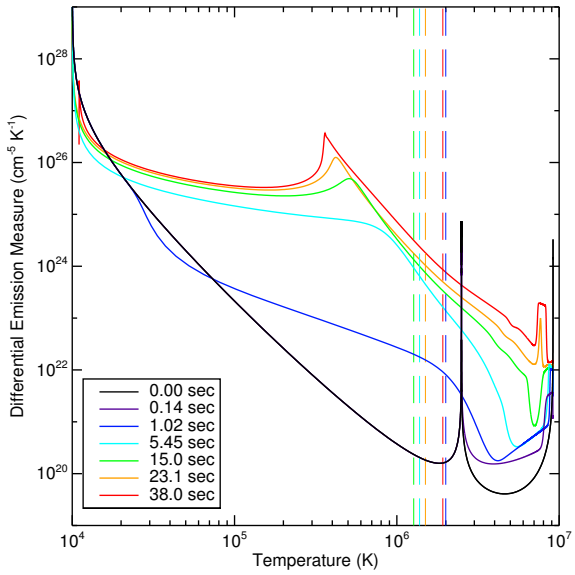


Figure 2.5. Time evolution of the differential emission measure (DEM) for the simulation discussed in Section 2.4 and described in Section 2.4.2, for the same times and color scheme in Figure 2.3. Vertical dashed lines indicate the flow reversal point (FRP) temperature, where $v = 0$ between the evaporation and condensation regions.

atmosphere, Equation (2.19), has its steepest gradient dT/dz at higher ($\sim$2 MK) temperatures, thus resulting in the DEM being minimized at those temperatures.

By $t = 0.14$ sec, the TR portion of the DEM between 10^4 K and 2.5 MK remains unchanged. Only the portion of the DEM between the uniform corona and the post-shock region has been altered as the TCF begins to smooth the temperature gradient across the piston shock, resulting in some enhancement of the DEM in the 3–8 MK range. For $t = 1.02$ sec, however, we observe significant changes to the DEM in the corona and upper TR; indeed, the entire range from 10^5 K to 2+ MK has been enhanced by a factor of 10 to 100. At this same time, recall from Section 2.4.1 that

upflows and downflows in the TR are beginning to form. To differentiate between the portion of the DEM that concerns upflows from the portion that concerns downflows, we have plotted several vertical dashed lines, in the same color palette, that indicate the temperature where $v = 0$ (i.e. the flow reversal point (FRP) separating the condensation and evaporation regions). This will be referred to henceforth as the FRP temperature T_{frp}, which is defined in terms of the simulation as the temperature at the first position z_0 where $v \geq 0.01$.

For the $t = 1.02$ sec profile, the evaporation temperatures range from the dashed blue line at 2.0 MK to slightly less than 4 MK. Similarly, for the $t = 5.45$ sec and $t = 15.0$ sec profiles, the evaporation begins at T_{frp} and ranges up to $\sim$5 MK and $\sim$7 MK respectively. In these two profiles, we note the evaporation front closing with the high-temperature post-TCF subshock, represented here by the peak in the DEM at $\sim 10^7$ K. Note that the post-shock DEM enhancement is roughly 10-fold, and since $DEM(T) \propto n^2$ this corresponds as expected to the three-fold density increase across the subshock (see Figure 2.3). We also note, in the $t = 15.0$ sec profile, the DEM enhancement of the condensation front at 5×10^5 K, which is partly due to the enhanced post-condensation density and partly to the "shoulder" which forms on the TCF as described in Section 2.4.1.

After the evaporation front and subshock interact ($t = 23.1$ sec and $t = 38.0$ sec profiles), we observe another roughly 10-fold DEM increase in the 7-9 MK range from

the combined compression of the plasma. Further, the continued compression of the post-condensation front plasma has continued to enhance the DEM, forming a large peak between 3×10^5 K and 4×10^5 K. Finally, to conclude our description of the DEM evolution for this simulation, we observe that the flow conversion temperature T_{frp} first appears at a somewhat higher temperature of 2.0 MK, subsequently descends to a lower range of 1.3 to 1.4 MK, and later rises again by the end of the simulation to 1.9 MK. Although the exact temperatures vary, this decreasing-and-increasing behavior is typical of the simulations used in this study.

2.4.3. Synthetic Doppler Velocities

As discussed in Section 2.1, observations of flare loops using the *Hinode/EIS* instrument have revealed temperature-dependent Doppler velocity profiles for plasma at the loop footpoints during chromospheric evaporation. We would thus like to construct a similar velocity-temperature profile for the simulation results, in order to compare to these observations. However, we cannot simply use the velocity and temperature profiles as shown in Figure 2.3, as this is not really what is being observed by *Hinode/EIS*. Instead, the temperature-dependent Doppler velocities are derived from spectral lines from an exposure recorded over approximately 5–10 seconds, and which are weighted by the amount of emission coming from the plasma at that temperature.

We thus wish to construct a "synthetic" Doppler velocity to compare with data. We begin by defining the plasma emission measure

$$EM = DEM(T)dT = n^2 dz, \tag{2.28}$$

and an emission-weighted plasma velocity

$$v_{EM} = EM \cdot v. \tag{2.29}$$

We next define a binned log-temperature scale with 100 equal bins per unit interval in $\log_{10}(T/T_{cor})$, and create binned versions of the emission measure, EM_{bin}, and EM-weighted velocity, v_{bin}, by summing EM and v_{EM} over each temperature bin. If there are no grid points in a given bin at that time, the values of EM_{bin} and v_{bin} for that bin are set to zero. Finally, we define a time-window $W = t_{sim}/4$ and construct the synthetic Doppler velocity as

$$\widetilde{v}(\widetilde{T}, t) = \frac{\sum_{t'=t-W/2}^{t+W/2} v_{bin}(\widetilde{T}, t')}{\sum_{t'=t-W/2}^{t+W/2} EM_{bin}(\widetilde{T}, t')}. \tag{2.30}$$

The variable window size allows us to consistently accommodate different simulation durations. For the simulation discussed thus far $W = 9.5$ sec, which is a typical exposure duration for *Hinode/EIS*. Note of course that $\widetilde{v}(\widetilde{T}, t)$ is only defined for $(W/2) \leq t \leq (t_{sim} - W/2)$, which for the Section 2.4.1 simulation corresponds to times between 4.75 sec and 33.25 sec.

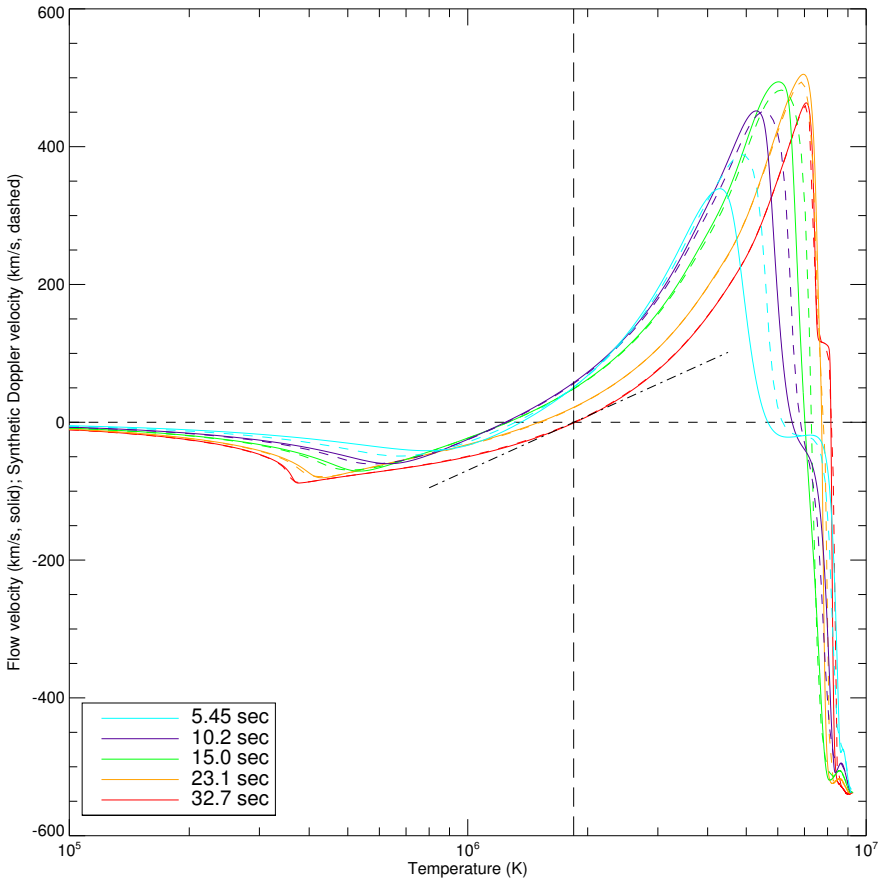


Figure 2.6. Plasma flow velocity as a function of temperature (solid lines) and synthetic Doppler velocity as a function of binned-temperature (dashed lines) for five different times during the simulation discussed in Section 2.4. Note that the times and color-coding indicated by the legend (bottom, lower left) are not identical to those in Figures 2.3–2.5. Horizontal dashed line indicates zero velocity. Vertical dashed line and diagonal dash-dot line indicate the FRP temperature and slope, respectively, of the 32.7 sec synthetic Doppler profile.

In Figure 2.6 we have plotted the hydrodynamic velocity v as a function of temperature T (solid lines) and the synthetic Doppler velocity $\widetilde{v}$ as a function of temperature $\widetilde{T}$ (dashed lines), for five representative times during the simulation and for temperatures above 10^5 K. Note that neither the times nor the color palette are identical to those plotted in Figures 2.3–2.5; this is because $\widetilde{v}$ is not defined for the three earliest times or the final time in those plots. However, we are able to include $t = 5.45$ sec (cyan) which is close to the start of the windowing, $t = 15.0$ sec (green), and $t = 23.1$ sec (orange). We have also added two additional times: $t = 10.2$ sec (replacing purple), and $t = 32.7$ sec (replacing red) which is close to the end of the windowing.

We note that one effect of the synthetic Doppler processing is to shift the velocity profiles in the upflow region to higher temperatures, particularly notable for the three earliest times. The peak Doppler upflow speed is increased by $\sim$50 km s^{-1} over the hydrodynamic velocity for the 5.45 sec profile, but is generally the same or slightly reduced for later times. Downflow speeds are slightly increased for temperatures below 1 MK, again more significantly for early times, but the observed downflow speeds remain significantly less than the upflow speeds. The FRP temperature T_{frp} separating upflows and downflows appears mostly unaffected by the processing, however the way in which we define the FRP needs to be modified due to the temperature binning. Recall that we previously defined T_{frp} as the temperature at the first position

z_0 where $v \geq 0.01$; we now determine the temperature bin B_0 where $\widetilde{v} \geq 0.01$ for each time t, and perform a fit to the two bins $(B_0, B_0 - 1)$ of the form

$$\widetilde{v} = \widetilde{C}_0 + \widetilde{S}_{frp} \log_{10} \widetilde{T}. \tag{2.31}$$

We now define the FRP temperature as

$$\widetilde{T}_{frp} = 10^{-\widehat{C}_0/\widehat{S}_{frp}}, \tag{2.32}$$

and we note that $\widetilde{S}_{frp}$ is the slope of the velocity-temperature profile at the FRP.

In the lower plot of Figure 2.6 we have indicated $\widetilde{T}_{frp}$ and $\widetilde{S}_{frp}$ for the $t = 32.7$ sec profile as the vertical dashed line and the dash-dotted line respectively. As an inspection of this plot will indicate, however, these two quantities do vary over the course of the simulation. To track the evolution of $\widetilde{T}_{frp}$ and $\widetilde{S}_{frp}$ we have plotted them as functions of time in the upper and middle plots in Figure 2.7, respectively, and as functions of each other in the lower plot in Figure 2.7. The notable "jitteriness" of the $\widetilde{S}_{frp}$ profile is due to movement between temperature bins when tracking $\widetilde{v} \geq 0.01$. We have also plotted the values for $\widetilde{T}_{frp}$ and $\widetilde{S}_{frp}$ at the five times shown in Figure 2.6 as solid squares in the upper two plots. With some exceptions (discussed in Section 2.5) the behavior of the FRP properties for other simulations is similar to that seen in Figure 2.7.

Finally, we define a mean FRP temperature $\langle \widetilde{T}_{frp} \rangle$ and slope $\langle \widetilde{S}_{frp} \rangle$, calculated by taking a time-average of $\widetilde{T}_{frp}(t)$ and $\widetilde{S}_{frp}(t)$ over the range $(W/2) \leq t \leq (t_{sim} - W/2)$.

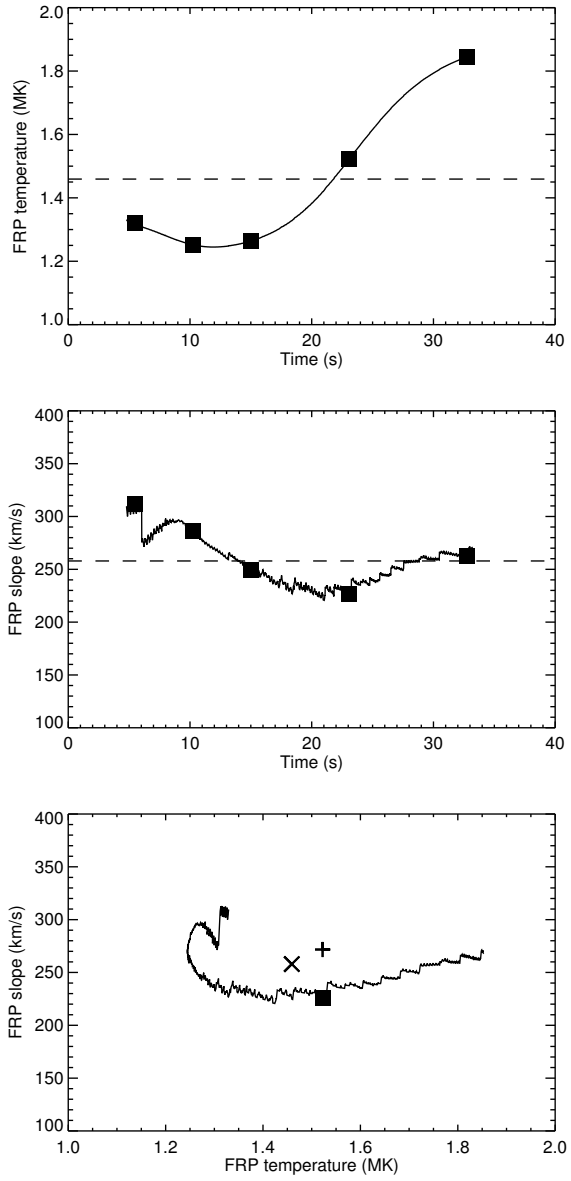


Figure 2.7. Upper and middle plots: Time evolution of the FRP temperature and slope, respectively, as determined from the synthetic Doppler velocities in Section 2.4.3. The solid squares indicate the times shown in Figure 2.6, and the dashed lines indicate the mean value for each. Lower plot: Evolution of the FRP slope plotted versus temperature. The "+", solid square, and "×" respectively indicate the observed, synthetic, and mean synthetic FRP properties from Sections 2.4.3 and 2.4.4.

For this simulation $\langle \widetilde{T}_{frp} \rangle = 1.46$ MK and $\langle \widetilde{S}_{frp} \rangle = 260$ km s^{-1}, and we have plotted these values in Figure 2.7 as the horizontal dashed lines in the top and middle plots for $\widetilde{T}_{frp}$ and $\widetilde{S}_{frp}$, respectively, and as an $\times$ in the lower plot. Obviously, the time-dependent values for the FRP properties differ from these mean values over the course of the simulation; in fact, the lower plot in Figure 2.7 shows that they do not ever assume the mean values simultaneously. However, by using the mean values we can in some sense characterize the entire evolution of $\widetilde{T}_{frp}$ and $\widetilde{S}_{frp}$ for a given simulation, which will allow us in Section 2.5 to directly compare these values for many different simulations.

2.4.4. Observational Data Fit

We conclude our discussion of this particular simulation by making a comparison of our synthetic Doppler velocities to the observed flare loop Doppler velocities published by Milligan & Dennis (2009) (with a correction published in Milligan (2011)). The event studied in that paper was a *GOES*-class C1.1 flare that took place in NOAA AR 10978 on 2007 December 14 at 14:12 UT. Serendipitously, the *Hinode/EIS* instrument was rastering over one of the flare loop footpoints during the impulsive phase of the flare, with an exposure time of 10 seconds. The authors used 15 different spectral lines, with formation temperatures ranging from 5×10^4 K to 16 MK, to derive Doppler velocities for the footpoint plasma. We have taken these Doppler velocity data and associated error ranges from Table 1 in Milligan (2011), and replotted them

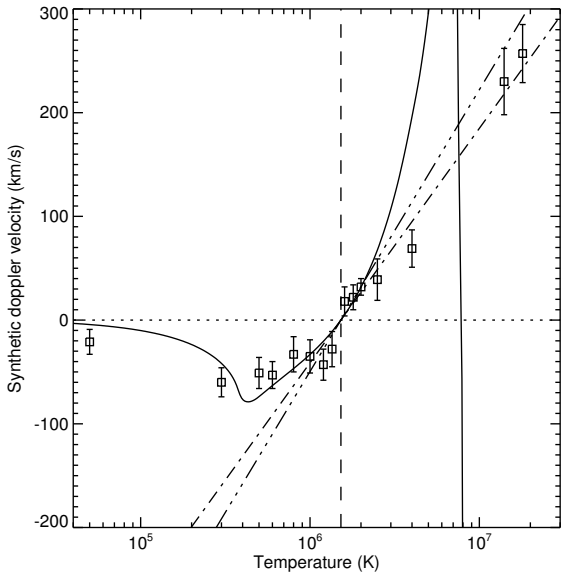


Figure 2.8. Best fit of the synthetic Doppler velocity from the simulation considered in Section 2.4 to the observed chromospheric Doppler velocities presented in Milligan (2011), as described in Section 2.4.4. Squares and error bars are the Milligan (2011) data (with reversed signs), and the dashed line and dash-triple-dotted lines are the approximate FRP temperature and slope, respectively. The solid line is the best fit of the synthetic Doppler velocity, while the dash-dotted line is the synthetic FRP slope.

in Figure 2.8 as the square points and error bars (note that we have changed the signs on these data to match our velocity convention).

Inspection of the observational data in Figure 2.8 reveals similar structure to the synthetic Doppler velocity profiles in Figure 2.6, with downflows and upflows separated by a flow reversal temperature that lies somewhere between 1–2 MK. To estimate the FRP parameters for comparison to the simulation, we take the six velocity measurements that fall in the 1–2 MK range, and use a linear fit of the form

$$v\left(T\right) = \widehat{C}_0 + \widehat{S}_{frp} \log_{10} T, \tag{2.33}$$

where $\widehat{S}_{frp}$ is the approximate FRP slope; the approximate FRP temperature is given by $\widehat{T}_{frp} = 10^{-\widehat{C}_0/\widehat{S}_{frp}}$. For the Milligan (2011) data we find that $\widehat{T}_{frp} = 1.5$ MK and $\widehat{S}_{frp} = 270$ km s^{-1}, and these values are represented by the "+" in Figure 2.7 as well as the vertical dashed line and dash-triple-dotted line, respectively, in Figure 2.8.

Since the observed flow conversion temperature is the quantity in which we have the most confidence, we fit the simulation to the data by selecting the time for which $\widetilde{T}_{frp}$ provides the best match to $\widehat{T}_{frp}$. This is found to be at $t = 23.1$ sec (orange line in Figures 2.3–2.6) with $\widetilde{T}_{frp} = 1.5$ MK and $\widetilde{S}_{frp} = 230$ km s^{-1}, plotted as the solid square in Figure 2.7. That profile for the synthetic Doppler velocity has been plotted on top of the observation data in Figure 2.8, along with a dash-dotted line representing the slope $\widetilde{S}_{frp}$. Aside from the approximate match to the FRP properties, we note that the profile from the simulation matches well to the observed velocities in the range 5×10^5 K $\leq T \leq 2 \times 10^6$ K. Outside of this range, however, the simulation profile begins to diverge from the observed values, especially for the highest temperatures (12.5 MK and 16 MK). Indeed, these temperatures do not even exist in this simulation, which has a maximum post-shock temperature of 9.2 MK.

We also observe from Figure 2.7 that the mean slope $\langle \widetilde{S}_{frp} \rangle$ is a somewhat better estimate for $\widehat{S}_{frp}$ than the value for $\widetilde{S}_{frp}$ at $t = 23.1$ secs, but that $\langle \widetilde{T}_{frp} \rangle$ is a slight underestimate for $\widehat{T}_{frp}$. Nevertheless, as an order-of-magnitude estimation, the mean value is not far removed from the observational result. Thus, we feel we are justified

in using the mean FRP properties $\langle \widetilde{T}_{frp} \rangle$ and $\langle \widetilde{S}_{frp} \rangle$ as proxies for describing the overall evolution of the evaporation during a flare.

2.5. Scaling Laws

Thus far we have developed a method for reducing the complex properties of the spatially- and temporally-dependent chromospheric evaporation driven by thermal conduction in a simple model atmosphere down to two scalar quantities, namely $\langle \widetilde{T}_{frp} \rangle$ and $\langle \widetilde{S}_{frp} \rangle$. Further, we have shown that these quantities provide an acceptable description of the FRP properties in observed chromospheric flows. An obvious question now presents itself: is it possible to systematically relate the observed FRP properties $\widehat{T}_{frp}$ and $\widehat{S}_{frp}$ back to fundamental parameters in the simulation?

Of course, with only two data inputs, it will only be possible to extract at most two parameters for the simulation. The two most useful properties are likely the TR temperature ratio R, which gives some insight into the pre-flare state of the loop, and the Mach number of the piston shock M_p, which has been shown previously to relate to the initial reconnection angle of the loop (Longcope et al., 2009). We therefore seek an invertible relationship between $(\langle \widetilde{T}_{frp} \rangle, \langle \widetilde{S}_{frp} \rangle)$ and (M_p, R); as we shall show, such a relationship does exist, but instead of M_p we shall use the post-shock temperature T_{ps}. However, the post-shock temperature is dictated uniquely by the piston Mach number, as described in Section 2.3.5, and thus the two are effectively equivalent.

To determine the desired parameter relationships, we require a set of simulations that adequately span the parameter space. At this point, in order to avoid confusion, we shall begin labeling dimensionless quantities explicitly with a superscript "$*$"; variables with ordinary units will be left as normal. We choose five values for the piston Mach number M_p^*, given by

$$M_p^* = (2.0,\, 2.5,\, 3.0,\, 3.5,\, 4.0)\,; \tag{2.34}$$

these values translate to the equivalent (dimensionless) post-shock temperatures,

$$T_{ps}^* = (3.67,\, 4.93,\, 6.47,\, 8.28,\, 10.4)\,. \tag{2.35}$$

We also choose five values for the TR temperature ratio R^*, given by

$$R^* = (100,\, 150,\, 200,\, 250,\, 300)\,. \tag{2.36}$$

Simulations were performed for all 25 combinations of the two parameters. For brevity, we will label and discuss these simulations based on the parameter values selected: the five values for T_{ps}^* are labeled "A"–"E", and the five values for R^* are labeled "1"–"5". Thus, the simulation discussed at length in Section 2.4, which had $M_p = 2.0$ and $R = 250$ would be labeled as "A4".

We next calculate, as in Section 2.4.3, the dimensionless mean synthetic Doppler velocity FRP temperature $\langle \widetilde{T}_{frp}^* \rangle = \langle \widetilde{T}_{frp} \rangle / T_{cor}$ and slope $\langle \widetilde{S}_{frp}^* \rangle = \langle \widetilde{S}_{frp} \rangle / c_{s,cor}$ for each simulation. The values of these two quantities for all 25 simulations are tabulated

Table 2.1. Simulation labels and properties.

Label	R^*	M_p^*	T_{ps}^*	$\langle \widetilde{T}_{frp}^* \rangle$	Fit error	$\langle \widetilde{S}_{frp}^* \rangle$	Fit error	Fit?
A1	100	2.0	3.67	0.929	1.8 %	2.06	-1.0 %	Yes
A2	150	2.0	3.67	0.764	0.36 %	1.44	-1.8 %	Yes
A3	200	2.0	3.67	0.659	-1.5 %	1.14	-0.38 %	Yes
A4	250	2.0	3.67	0.584	-3.5 %	0.960	2.1 %	Yes
A5	300	2.0	3.67	0.526	-5.7 %	0.841	4.8 %	Yes
B1	100	2.5	4.93	1.60	1.8 %	4.13	2.7 %	Yes
B2	150	2.5	4.93	1.35	2.7 %	2.81	-0.63 %	Yes
B3	200	2.5	4.93	1.18	2.1 %	2.15	-2.5 %	Yes
B4	250	2.5	4.93	1.05	1.1 %	1.76	-2.9 %	Yes
B5	300	2.5	4.93	0.959	-0.19 %	1.51	-2.9 %	Yes
C1	100	3.0	6.47	2.51	-3.2 %	7.42	0.49 %	Yes
C2	150	3.0	6.47	2.20	1.5 %	5.34	2.8 %	Yes
C3	200	3.0	6.47	1.96	2.9 %	4.08	0.74 %	Yes
C4	250	3.0	6.47	1.77	3.0 %	3.29	-1.5 %	Yes
C5	300	3.0	6.47	1.63	2.7 %	2.77	-2.8 %	Yes
D1	100	3.5	8.28	3.59	-12 %	10.5	-18 %	No
D2	150	3.5	8.28	3.29	-3.7 %	8.93	-0.96 %	Yes
D3	200	3.5	8.28	3.01	0.38 %	7.23	3.0 %	Yes
D4	250	3.5	8.28	2.78	2.4 %	5.94	2.6 %	Yes
D5	300	3.5	8.28	2.58	3.3 %	5.00	1.1 %	Yes
E1	100	4.0	10.4	4.78	-23 %	11.3	-47 %	No
E2	150	4.0	10.4	4.53	-13 %	11.9	-21 %	No
E3	200	4.0	10.4	4.27	-6.5 %	11.0	-6.2 %	Yes
E4	250	4.0	10.4	4.03	-2.4 %	9.63	-0.07 %	Yes
E5	300	4.0	10.4	3.81	0.13 %	8.41	2.2 %	Yes

in Table 1. In Figure 2.9 we show the results of sequences "2" (dashed), "5" (broken), "A" (dotted) and "D" (dash-dot). This parameter survey shows that increasing the chromospheric density ratio R^* leads to decreases in both FRP temperature (9c) and slope (9a). Increasing the post-shock temperature T^*_{ps} leads to an increase in each of these (9d and 9b). The flow conversion temperature lies naturally beneath the post-shock temperature solid curve in Figure 9d but can be below the coronal temperature if the chromospheric ratio is sufficiently large ($T^*_{frp} = 1$ in Figures 9c and 9d). All 25 runs are fit to a pair of power-law relations of the form

$$\langle \widetilde{T}^*_{frp} \rangle = C_1 \left(T^*_{ps}\right)^{A_{11}} \left(R^*\right)^{A_{12}} , \tag{2.37}$$

$$\langle \widetilde{S}^*_{frp} \rangle = C_2 \left(T^*_{ps}\right)^{A_{21}} \left(R^*\right)^{A_{22}} , \tag{2.38}$$

where $A_{11} = 1.84$, $A_{12} = -0.448$, $A_{21} = 2.23$, $A_{22} = -0.866$, $C_1 = 0.654$, and $C_2 = 6.14$. These fits are plotted as curves in Figure 2.9.

For the foregoing power-law fits we have chosen to omit the values for the "D1", "E1", and "E2" simulations, as doing so results in a much stronger fit for the remaining 22 simulations (the percent error between the actual values and the fit values are also tabulated in Table 1). As shown in Figure 2.9, the three omitted simulations have values for $\langle \widetilde{T}^*_{frp} \rangle$ that fall between 10–19% below the power-law fit, and values for $\langle \widetilde{S}^*_{frp} \rangle$ that fall between 14–38% below the power-law fit. We believe the reason for the poor fit for these simulations is that they fall in a "weak-TR/strong-shock" regime, where the TCF simply moves through the TR and chromosphere too quickly,

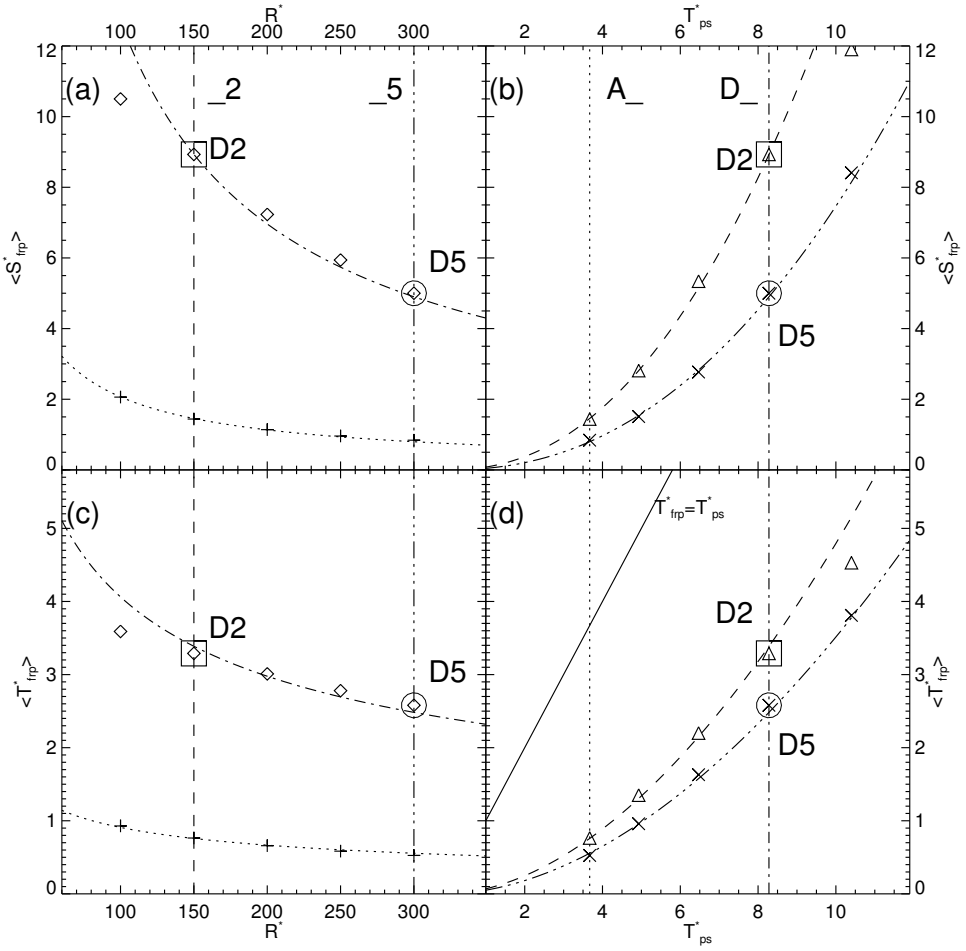


Figure 2.9. Some of the runs conducted for the parameter survey. Four of the 10 sequences are shown differentiated by line style: "2" (dashed), "5" (broken), "A" (dotted) and "D" (dash-dot). These lines show the power-law fits from Equations (37) and (38). The data points themselves are shown by symbols. The left and right columns show the variation in run conditions R^* and T^*_{ps}. The top and bottom rows show the variation in measured characteristics, $\widetilde{S}^*_{frp}$ and $\widetilde{T}^*_{frp}$. To indicate the relation between the panels runs D2 and D5 are indicated by text and by larger squares and circles respectively.

and thus the time-averaged FRP properties do not reflect the later evolution seen in Figure 2.7.

Since the dimensionless versions of the scaling laws (2.37) & (2.38) are not especially useful for handling observational data, we rescale them by using the definitions $R^* = T_{cor}/T_{chr}$ and $T^*_{ps} = T_{ps}/T_{cor}$, and the definitions of $\langle \widetilde{T}^*_{frp} \rangle$ and $\langle \widetilde{S}^*_{frp} \rangle$ given above. We also use the fact that the sound speed in the corona is given by $c_{s,cor} = c_{s,0} T_{cor}^{1/2}$, where $c_{s,0} = 0.17$ km s^{-1} K$^{-1/2}$. After some rearrangement, and making the assumption that $\widehat{T}_{frp}$ and $\widehat{S}_{frp}$ are adequate proxies for $\langle \widetilde{T}^*_{frp} \rangle$ and $\langle \widetilde{S}^*_{frp} \rangle$, we obtain the following:

$$\widehat{T}_{frp} = C_1 \, T_{chr}^{-A_{12}} \, T_{ps}^{A_{11}} \, T_{cor}^{A_{12}-A_{11}+1} \tag{2.39}$$

$$\widehat{S}_{frp} = C_2 \, c_{s,0} \, T_{chr}^{-A_{22}} \, T_{ps}^{A_{21}} \, T_{cor}^{A_{22}-A_{21}+1/2}. \tag{2.40}$$

Note that these versions of the scaling relationships require the assumption of one of the parameters T_{chr}, T_{cor}, or T_{ps}. Recall that throughout Section 2.4 we restored the simulation variables to conventional units in part by setting $T_{cor} = 2.5 \times 10^6$ K. Since $R^* = 250$ for that simulation, it follows that $T_{chr} = 10^4$ K. We now generalize this assumption for all our simulations by fixing $T_{chr} = 10^4$ K, and we then invert Equations (2.39) & (2.40) to yield the flare parameters explicitly from observables:

$$T_{ps} = G_1 \, T_{chr}^{D_1} \, \widehat{T}_{frp}^{B_{11}} \, \widehat{S}_{frp}^{B_{12}} \tag{2.41}$$

$$T_{cor} = G_2 \, T_{chr}^{D_2} \, \widehat{T}_{frp}^{B_{21}} \, \widehat{S}_{frp}^{B_{22}} \tag{2.42}$$

where $B_{11} = 1.36$, $B_{12} = -0.678$, $B_{21} = 1.17$, $B_{22} = -0.967$, $G_1 = 1.84$, $G_2 = 1.71$, $D_1 = B_{11}A_{12} + B_{12}A_{22} = -0.0225$ and $D_2 = B_{21}A_{12} + B_{22}A_{22} = 0.313$, and $\widehat{S}_{frp}$ is in units of km s^{-1}.

As a final check we determine if the run presented in Section 2.4, which fit both the observed Doppler velocity data and flow conversion properties quite well, is actually the run that would be suggested by the above scaling laws. We adopt $T_{chr} = 10^4$ K and use the observed values for $\widehat{T}_{frp} = 1.5$ MK and $\widehat{S}_{frp} = 270$ km s^{-1} in Equations (2.41) & (2.42) to obtain a suggested coronal temperature $T_{cor} = 2.4$ MK and post-shock temperature $T_{ps} = 8.4$ MK, implying a dimensionless TR ratio $R^* = 240$ and post-shock temperature $T^*_{ps} = 3.5$. From Table 1, we see that the simulation closest to these suggested values is indeed "A4", with $R^* = 250$ and $T^*_{ps} = 3.67$, indicating that the derived scaling laws do indeed yield reasonable results.

2.6. Discussion

In this paper we have developed a numerical simulation code to investigate relationships between certain observable properties of chromospheric evaporation and more fundamental (but difficult to determine) properties of the loop atmosphere and of coronal energy release. This code is an extension of the model developed in Longcope et al. (2009), in which the coronal plasma in a post-reconnection flux tube is

accelerated and compressed due to the contraction of the loop under magnetic tension. The compressed plasma at the loop top results in slow magnetosonic shocks, and the post-shock plasma is heated to flare temperatures of several megakelvin from the conversion of free magnetic energy to kinetic and then to thermal energy. We have extended this model to include a highly simplified model chromosphere and transition region (TR) at the loop footpoints to act as a mass reservoir. Thermal conduction from the post-shock plasma transports heat down toward the footpoints, resulting in impulsive heating of the chromospheric and TR plasma, a disruption of the equilibrium state in the form of an overpressure peak, and finally bulk flows of plasma known as chromospheric evaporation and condensation.

In creating the numerical simulation code, we made a variety of simplifying assumptions beyond the piston shock model. First, we opted to ignore gravitational stratification and loop geometry, effectively assuming a horizontal tube of uniform cross-section. We also left out explicit radiation and coronal heating, instead setting up our model loop atmosphere using a simple function for the temperature profile. We then calculated the necessary heating input to maintain that atmosphere at equilibrium and supplied that to the loop for the entire simulation. We chose these particular simplifications in part because they allowed us to assign definite values for certain parameters of interest (e.g. the ratio of the coronal to chromospheric temperatures), and thus more easily make comparisons between simulations with different values for

those parameters. We did test the effect of the heating input on the simulations by turning it off for a test run, and we found no significant impact on the result for that simulation. Although we did not present it, we also conducted a preliminary test varying the thickness of the transition region, and found only a very weak impact on the results. However, since we used the same function for the temperature profile for all simulations, we are unable to make any claims about how a different temperature and density profile might alter the results. Finally, recall that in order to adequately resolve features in the chromosphere, we artificially enhanced the viscosity and conductivity at low temperatures. This has the effect of altering short-scale physics, and also reducing velocities at low-temperatures, and decreasing this enhancement by 50% results in 20% and 10% increases in T_{frp} and S_{frp}, respectively. We do not believe, however, that this substantially alters either our data comparison or our final conclusions.

To demonstrate the results of the code, we discussed in detail the hydrodynamic and DEM evolution of a single simulation, as the results for our other simulations were qualitatively similar and differed only in quantitative details. In terms of broad-scale features, we observe that our results using this code are also qualitatively similar to simulations performed in other studies of impulsive conduction-driven evaporation. This includes the rapid development of the thermal conduction front (TCF) and development of the isothermal subshock (ISS), the overpressure in the TR, and the

presence of both upflows and downflows (so-called "explosive" evaporation) with upflow velocities dominating (Nagai, 1980; Cheng et al., 1984; MacNeice, 1986; Fisher, 1986). The magnitude and shape of the DEM profile was found to be similar to other studies (Emslie & Nagai, 1985; Brosius et al., 1996). This is encouraging, since our model is in many ways simpler than other models (as discussed above) but still seems to evolve in a broadly similar manner. Our model differs from most others, however, in one particularly substantial aspect: the use of a hydrodynamic shock to drive the TCF. This shock, and the associated downflows, introduce a complex interplay between the evaporation front and the isothermal subshock. It also serves to resolve the issue of the free-streaming saturation limit, which is easily violated using *ad hoc* heating models. Instead we find that, after a brief initial violation in the piston shock, the decomposition into the TCF and ISS quickly restores the thermal flux to below the saturation limit.

Our goal in this study was not to investigate the hydrodynamic and DEM evolution of chromospheric evaporation, which, as we have noted above, have been extensively studied elsewhere and in greater depth. Instead, our purpose was to draw a connection to footpoint velocities obtained from spectral Doppler shifts in data from instruments such as *Hinode/EIS*. To do this, we constructed "synthetic" Doppler velocities from our simulation results by first weighting the plasma flow velocities by the emission measure, then binning over temperature, and finally averaging over a

time-window of similar duration to typical *Hinode/EIS* exposure times. Although this method is not as exact as, for example, using the CHIANTI database to construct the actual spectral lines and associated Doppler shifts, we find that the results are more flexible for investigating temperature-dependent properties of observable footpoints flows.

The properties of particular note for our purpose center on the existence of a *flow reversal point* (FRP) near the loop footpoint that separates upflows from downflows. As seen in observational data, the FRP occurs at an identifiable temperature and with an identifiable velocity-temperature slope, and these properties can be seen to vary over time and among flares (Milligan & Dennis, 2009; Milligan, 2011; Li & Ding, 2011; Raftery et al., 2009). We have identified and tracked these two properties for our synthetic Doppler data, and we find that they do indeed vary over time, but that they are also confined to a fairly narrow range of values for each simulation. We thus calculated the mean values for the FRP properties during each simulation to serve as a convenient proxy while comparing different simulations. Finally, we compared the velocity data from Milligan (2011) to both the "best-fit" and the mean FRP for one of the simulations and determined that both may be considered reasonable given the data. This fact, along with the observation that the FRP properties evolve similarly across a range of simulation inputs, indicates that the mean FRP properties are a robust proxy for the overall FRP evolution during impulsive evaporation.

Having chosen the simulation inputs (namely the Mach number of the piston M_p and the ratio of coronal-to-chromospheric temperatures R) and outputs (the mean FRP temperature and slope), we then investigated whether a simple relationship may be determined using this simulation code. We have shown that it is possible to extract a general scaling-law relationship between these quantities, after replacing the piston shock Mach number with the (formally identical) post-shock temperature T_{ps}. A few exceptions to these relationships exist, particularly among the simulations where the ratio R is low and the Mach number M_p is large (the "strong-shock/weak-TR" limit), but we note that the relationships hold well if these cases are ignored. It is possible that these cases, which we note have the shortest duration among the 25 simulations, simply do not have enough time to evolve as fully as the others, particularly the FRP temperature which tends to rise as the simulations evolve. One potential solution would be to extend the length of the simulation region, particularly the chromospheric depth, to allow for runs that are of equal duration; however, this has not been tested. Finally, we observe that the scaling exponents we obtained do make some physical sense: a larger value for T_{ps} (i.e. a stronger driving shock) results in higher temperatures and flow velocities and hence in larger values for the mean FRP properties, whereas a larger value for R (i.e. a hotter pre-flare corona) results in lower temperatures and slower flows and hence suppresses the mean FRP properties. However at this point we have no intuition regarding the exact values for

the scaling exponents, and further work will be needed to determine if these values may be derived analytically.

When applied to the data from Milligan (2011), the scaling-law relationships we have determined suggest input parameters that are reasonably close to the "best-fit" that we selected from among our performed simulations. This again strongly suggests that the mean FRP properties are an adequate proxy for the overall evolution of the evaporation dynamics. Further, the ambient coronal temperature and post-shock temperature are both reasonable and typical for active regions and flare loops. That being said, we have also performed preliminary tests of our scaling law relationships on other observed flare footpoint flow profiles (e.g. Li & Ding (2011), Raftery et al. (2009)) and we find these results somewhat less encouraging. For example, one set of Doppler velocities from Li & Ding (2011) yield an ambient coronal temperature of ∼24 MK and post-shock temperature of ∼45 MK, and data from Raftery et al. (2009) suggests $T_{cor} \approx 8$ MK and $T_{ps} \approx 15$ MK. In both cases the ambient coronal temperature is significantly higher than is typically expected, and the post-shock temperature suggests a very weak effective piston shock ($M_p < 2$). Data from both papers suggest FRP temperatures comparable to what we have presented here, but have FRP slopes that are much shallower than is seen in any of our simulations.

It therefore seems likely that there is some effect, besides viscosity, acting to suppress the plasma velocities in at least the evaporation region, and possibly the

condensation region as well. We posit, without proof, that these unreasonable values for the coronal and post-shock temperature may be resolved by incorporating a flux tube "nozzle" at or near the TR. Some constriction of the magnetic flux tube is expected near the loop footpoint due to a combination of canopy expansion and magnetic pressure. The authors believe that the presence of a nozzle near the TR will modify the properties of the resulting chromospheric flows, possibly suppressing flow velocities in such a way that the shallow FRP slope is reproduced for more reasonable parameters of the flare loop. This topic will be the subject of a future study using an extension of this numerical simulation model.

2.7. Acknowledgements

We wish the thank the referee for a careful reading of our manuscript and for providing constructive comments which improved the manuscript. We also thank Dr. Sylvina Guidoni, Dr. Lucas Tarr, and Roger Scott for many productive discussions during the development of the code used in this paper, and also Prof. David McKenzie for his valuable input in preparing the manuscript. This work was supported by a grant from the National Science Foundation (NSF) and Department of Energy (DOE) Partnership for Plasma Sciences and a NASA SR&T grant.

3. SPECTROSCOPIC OBSERVATIONS OF EVOLVING FLARE RIBBON SUBSTRUCTURE SUGGESTING ORIGIN IN CURRENT SHEET WAVES

Contribution of Authors and Co–Authors

Manuscript in Chapter 3

Author: Sean R. Brannon

Contributions: Conceived and implemented study design. Constructed code to analyze data sets. Wrote first draft of the manuscript.

Co–Author: Dr. Dana W. Longcope

Contributions: Helped to design study. Provided feedback of analysis and comments on drafts of the manuscript.

Co–Author: Dr. Jiong Qiu

Contributions: Helped with coalignment of data sets. Provided comments on drafts of the manuscript.

Manuscript Information Page

Sean R. Brannon, Dana W. Longcope, Jiong Qiu
The Astrophysical Journal
Status of Manuscript:
___Prepared for submission to a peer–reviewed journal
___Officially submitted to a peer–reviewed journal
___Accepted by a peer–reviewed journal
_x_Published in a peer–reviewed journal

Published by the American Astronomical Society
Published February, 2015, ApJ 810, 4

ABSTRACT

We present imaging and spectroscopic observations from the Interface Region Imaging Spectrograph (IRIS) of the evolution of the flare ribbon in the SOL2014–04–18T13:03 M-class flare event, at high spatial resolution and time cadence. These observations reveal small-scale substructure within the ribbon, which manifests as coherent quasi-periodic oscillations in both position and Doppler velocities. We consider various alternative explanations for these oscillations, including modulation of chromospheric evaporation flows. Among these we find the best support for some form of wave localized to the coronal current sheet, such as a tearing mode or Kelvin-Helmholtz instability.

3.1. Introduction

The standard picture of the formation of flare ribbons in the solar chromosphere begins with magnetic reconnection in the corona (Kopp & Pneumann, 1976). As magnetic field lines reconnect across a current sheet, coronal flare loops are formed. The plasma along these loops is heated to flare temperatures both by the reconnection itself and by the subsequent contraction of the loop under magnetic tension (Longcope et al., 2009). The energy from this flare plasma is then transported down the legs of the loop by non-thermal particles (Brown, 1973), thermal conduction (Craig & McClymont, 1976; Forbes et al., 1989), wave propagation (Russell & Fletcher, 2013), or some other means, until it reaches the cool, dense chromospheric plasma located at the loop footpoints. Energy is rapidly deposited in the chromosphere and transition region (TR), resulting in plasma flows both up and down the loop. The upflows are called *chromospheric evaporation*, and are responsible for filling the flare loop

with hot plasma. Evaporative upflow of hot material is frequently accompanied by downward motions of cooler material, termed *chromospheric condensation* (Ichimoto & Kurokawa, 1984; Brosius & Phillips, 2004; Milligan & Dennis, 2009). Both evaporating and condensing components are significantly brighter than ambient material, and thus appear as elongated emission called flare ribbons.

As the flare progresses and new magnetic field lines are reconnected, the flare ribbons move outward from the polarity inversion line, which also marks the approximate location of the coronal current sheet (Kopp & Pneumann, 1976). The flare ribbon emission is generally considered to represent the footpoints of recently reconnected field lines, and the ribbons are therefore an indirect image of the coronal reconnection process which is imprinted into the chromosphere (Forbes & Priest, 1984). The structure and evolution of the ribbons can thus serve as an observational proxy for events occurring along the current sheet (Longcope et al., 2007; Qiu, 2009; Nishizuka et al., 2009). Significant effort has been put into using observations of chromospheric ribbons to investigate the coronal reconnection (Schmieder et al., 1987; Falchi et al., 1997; Isobe et al., 2005; Miklenic et al., 2007), including the reconnection rate and current sheet electric field (Qiu et al., 2002).

The general trend of ribbon spreading during a flare has been established for several decades, however it has only been since the early 2000's that instruments with sufficient resolution and cadence, such as the *Transition Region and Coronal*

Explorer (*TRACE*, Handy et al. 2009), have allowed for observations of small-scale substructure within the ribbon itself. Several studies of *TRACE* observations found that flare ribbons in some events were broken into small and tightly-spaced bright sources, which were dubbed "compact bright points" (CBPs) (Warren & Warshall, 2001; Fletcher & Warren, 2003; Fletcher et al., 2004). In Fletcher et al. (2004), CBPs were found to exhibit a random component to their motion in addition to the large-scale ribbon spreading, and they interpreted CBPs as individual loop footpoints that wander through the magnetic canopy during the course of the flare. Additionally, they found that the brightness of a CBP was correlated to the product of footpoint speed and line-of-sight magnetic field, which they interpreted as a measure of the local coronal reconnection rate.

High-resolution observations of coronal loops, meanwhile, have strongly suggested that instabilities may occur within the reconnection region which subsequently induce oscillations in the flare loop (Aschwanden et al., 1999; Ofman & Thompson, 2011). One such instability which has been studied in the context of the solar corona is the *Kelvin-Helmholtz* instability, which occurs at a fluid interface with a discontinuity in flow speeds (Uchimoto et al., 1991). KH instabilities have been specifically invoked to explain observed oscillations in coronal loops (Ofman & Thompson, 2011) and auroral spirals in the magnetopause (Lysak & Song, 1996). Another instability that has attracted interest is the *tearing mode* (TM) instability, in which magnetic

islands spontaneously form and grow in a current sheet during reconnection (Furth et al., 1963). The TM instability is believed to be important in permitting the fast reconnection rates required for solar flare energy release in so-called "impulsive bursty reconnection" models (Priest, 1985), and numerical simulations of reconnection have frequently invoked some form of velocity shear or TM instability along the current sheet (Karpen et al., 1995; Kliem et al., 2000).

Despite some successes (Aschwanden et al., 1999; Ofman & Thompson, 2011), it has proven difficult to unambiguously resolve either current sheet instabilities or the associated flare loop oscillations, due in part to lower emission intensities and line-of-sight effects in the corona. The chromospheric flare ribbons, on the other hand, are much more intense relative to the background emission, and any footpoint brightenings or ribbon motions are more easily distinguished from noise. The connectivity between the reconnection region and the chromospheric footpoints means that a global instability in the coronal current sheet might be expected to imprint itself into the ribbon evolution. Further, since the entire current sheet is presumably connected to the ribbons via the reconnecting flare loops, a current sheet instability would likely manifest as a substructure in the ribbons which could be easily distinguished from random CBP motion by a coherent pattern. This assumes, of course, that the transport mechanisms at play translate energy uniformly down the loops.

An alternative is that the observed ribbon patterns might be a result of the transport rather than the source. The conventional understanding, based on numerous observations of coherent ribbon motion at two magnetically conjugate sites, is that the transport does not play a significant role.

In fact, the Interface Region Imaging Spectrograph (IRIS, De Pontieu et al. 2014), which makes high spatial and temporal resolution observations of the chromosphere and TR, has captured instances of such coherent substructure in flare ribbons. One example is a recent study of an X-class flare by Li & Zhang (2015), where the authors identify a quasi-periodic slipping motion of flare loop footpoints which is observed as a series of small bright knots in Si IV which oscillate along the ribbon. They interpret this slipping behavior as an apparent motion of footpoints, which brighten and fade as quasi-periodic slipping reconnection drives impulsive footpoint heating. Finally, based on the timing of the oscillations, they suggest that the slipping reconnection may be due to varying densities in the current sheet which are driven by p-mode oscillations above the sunspots.

In this paper, we present an analysis of an IRIS observation from 2014 April 18 of a two-ribbon flare which displays coherent substructure of the ribbon during the impulsive phase of the flare, very similar to that reported by Li & Zhang (2015). We find support in the data for a scenario of a flare loop undergoing elliptical oscillations, driven by either a TM or KH instability in the current sheet. Our paper is outlined as

follows: in Section 3.2, we describe the data and the details of the flare event. Then, in Section 3.3, we describe the evolution of the flare ribbons and our method for spectral line fitting, determine the Doppler velocities for Si IV within the ribbon, and lastly discuss both the behavior of other spectral lines and compare the substructure in both ribbons between conjugate points. Next, in Section 3.4, we consider and dismiss two alternative scenarios for generating the observed ribbon substructure before proposing our scenario for instability-driven elliptical oscillation. Finally, in Section 3.5, we discuss some of the possible implications for our results.

3.2. Observation

3.2.1. Instrument

The Interface Region Imaging Spectrograph (IRIS) is a space-based observatory in low-Earth orbit that was launched on 2013 June 27. The primary instrument onboard IRIS is a dual-range UV spectrograph (SG) with 0″.16 pixels and an effective spatial resolution of 0″.4. The SG slit is 0″.33 wide and 175″ long, and covers FUV passbands from 1332 Å to 1358 Å and 1389 Å to 1407 Å and an NUV passband from 2783 Å to 2835 Å. These passbands include lines formed over a wide range of temperatures from the photosphere (5000 K) to the corona (1 to 10 million K). Two fiducials (dark bands where light is excluded from the SG) are located along the slit which provide

alignment and spatial context, and the entire SG can be rastered back-and-forth to provide coverage over a 2-D area (De Pontieu et al., 2014).

The other instrument featured onboard IRIS is a slit-jaw imager (SJI) which records context images of the observation region on either side of the SG. The IRIS SJI includes four wavelength passbands, including two transition region lines (Si IV 1400 Å and C II 1335 Å), with a field-of-view (FOV) of $175'' \times 175''$, and typically operates at one-third the cadence of the SG (due to cycling through the passbands) (De Pontieu et al., 2014). The inclusion of a SJI, with the same FOV, resolution, and alignment as the SG allows for detailed contextual knowledge of the slit placement relative to observational features such as sunspots, ribbons, and coronal loops. It also facilitates very precise co-alignment ($< 1''$) between IRIS and other instruments, such as SDO/AIA, by aligning visual features in the SJI to images from those instruments.

3.2.2. Flare

The event investigated in this paper is a GOES M7.3-class flare that occurred on 2014 April 18. The flare was located in NOAA Active Region 12036, which on that day was located at approximately $500''$ West and $200''$ South from solar disk center. The flare start time was 12:31 UT and the GOES X-ray flux peaked at approximately 13:03 UT, with the event mostly concluded by 13:20 UT. The large-scale structure consists of two chromospheric ribbons, one on the east side and one on the west side of the flare, visible as strands of intense 1600 Å emission at 12:46:40 UT in

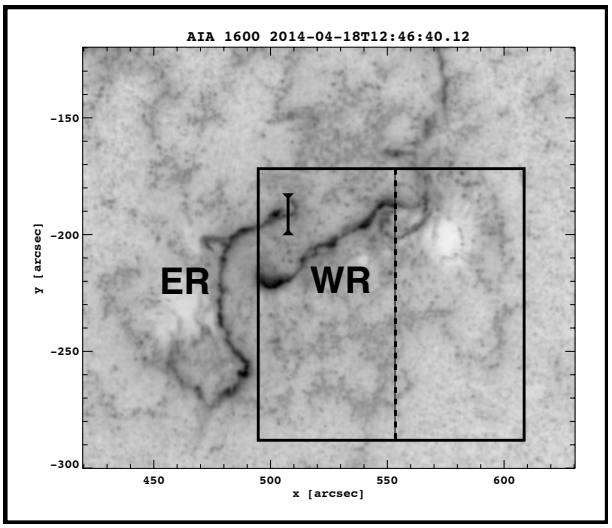


Figure 3.1. SDO/AIA 1600 Å image of the flare ribbons, in reversed $\log_{10}$ black–white (RLBW). The black inset box is the positioning of the IRIS SJI FOV, and the vertical black dashed line is the IRIS SG slit position. The east and west ribbons are indicated by "ER" and "WR", respectively. The black "I"-shaped line is an artificial slit discussed in Section 3.3.5.

Figure 3.1 (note that the color scale is a reversed $\log_{10}$ black–white (RLBW), with white as lowest intensity and black as highest intensity). We have labeled the east and west ribbons accordingly as "ER" and "WR", and we refer to the ribbons as such throughout the text. Both ribbons generally follow a single distinct path from southeast to northwest, although the ER is more strongly tilted toward a north–south orientation. There are also occasional offshoots and patchy regions of intensity which evolve with time.

One notable exception to the general SE-to-NW single-track ribbon paths can be seen in the WR starting at around 550″ West and 200″ South (Figure 3.1). At this point, moving SE to NW, the ribbon clearly splits into two channels which merge

back together farther to the NW, resulting in an isolated island between the ribbon channels. This split ribbon feature persists over most of the evolution of the flare and appears in both SDO/AIA 1600 Å and IRIS SJI 1400 Å, but does not appear in the SDO/AIA 171 Å passband. The most likely origin of this feature can be seen in the SDO/HMI magnetogram for this region taken in the middle of the flare duration (12:58:19 UT) as shown in Figure 3.2, where positive and negative LOS polarity are colored white and black, respectively, and the ER and WR positions are traced for context as the white and black lines. In the center of the split WR island we observe a significant neutral gap running diagonally through the positive magnetic region centered at 575″ West and 200″ South. The split 1600 Å ribbon appears to track around either side of this neutral channel.

There is also a prominent arcade of coronal loops which appears in the SDO/AIA 171 Å passband approximately 30 minutes after the first appearance of the flare ribbons. Figure 3.3 (also RLBW) shows a 171 Å image of the flare region taken at 13:12:37 UT showing the flare ribbons shortly after they first appear. For comparison with Figure 3.1 we have traced the position of the ribbons as jagged white lines. The loops visible in Figure 3.3 all follow roughly E to W paths between the two ribbons, although the exact loop connections between the ER and WR are not easy to establish because of the time delay for the appearance of the loops in this passband. We also searched for loops at earlier times using higher temperature SDO/AIA passbands,

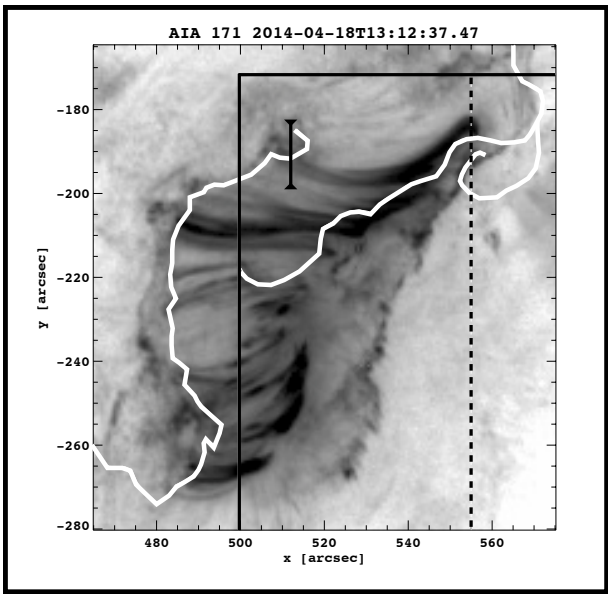


Figure 3.2. SDO/HMI magnetogram of the flare active region, with standard colors. The balck inset box is the positioning of the IRIS SJI FOV, and the vertical black dashed line is the IRIS SG slit position. The black and white solid lines trace the west (WR) and east (ER) ribbons from Figure 3.1.

such as 131 Å and 193 Å, but saturation and lack of sharpness in these passbands relative to 171 Å impedes clear identification. Our main use for the AIA imaging data is to identify magnetic conjugacy. We use 171 Å images for this because they are sharpest and will probably extend to the lowest points along the loops. The 171 Å image clearly indicates a dipolar component to the magnetic geometry, which we confirm with the SDO/HMI magnetogram in Figure 3.2. We clearly see two dominant polarities, negative to the east and positive to the west, which the ribbons track quite closely and which are connected by the flare loops. Finally, we note there was a coronal mass ejection (CME) associated with this flare (observed by LASCO); the

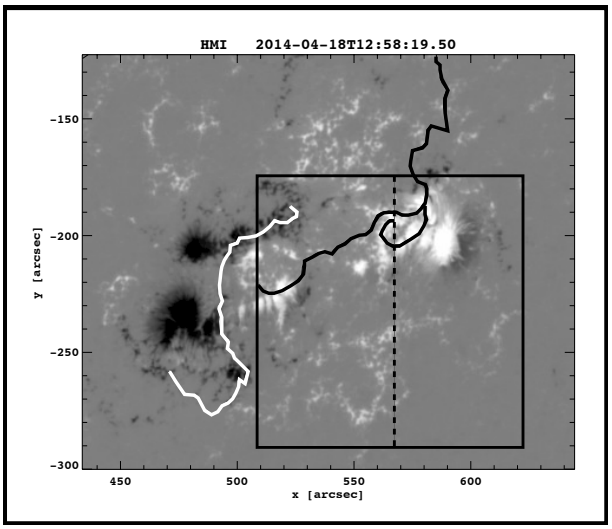


Figure 3.3. SDO/AIA 171 Å image of the post-flare loops and ribbons, in RLBW. The black inset box is the positioning of the IRIS SJI FOV, and the vertical black dashed line is the IRIS SG slit position. The solid white lines trace the position of the SDO/AIA 1600 ribbons from Figure 3.1, and the black "I"-shaped line is an artificial slit discussed in Section 3.3.5.

flux rope eruption responsible for the CME is discussed in more detail in Cheng et al. (2015).

The IRIS SG data we use for this study is drawn from a sit-and-stare observation (i.e. no rastering of the SG slit) which began at 12:33:38 UT, shortly after the GOES start time for the flare, and which continued until 17:18:10 UT. This observation thus covers nearly all of the impulsive rise phase and the entire decay phase of the flare. The SG cadence for this observation was ∼9 s, while the SJI cadence for 1400 Å was ∼27 s, and the SJI FOV was initially centered at 550″ West, 230″ South (note that the spatial metric at this position on the disk is ∼900 km/arcsec). An example SJI 1400 Å image, taken at 12:46:34 UT (approximately the same time as Figure 3.1),

is shown in Figure 3.4 (we again use RLBW). For context, note that the IRIS SJI FOV is shown as a black inset box in Figures 3.1–3.2, and that the IRIS SG slit position is indicated in those three figures by a vertical dashed black line. Finally, note that the IRIS SG slit is conveniently positioned across the WR, directly over the location of the magnetic gap and ribbon island mentioned above. In summary, the slit placement, high cadence, and consistently stable rotation tracking during this observation make it ideal for a spectroscopic study of the fine structure of flare ribbons and its evolution.

3.2.3. Wavelength Correction

The rest wavelengths of spectral lines for the IRIS SG are generally dynamically shifted to some degree due to the orbital motion and thermal variations of the IRIS spacecraft and must be corrected for every spectrograph exposure. To do this we use the SSWIDL routine `iris_orbitvar_corr_l2`, which fits the Ni I 2799.474 Å line to determine the appropriate wavelength shifts for the FUV bandpass (De Pontieu et al., 2014). Even after applying this correction, however, we find that the peak of the O I 1355.598 Å is systematically redshifted during the observation by ∼0.01 Å, even though as a photospheric line it should generally be stationary. We therefore subtract this additional shift from the FUV wavelength axis to make the O I line stationary, and subsequently reference all other lines to their CHIANTI database line centers (IRIS Technical Note 20).

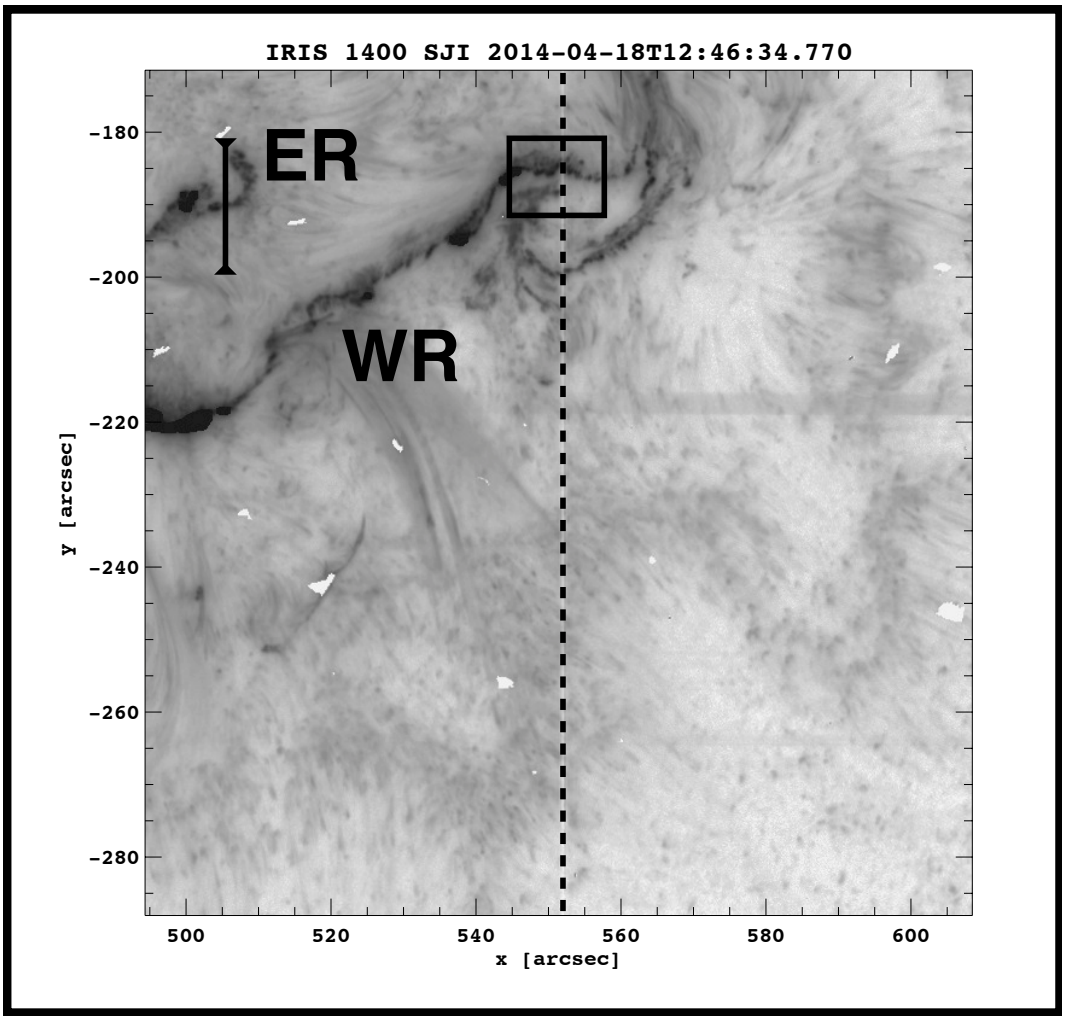


Figure 3.4. An image of the flare ribbons from the IRIS 1400 Å SJI, in RLBW, corresponding to the black inset boxes for Figures 3.1–3.2. The east and west ribbons are indicated by "ER" and "WR", respectively. The vertical black dashed line is the IRIS SG slit, and the black inset box outlines where the WR crosses the slit and the positioning of the frames for Figure 3.5. The black "I"-shaped line is an artificial slit discussed in Section 3.3.5.

3.3. Results

3.3.1. Ribbon Evolution

The flare ribbon appears as an intense band in the northern portion of the IRIS SJI beginning around 12:46:34 UT. The overall orientation of the WR is from SE to NW, and in the vicinity of the SG slit the ribbon is running very nearly due E–W, across and perpendicular to the slit. As the WR evolves it slowly drifts S, generally maintaining its perpendicular orientation to the slit. This motion is away from the polarity inversion line (PIL), in agreement with the classic picture of ribbon spreading (Kopp & Pneumann, 1976). Figure 3.5 shows a series of 16 images from the SJI 1400 Å passband, taken from the black inset box near the top of Figure 3.4, at ∼1 minutes intervals starting at 12:46:34 UT (the same time as Figure 3.4) and continuing to 13:00:41 UT. The color scale is RLBW. The inset frame has been chosen to cover the area of the SJI where the northern branch of the WR crosses the SG slit. The reader should note that the time axis for these 16 frames runs from left-to-right in the top row, then right-to-left in the second row, and so on row-to-row as indicated by the arrows to form a movie of the ribbon evolution. The SG slit can be seen as a pale line running down the middle of each frame, with the upper fiducial just visible at the bottom of each frame. Intermittent saturated pixels appear to the left of the slit in some frames (for example, 12:52:41 UT).

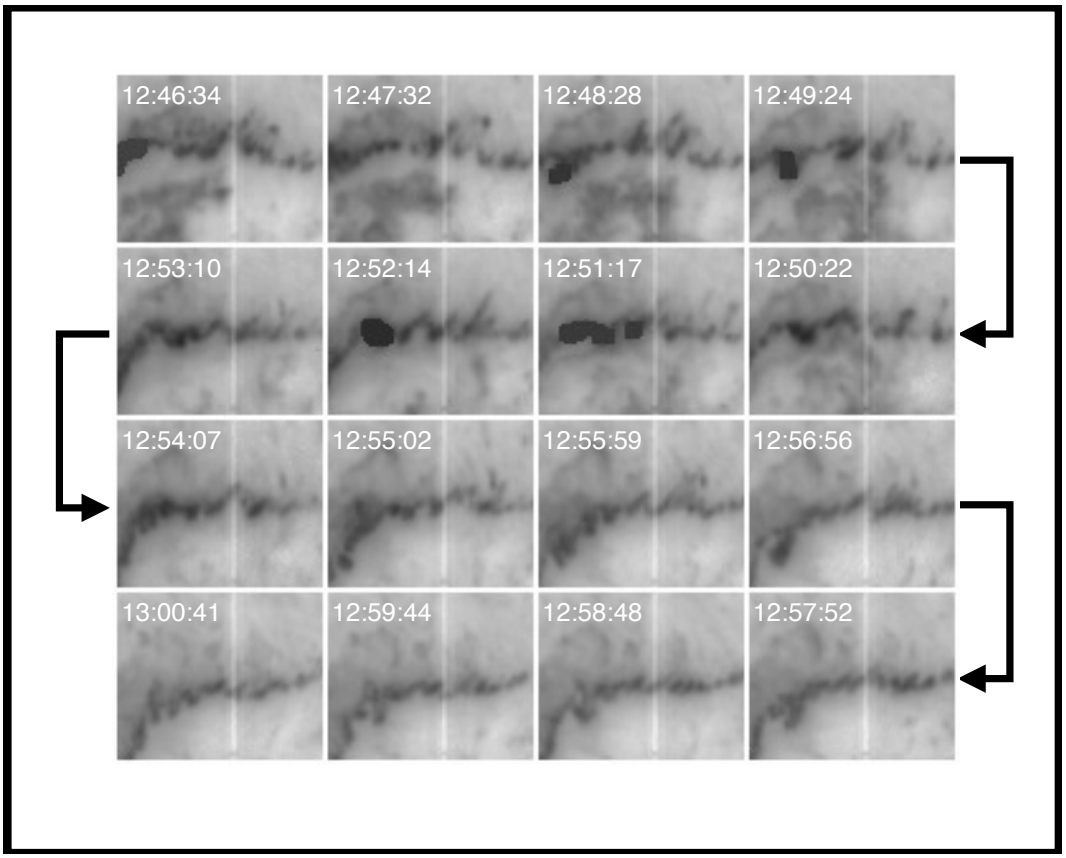


Figure 3.5. Time series of SJI 1400 Å images, for the inset box in Figure 3.4, showing the evolution of the flare ribbon in ∼1 minute intervals beginning at 12:46:34 UT, in RLBW. Time for each image is displayed at upper left for each frame. Note that time runs from left-to-right in the first row, then right-to-left in the second row, and continues to alternate down the rows, as indicated by the arrows.

In addition to the large-scale evolution of the ribbon shown in Figure 3.5, we also note a distinct substructure that evolves on a smaller scale and at a faster rate than the overall ribbon motion. This substructure appears in most frames as a jagged sawtooth pattern that cuts across the slit, with multiple patches of bright emission oriented diagonally to the slit that break up the ribbon. A very similar structure was observed by Li & Zhang (2015) and called "slipping reconnection" by them. Since this term also refers to a model (Aulanier et al., 2006), which may or may not be pertinent to the observation, we use the term sawtooth here instead. Times at which this pattern appears most prominent include 12:50:49 UT, 12:52:14 UT, and 12:55:32 UT. An inspection of this sawtooth pattern from frame-to-frame reveals that the diagonal features appear to slide across the slit from east to west as the ribbon drifts south over time. Our best estimate of its pattern speed is $v_{st} \approx 15$ km s^{-1}, parallel to the ribbon itself. One example where this is most readily apparent occurs between 12:53:38 and 12:55:32 UT. In these three frames a diagonal sawtooth begins just to the left of the slit, moves west such that one minute later it is crossing the slit, and one minute after that is seen on the right side of the slit.

Since the sawtooth pattern in the SJI 1400 Å is moving across the SG slit, we would expect the pattern to also be reflected in spectral intensity for the Si IV 1403 Å passband. To calculate the total intensity in this passband, we first divide the data for each SG frame by the appropriate exposure time to obtain normalized units of

DN s^{-1}. We then reset all negative values in the passband (which occur near the passband edges) to 0, and finally sum the data over the entire Si IV 1403 Å passband. In the upper plot of Figure 3.6 we show the resulting time-distance stackplot for the time range 12:45 UT to 13:05 UT. The y-axis shows the heliographic position of the slit pixels at at the beginning of the observation; there is some wobble to y-pointing of the instrument, but it is less than $0.3''$ over the entire observation. Data values vary between 20 DN s^{-1} and 64000 DN s^{-1}. We again note the southward motion of the ribbon, beginning at $\sim 184''$ S and subsequently moving south to $\sim 188''$ S. We also observe immediately that the sawtooth pattern is indeed present in the SG data starting around 12:48 UT and ending at around 13:02 UT, and that three teeth in particular can be clearly seen between 12:51 UT and 13:01 UT. There is also a feature that moves up from the south beginning at around 12:47 UT, however this is a piece of the northward-moving southern branch and not part of the ribbon sawtooth structure.

In the lower plot of Figure 3.6, we have replotted the intensity stackplot (with the time axis in seconds this time), and we have overlaid a red contour line around the section of the ribbon emission for which the sawtooth pattern is the clearest. Henceforth, when referring to the "sawtooth", we will be referring to this outlined region of pixels. The numbers 1–6 indicate six peaks in the sawtooth oscillation, with dashed lines also indicating the approximate beginning time of a southward motion

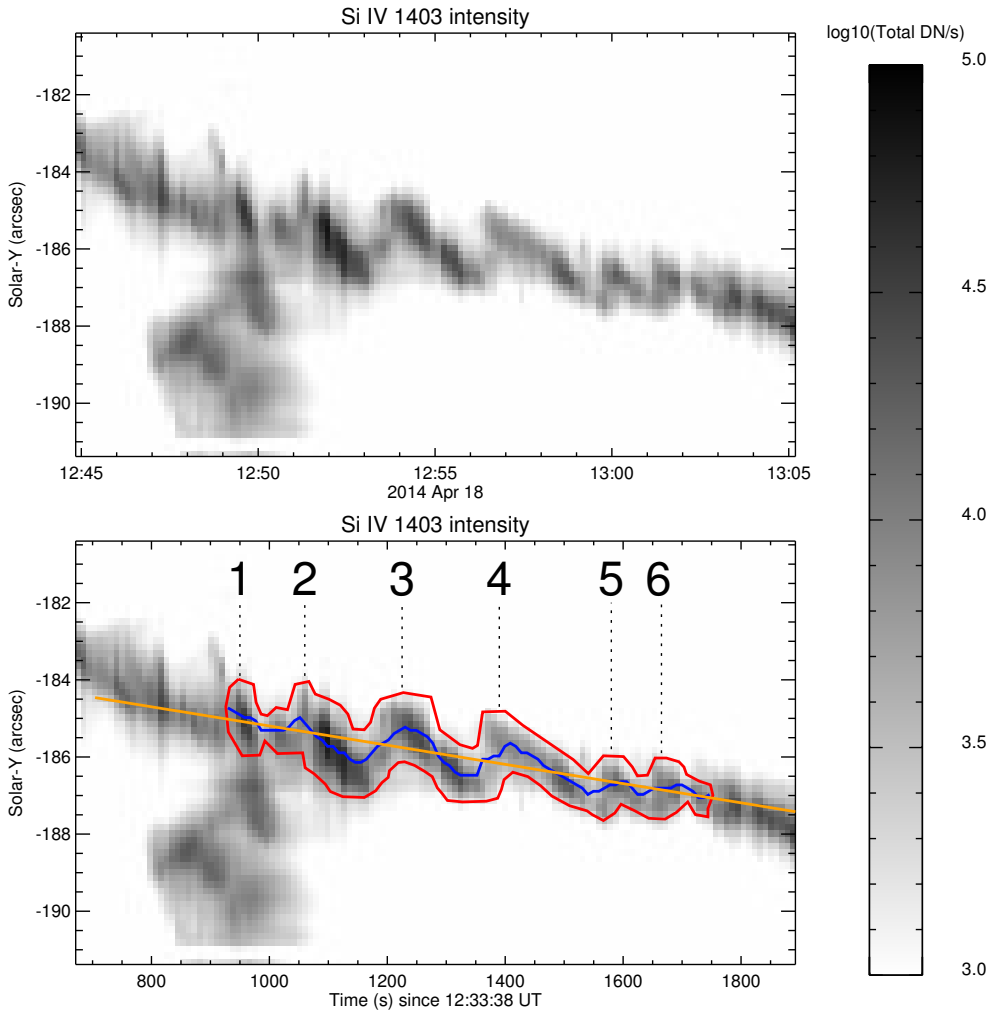


Figure 3.6. Upper panel: time-distance stackplot of the total Si IV 1403 Å SG passband intensity, in RLBW. Time is given on the x-axis in UT, and the y-axis is solar-Y in arcsec. Intensity scale is given to the right. Lower panel: reprint of the upper panel with a red outline indicating the position of the sawtooth pattern described in Section 3.3.1. Time is given on the x-axis in s (after 12:33:38 UT), and the y-axis is unchanged. The blue line indicates the sawtooth centroid position, and the orange line is a linear fit to the blue line. The numbers 1–6 indicate six peaks in the sawtooth oscillation.

in the sawtooth. The oscillation period varies between 80 and 190 s, averaging ∼140 s, consistent with sawtooth structures ∼2 Mm long moving across the slit at ∼15 km s^{-1}. We have also overlaid the sawtooth centroid position (as a function of time) as the blue line, as well as a linear best fit to the sawtooth mean as the orange line. The linear fit has a southward velocity of 1.6 km/sec, while the mean position moves at velocities ranging from ±20 km/s. This confirms the much faster motion of the sawtooth substructure relative to the overall ribbon motion. Finally, we observe that the shallow sides of the sawtooth pattern are all directed away from the PIL located between the ER and the WR.

3.3.2. Spectral Line Fitting

The WR sawtooth substructure is seen in the 1400 Å SJI passband. These images are dominated by the two Si IV lines (1394 Å and 1403 Å) which are recorded in the IRIS SG FUV 2 range (De Pontieu et al., 2014). These two lines are ideal for examining flare ribbon plasma, since at ∼80,000 K they are located within the transition region at the footpoints of the flaring loops. Additionally, they are typically strong lines that dominate their respective spectral regions and therefore are easily distinguished from the lines of other ion species. In Figure 3.7 we have plotted the exposure-normalized data for the two lines for several representative positions and times in and around the sawtooth pattern: 1394 Å as asterisks and 1403 Å as squares. The x-axes are in units of km s^{-1} with $v = 0$ referring to the rest wavelength defined

as described above, where redshifts and blueshifts are defined as positive and negative velocities respectively. The y-axis is arbitrarily scaled for each pixel, and the time appears to the left of each plot. At the upper right is the outline of the sawtooth from Figure 3.6, with "+" symbols arranged in five rows "A"–"E", corresponding to a row of spectral plots, which indicate the position and time of each spectral plot. Finally, note that the 1394 Å data have all been scaled by a factor of 0.5, so that the two spectral lines will appear on the same scale (and see the final paragraph of this section for more detail on this choice).

The positions and times (henceforth "pixels") chosen for Figure 3.7 have been chosen to illustrate several general features of the Si IV spectral lines in this event. First, the majority of the pixels within the sawtooth appear to contain two Gaussian components, as first noted by Cheng et al. (2015) in the early ribbon development. The two components are present for both the 1394 Å and the 1403 Å lines, clearly demonstrating that both components are from Si IV and not from an accidental blend with another spectral line. A fraction of pixels late in the sawtooth contain one or more additional components; however, these occur only in a minority of cases and typically have small amplitude compared to the two dominant components. The lack of additional components, or of significant non-Gaussian tails in the spectral lines, suggests that the IRIS SG is not observing many separate loop footpoints within a single pixel, but rather only one or two distinct footpoints. We also observe that each

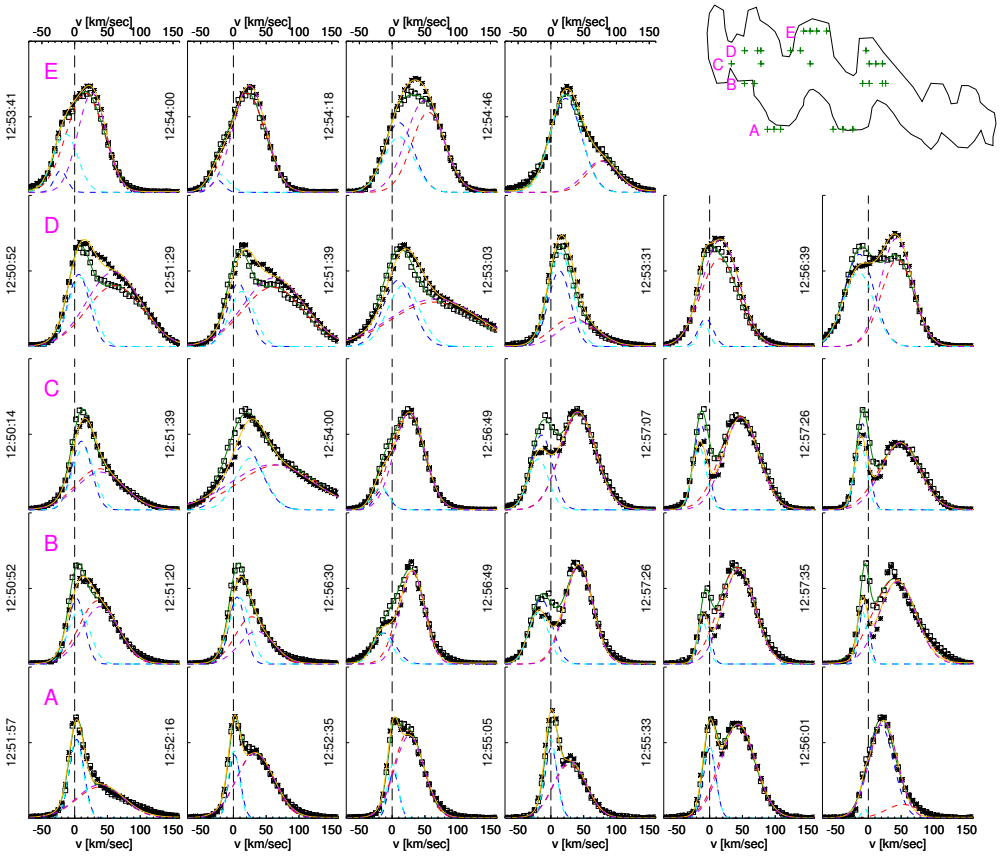


Figure 3.7. Selected Si IV spectral lines for 28 pixels in or near the sawtooth pattern shown in Figure 3.6. An outline of the sawtooth is shown at upper right, and the five rows of plots "A"–"E" each sample a given spatial position at several different times, as indicated by the "+" symbols at upper right. Each plot displays the spectrograph data for Si IV 1394 Å (as asterisks) and 1403 Å (as squares), with the time printed to the right of each plot. The x-axis is in km s^{-1} from nominal line center (same for both lines), and the y-axis scaling is arbitrary (the 1394 Å data has been scaled by a factor of 0.5 for direct comparison to the 1403 Å line). Additionally, the solid orange (green) lines are the two component Gaussian fits for the 1394 Å (1403 Å) spectral line, as described in Section 3.3.2. The dashed lines are the individual components C_B and C_R for each of the Si IV spectral lines, with cyan/violet used for the respective 1394 Å spectral components and blue/red used for the respective 1403 Å spectral components.

component appears to persist and to evolve within its row. Both components are Doppler-shifted, with one component consistently redshifted and the other switching between redshift and blueshift, and both the Doppler shift and the velocity separation between the components evolves with time. Finally, we note that neither component consistently dominates, and for some pixels they have comparable magnitude.

Within the sawtooth, there are numerous cases where at least one, and sometimes both, of the Si IV lines saturate the IRIS SG pixels. This is true for $\sim$17% of pixels for 1394 Å and $\sim$5% of pixels for 1403 Å, and makes accurately fitting a two-component Gaussian problematic. Except for saturation, however, most positions display behavior similar to that discussed above, although we discuss some additional discrepancies below. We therefore assume that a two-component Gaussian will be appropriate for the majority of the pixels within the sawtooth.

Since there are too many positions and times within the sawtooth to manually supervise the fitting, we have developed an automated procedure for eliminating poor fits. We note first that the chi-squared measure for the fits were found not to neatly discriminate between fits which were deemed good and bad by visual inspection. Therefore, in our procedure the two-component fit is rejected if any one of the following criteria are met for either component:

1. any pixel in the band is greater than 2000 DN s^{-1} (approximate saturation limit);

2. the Gaussian amplitude is less than 10 DN s^{-1};

3. the line center is greater than ± 0.625 Å ($\sim$134 km s^{-1}) from the rest wavelength;

4. the Gaussian width is greater than 0.625 Å.

We find that $\sim$21% of 1394 Å and $\sim$7% of 1403 Å attempted fits are rejected using this method; roughly two-thirds of these rejections are due to condition 1, while the rest are from the other three conditions. Because of the greater percentage of successful fits for 1403 Å, we will use only that spectral line for the remainder of the analysis starting in Section 3.3.3. In a small number (<1%) of cases, only one component is the cause of the rejected fit; however, due to the rarity of these cases, we simply reject both components. Finally, the two components are sorted according to their Doppler shifts, and we label the bluer component C_B and the redder component C_R.

In Figure 3.7 we have plotted the resulting two-component Gaussian fits for the 28 selected pixels over the data for those pixels, for both the 1394 Å (as the solid orange curve) and the 1403 Å (as the solid green curve) spectral lines. The dashed lines correspond to the individual components C_B and C_R for each of the Si IV spectral lines, with cyan/violet used for the respective 1394 Å spectral components and blue/red used for the respective 1403 Å spectral components. We note that our criteria are generally adequate to reject bad fits, and the fits that remain conform to the data for both spectral lines quite well. We also note that the fit parameters of the two

components are generally similar for both spectral lines, which adds confidence that the fitting procedure is finding the same two major components. We find that C_B is generally narrower than C_R (for $\sim$88% of pixels). The average non-thermal widths, given by $\sigma_{\rm nt} = \sqrt{\sigma^2 - \sigma_{\rm th}^2 - \sigma_{\rm inst}}$ where $\sigma_{\rm th} = 6.86$ km s^{-1} and $\sigma_{\rm inst} = 3.9$ km s^{-1} (De Pontieu et al., 2015), for the two components are $\sigma_{\rm nt}^{\rm B} = 19$ km s^{-1} and $\sigma_{\rm nt}^{\rm R} = 38$ km s^{-1}. We note that the non-thermal widths for C_B are quite consistent with those found in quiescent active regions (De Pontieu et al., 2015) whereas C_R shows much greater broadening, but we will defer discussion of this fact until later.

In an optically-thin plasma without geometrical effects, the 1394 Å and 1403 Å Si IV lines will have a 2:1 intensity ratio (Mathioudakis et al., 1999). The majority of the sawtooth pixels display this 2:1 ratio: e.g. the majority of the scaled data for rows A, D, and E all lie on top of each other. Some pixels, however, depart from the strict 2:1 line ratio, suggesting some optical depth effects. This departure is more common in C_B, especially when it is very narrow, as in rows B and C. It can also occur in C_R, as it does in row D. In some cases the line ratio is less than two, while in other it is greater (as in C_R of row D). The former situation is commonly attributed to loss from the thicker line (1394 Å) by scattering out of the line of sight (Mathioudakis et al., 1999). The latter can occur in more complicated geometry when photons are scattered *into* the line of sight (Kerr et al., 2005). The fact that we observe both cases in neighboring pixels suggests, not surprisingly, that the emitting plasma has a

complex geometrical structure over scales comparable to the IRIS resolution. Almost all optical-depths effects we observe are similar to those shown in rows B, C and D. The line ratio remains very close to the optically thin value of 2:1, and the thicker component (1394 Å) is still well fit by a Gaussian. We therefore conclude that Si IV is never far from being optically thin and that Doppler shifts and line width are well measured by the Gaussian fit.

3.3.3. Doppler Velocities

In Figure 3.8, we plot the Doppler velocities determined above for both components using a blue–red color scale on time-distance stackplots (C_B in the upper panel and C_R in the lower panel). The time axes follow the same labeling scheme as in Figure 3.6, and the blue–red color range runs between ± 40 km s^{-1} for C_B and between ± 80 km s^{-1} for C_R (in this system, we define redshifts as positive and blueshifts as negative). We have also outlined the sawtooth pattern from Figure 3.6 with the solid black line to help guide the reader in determining the relative position of features. Finally, we have color-coded any pixels not fit (for any reason) by the above automatic routine as gray.

There are several important features to note in the Doppler velocity data, mostly for component C_B. The first is that, as mentioned above, the Doppler shifts for component C_B are sometimes red and sometimes blue. However, we now observe that these shifts are not random, but are clustered into large regions of redshift and

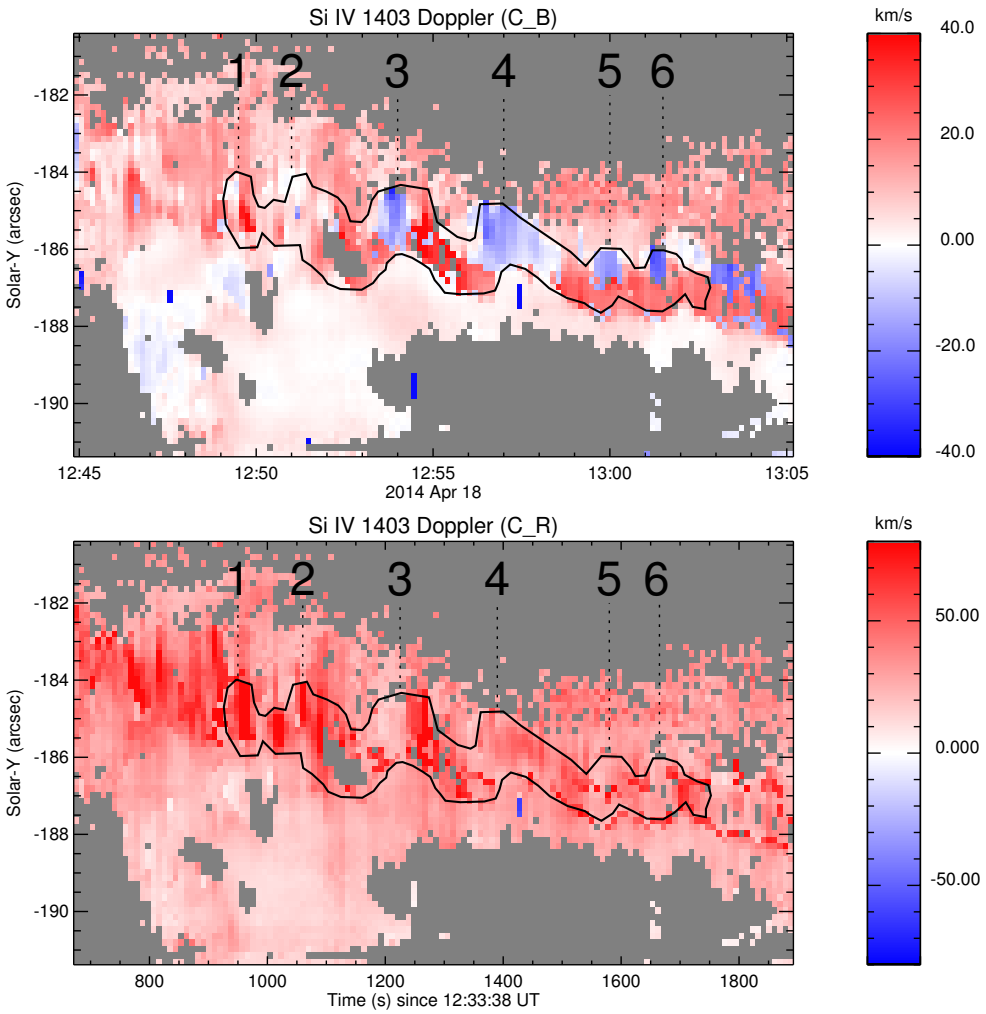


Figure 3.8. Time-distance stackplot of Doppler velocity for components C_B (upper panel) and C_R (lower panel) of the Si IV 1403 Å spectral line. Time is given on the x-axis in UT for the upper panel and in s after 12:33:38 UT for the lower panel. The y-axis for both panels is solar-Y in arcsec. Velocity scale is given to the right of each panel (scaled ± 40 km s^{-1} for C_B and ± 80 km s^{-1} for C_R). Black outline indicates the position of the sawtooth pattern, and gray pixels indicate discarded fits (as described in Section 3.3.2).

blueshift. Additionally, we note that the blueshifts tend to be concentrated near the upswings and peaks in the sawtooth pattern, whereas the redshifts tend to be on the downswings and troughs (particularly prominent in the teeth marked "3" and "4"). Although it is not as apparent, this same pattern is reflected in component C_R, except that the redshift is merely weakened instead of shifted to the blue.

A different method of visualizing the velocity evolution is to plot the Doppler velocities for all positions in a single time slice of the sawtooth as a function of time, as we have in Figure 3.9. Components C_B and C_R are displayed as the black squares and asterisks, respectively, and the mean velocity within each column is plotted as the solid blue (for C_B) and red (for C_R) lines. In this format we can clearly observe that, starting at ∼1100 s, there begins a distinct red–blue oscillation in C_B, apparent in the mean velocity, which continues for at least three full periods of 100–200 s and amplitude ± 20 km s^{-1}. Finally, we note that there is a similar oscillation in the redshifted C_R Doppler velocity, which is noisier than for C_B but still clearly at the same frequency as and in phase with the C_B oscillation. The similar frequency and phase of these Doppler oscillations strongly suggests that both Si IV components are being shifted by a common motion of the plasma.

3.3.4. Additional Spectral Lines

There are two additional pairs of spectral lines included in the IRIS SG that are of use for observing the upper chromosphere and TR. One pair is the O IV 1400 Å

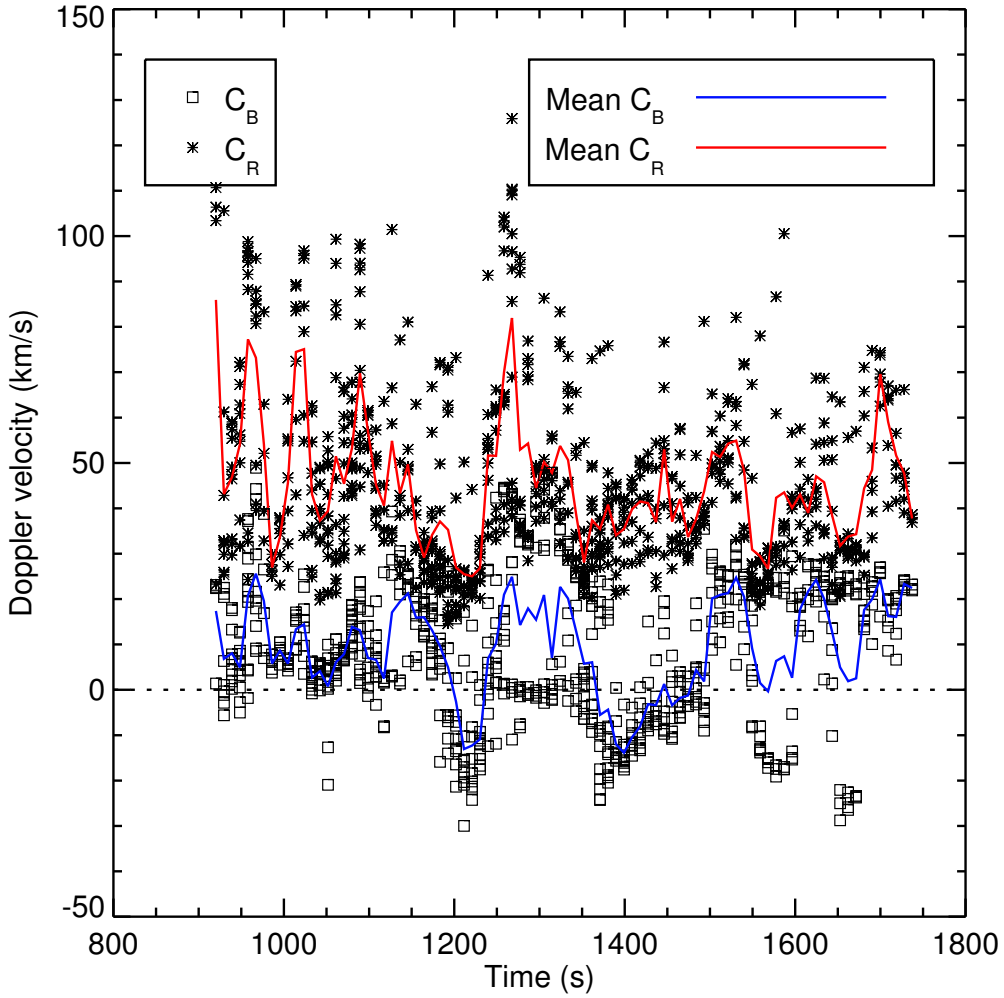


Figure 3.9. Plot of the Doppler velocities (in km s^{-1}) for the two Si IV 1403 Å components for all pixels within the sawtooth as a function of time (given in s after 12:33:38 UT). The black squares (asterisks) are the Doppler velocities for component C_B (C_R), and the solid blue (red) lines are the mean Doppler velocity for component C_B (C_R) for all positions at a given time.

and 1401 Å lines included in the FUV 2 passband. These lines are formed higher in the TR than the Si IV lines, at ∼150,000 K, and as forbidden lines they are often of use for determining the plasma density at that temperature (Flower & Nussbaumer, 1975). We find that the time-distance stackplot of the O IV 1401 Å total line intensity is virtually indistinguishable in structure from that of Si IV 1403 Å, with the sawtooth pattern appearing at an identical position and time. Unlike the Si IV profiles discussed above, however, neither of the O IV lines have any obvious two-component structure and appear generally well-fit by a single Gaussian. This may be because the O IV lines have count rates significantly lower than the Si IV lines, or it may be due to the specifics of the formation mechanism for the forbidden O IV lines. Although we do not discuss it further in this work, we find that the single component O IV 1401 Å Doppler shifts generally follow that of component C_B of Si IV 1403 Å, with similar magnitudes of blueshifts and redshifts located in the same parts of the sawtooth.

The other pair of lines are the C II 1335 Å and 1336 Å lines in the FUV 1 passband. These lines are formed in the upper chromosphere, at ∼20,000 K, and are thus expected to be (somewhat) closer to the footpoint than Si IV and generally will not display the same dynamics. However, we find that C II 1335 Å and 1336 Å lines also display nearly identical behavior to Si IV, with the sawtooth intensity pattern appearing over the same spatial and temporal scales. We also find that both C II lines possess two-component Gaussian profiles, as was noted in Cheng et al. (2015),

and although we did not perform the same detailed analysis of the Doppler shifts we note that these components display very similar shifts to the Si IV lines at a several selected pixels within the sawtooth.

3.3.5. East Ribbon

Although the IRIS SG FOV only allows for spectral analysis of the WR, we note that the northern end of the ER was located within the IRIS SJI 1400 Å FOV (Figure 3.4). From the 171 Å SDO/AIA image in Figure 3.3, we observe a set of flare loops that emerge from the WR at the IRIS SG slit location which curve first North and then South and West to end at the ER at the location indicated in that figure by a vertical black "I"-shaped line crossing the ER. We extract an artificial SJI slit, one pixel wide and located along the vertical black "I"-shaped lines in Figures 3.1 & 3.4, to investigate the ER intensity behavior in the same manner as the WR. The resulting intensity time-distance stackplot is shown in the middle panel of Figure 3.10, with the original SG stackplot from Figure 3.6 plotted in the bottom panel.

We note immediately that there are two diagonal bands that begin at very nearly the same times as the peaks marked "3" and "4" in the original sawtooth. Of course, the lower time resolution of the SJI ($\sim$27 s) means that any features in time are somewhat less clear than for the $\sim$9 s cadence SG. However, the SJI bands both begin within 60 s of their companion SG sawtooth features, and their duration (120-180 s) and spatial extent (2-3″) are nearly identical. We also note that the slow

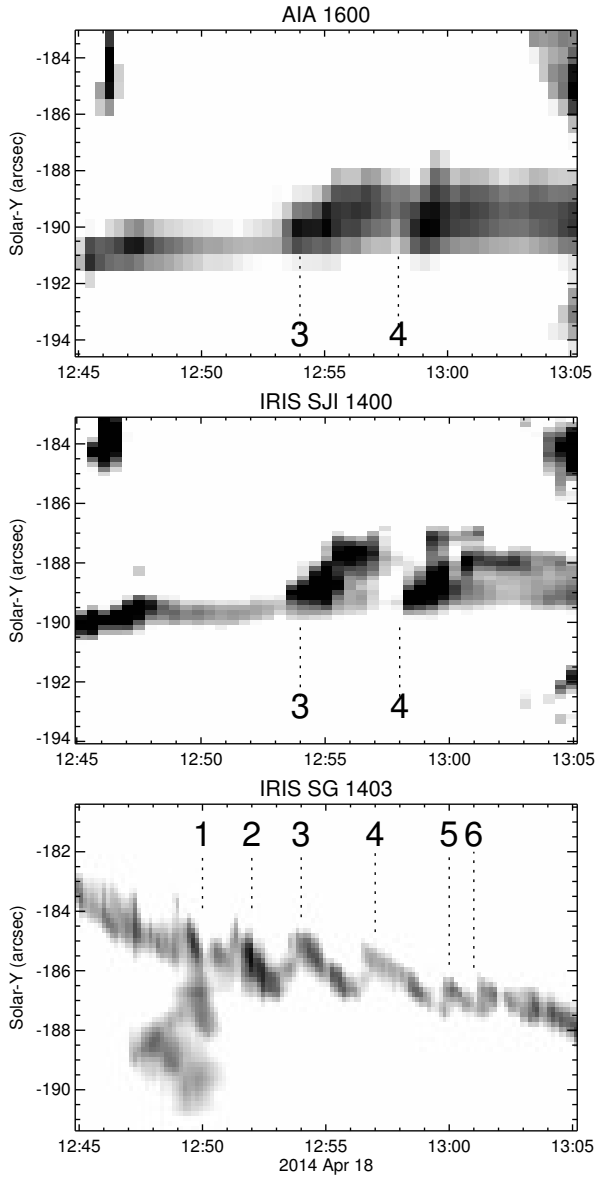


Figure 3.10. Upper panel: Time-distance stack plot of SDO/AIA 1600 Å intensity for a vertical artificial slit across the ER (shown in Figures 3.1 and 3.4), as described in Section 3.3.5, with labels for the sawteeth "3" and "4". Middle panel: Time-distance stack plot of IRIS SJI 1400 Å intensity for a vertical artificial slit across the ER (shown in Figures 3.1 and 3.4), as described in Section 3.3.5, with labels for the sawteeth "3" and "4". Lower panel: Reprint of the time-distance stackplot for total 1403 Å intensity from Figure 3.6 with sawtooth labels. Time in all panels is in UT.

motion of the band is also directed away from the PIL, as it was for the SG sawtooth, indicating that the phase of these features is the same.

We repeat this procedure using the co-aligned AIA 1600 data, which is often dominated by the C IV lines at 1548 Å and 1550 Å (Lemen et al., 2012). These lines are formed at ∼100,000 K, slightly hotter than for Si IV. The resulting intensity stackplot is shown in the top panel of Figure 3.10. Once again, we note that the lower spatial (0″.5) and temporal (24 s) resolutions smear out the features, but we can still make out the same diagonal bands marked "3" and "4" at approximately the same positions and times as before. Obviously, we cannot be absolutely certain that these ER footpoints are conjugate to the WR footpoints in the IRIS SG. We also note that the bands present in the ER are not completely identical to the sawtooth in the WT, and that the oscillations "1", "2", "5", and "6" from the WR sawtooth are conspicuously missing in the ER. Further, those oscillations do not appear for any other artificial slit positions on either side of the position shown, and as the artificial slit is moved away from that position the two oscillations that do appear are not as apparent. This indicates some degree of asymmetry between the two ribbons. However, we are fairly confident stating that the conjugate behavior of the intensity stackplots indicates that both ribbons are experiencing the same oscillation, and that the close relationship we observe between the ER and WR strongly implicates a source somewhere high in the corona. We therefore rule out any local mechanism, such as

p-mode oscillations (Li & Zhang, 2015), which would not be linked by the coronal magnetic field.

3.4. Interpretation

In the upper panel of Figure 3.11 we have plotted the mean C_B Doppler velocity in km s^{-1}, determined in Section 3.3.3 and shown in Figure 3.9, against the relative difference in arcsec of the mean sawtooth position from the linear fit (effectively the orange line subtracted from the blue line in Figure 3.6). The result is a phase portrait for the sawtooth ribbon oscillations. Note that the actual sawtooth data are represented in the plot by the colored squares, with the connecting colored lines added to guide the reader. Time is encoded by the color of the squares and connecting lines starting with purple at the beginning of the sawtooth and ending with red, as shown by the color bar on the right side of the figure.

The central feature of this phase portrait is that, despite some meandering of the data, many of the data appear to lie along the diagonal that runs from upper left to lower right. The solid black line represents a linear fit to the full data set within the sawtooth, and gives an overall slope of ∼14 s (using ∼900 km/arcsec). However, we note that the diagonal trend becomes more apparent when we consider only individual pieces of the sawtooth. In particular, in the lower panel of Figure 3.11, we have grayed-out all the data except that for sawtooth "4" in Figures 3.6 and 3.8

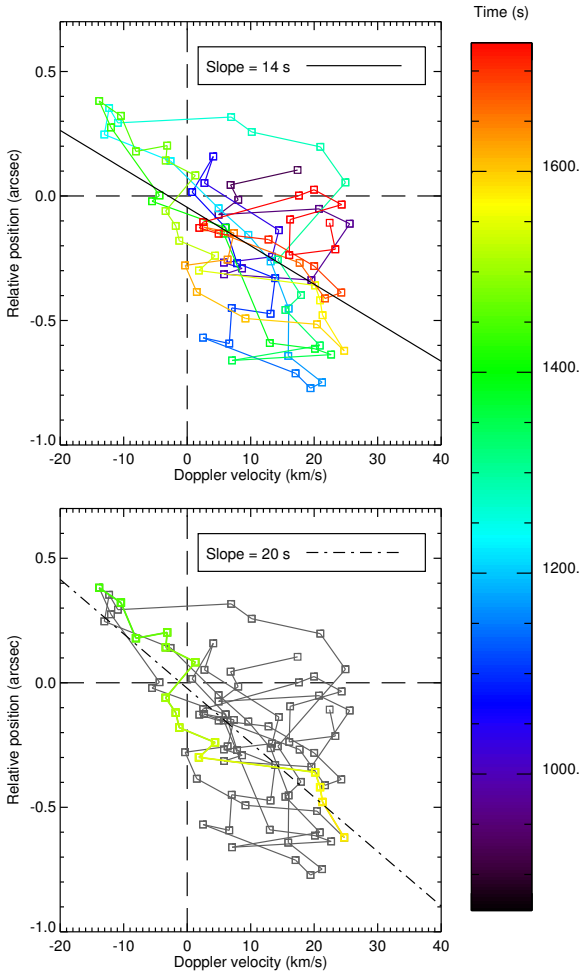


Figure 3.11. Upper panel: phase portrait of the mean Doppler velocity of component C_B (blue line from Figure 3.9) and the relative sawtooth position (orange line subtracted from the blue line from Figure 3.6). Data is indicated by the squares, and the connecting lines are to guide the reader. Time is indicated by the color of the squares and connecting lines, and is indicated by the color bar at right. The solid black line is a linear fit to all data. Lower panel: same, but with only the data for sawtooth "4" colored (all other data in gray). The dash-dotted line is a linear fit to the sawtooth "4" data points.

(beginning at ∼1400 s and ending at ∼1520 s). These data are clearly aligned along a diagonal trend, and the dash-dotted line represents a linear fit to just these data with a slope of ∼20 s. In the context of the discussion so far, the diagonal trend makes sense: the strongest blue and red Doppler shifts tend to be concentrated respectively at the peaks and troughs of the sawtooth pattern. The phase portrait presented in Figure 3.11 therefore reveals a critical property of the ribbon substructure. Namely, that the LOS Doppler velocity and the position of the sawtooth pattern are 180° out-of-phase.

Before presenting our proposed scenario for the generation of the sawtooth pattern, we first consider two alternative scenarios that would be probably serve as the most obvious first candidates. The first scenario is a simple harmonic oscillation (SHO), where the loop is waving forward and back within a plane. This could come from a linearly polarized loop oscillation and would create redshifts and blueshifts in the loop plasma as the loop motion carries it toward or away from the observer. However, these Doppler shifts would occur only as the loop was moving from North to South or from South to North, and cannot account for the Doppler shifts at the peaks and troughs of the wave. We also note that the phase portrait for an SHO is an ellipse in position-velocity space, resulting from the 90° phase difference between position and velocity. The SHO scenario is therefore inconsistent with the results from the ribbon sawtooth.

The second scenario which we consider is also an SHO ribbon oscillation, but instead of the loop motion creating the Doppler shifts it simply modulates pre-existing plasma velocities within the loop. In this scenario, the loop tilts first toward and then away from the observer, the Doppler shifts of plasma flowing along the loop would be changed from red to blue (or vice versa, depending on the flow direction). Assuming the correct conditions, this modulation could provide the correct 180° phase difference. It is readily seen, however, that this scenario requires the loop oscillation to be at least partly on the far side of 90° inclination from the LOS, in order to switch the sign of the Doppler shift. From the 45-minute HMI vector magnetogram at 12:58:19 UT we find that the magnetic field in the sawtooth region is angled only ∼40° from the LOS. This would require a substantial (>50°) oscillation in order to switch the Doppler shifts, which does not seem reasonable given the observations.

The 180° phase difference between the LOS velocity and the apparent wave position suggests that the flare loops (and the fluid elements of plasma along them) are undergoing motion that is alternately parallel and perpendicular to the LOS. One example of a class of waves which produces such motion are surface waves, such as occurs in deep water driven by wind. In a surface wave, traveling in a direction x perpendicular to the surface normal z with no mean flow, the displacement of a fluid element $\delta\mathbf{x}$ is given by

$$\delta\mathbf{x}\left(x,z,t\right) = A\mathrm{e}^{kz}\left[-\sin\left(kx-\omega t\right)\hat{\mathbf{e}}_{\mathbf{x}} + \cos\left(kx-\omega t\right)\hat{\mathbf{e}}_{\mathbf{z}}\right]; \tag{3.1}$$

and the the velocity $\mathbf{v}$ is given by

$$\mathbf{v}\left(x,z,t\right)=A\omega\mathrm{e}^{kz}\left[\cos\left(kx-\omega t\right)\hat{\mathbf{e}}_{\mathbf{x}}+\sin\left(kx-\omega t\right)\hat{\mathbf{e}}_{\mathbf{z}}\right], \tag{3.2}$$

where A is the wave amplitude, ω is the wave frequency, k is the wave number, and $\hat{\mathbf{e}}_{\mathbf{j}}$ is the j^{th} unit vector (Phillips, 1977). As can be seen from these equations, a fluid element in this wave will trace out an ellipse in (x,z) as the wave passes, with a 90° phase difference between the two velocity components and a total 180° phase difference between a given velocity component and the position component perpendicular to it.

We also recall that the symmetry between the two ribbons suggests a coronal source to the wave. It therefore seems likely that an instability in the current sheet during reconnection is driving the sawtooth. Two such instabilities which have been shown to occur in coronal current sheets during reconnection, and which can lead to oscillations in the subsequent flare loops, are the *Kelvin-Helmholtz* (KH) instability (Uchimoto et al., 1991; Ofman & Thompson, 2011; Foullon et al., 2011) and the *tearing-mode* (TM) instability (Furth et al., 1963). Like the water wave described above, both of these plasma instabilities are confined to a surface (the current sheet) and produce elliptical motions. In the upper panel of Figure 3.12, we present a schematic conception of the scenario by which these instabilities could produce the observed features. Looking north along the flare arcade, the LOS comes roughly from the upper left. The two outermost black lines represent a pair of reconnecting field

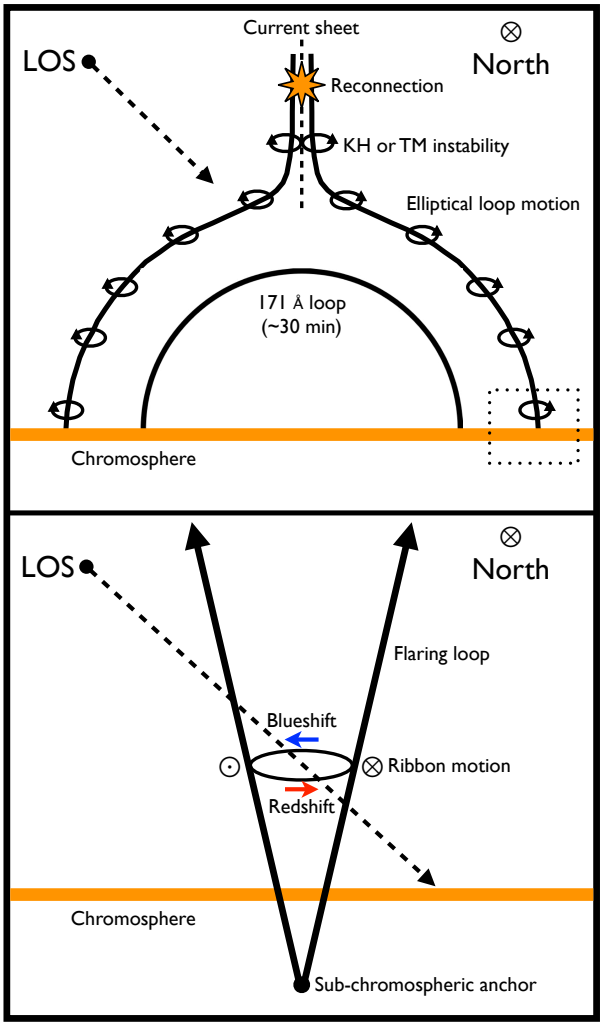


Figure 3.12. Upper panel: schematic diagram of our proposed scenario, with a KH or TM instability in the coronal current sheet resulting in elliptical wave oscillations in the reconnected flare loops. Lower panel: schematic diagram of the flare loop footpoint, as described in Section 3.4, showing how the elliptical wave motion relative to the LOS generates the observed 180° phase difference between the ribbon motion and Doppler velocities.

lines, where the reconnection is occurring at the star along the current sheet (vertical dashed line). We then hypothesize that either a KH or TM instability occurs, which results in elliptical motion of the field lines during their reconnection (indicated by the arrowed circles). The oscillation frequency is low enough that the loop responds rigidly, as a whole, pivoting at some depth below the chromosphere. Finally, the inner black circle shows a previously reconnected loop that has contracted and then cooled to become visible in 171 Å. By this point the loop is disconnected from the current sheet and oscillation has ceased. The instability drives the elliptical oscillation, but also appears to have a phase velocity within the sheet, producing the pattern motion at $v_{st} \simeq 15$ km s^{-1}.

Meanwhile, at the loop footpoint we see the effects of the instability-driven oscillations on the ribbon. The dotted box in the upper panel of Figure 3.12 indicates the zoom-in region, which is shown in the lower panel of Figure 3.12. Here, the oscillating loop is shown in two positions as the solid arrowed lines, with the LOS again from upper left as indicated. The loop is shown anchored somewhere deeper in the atmosphere, and the elliptical loop oscillation is indicated by the ellipse at the center and by the $\otimes$ and $\odot$ respectively representing motion into and out of the page. The observed amplitude of the oscillation will be the diameter of the ellipse; from above we find this to be $\sim$1–3″ or $\sim$0.7–2.2 Mm. We note that the only motion of the loop that results in Doppler shifts is that of the loop moving along the LOS, as indicated

by the blue and red arrows, and that the loop motion at the $\otimes$ and $\odot$ is perpendicular to the LOS and generates no Doppler shifts. Therefore, as we observe, the blue and red Doppler shifts will occur at the northern and southern extremes of the oscillation, as in Figure 3.8, and that the phase difference between the apparent position and Doppler shift will be 180°.

Obviously, in order to produce the observed Doppler shifts in C_B of $\pm$20 km s^{-1}, the loop must be rotating around the circle indicated in Figure 3.12 at approximately that same speed (technically it would need to be somewhat faster, due to the inclined LOS). Given that the observed amplitude of the oscillation (equivalent to the diameter of the circle) is $\sim$0.7–2.2 Mm, we note that a rotation speed of $\sim$30 km s^{-1} (allowing for LOS effects) would give an oscillation period of 70–230 s. This is very similar to the observed range for the period of the sawtooth oscillation, which varied between 80–190 s.

Finally, we believe that the two components C_R and C_B occur in distinct sets of loop footpoints, which are too closely spaced to be resolved by IRIS. Both sets of loops are participating in the elliptical oscillation generated by the instability described above. However, the greater non-thermal broadening of C_R, as well as the nonzero average redshifts, suggests that those footpoints are undergoing chromospheric condensation, presumably as that plasma is being directly energized by reconnection in

the instability region. The C_B component, on the other hand, has non-thermal broadening consistent with previous quiescent AR observations (De Pontieu et al., 2015), and displays an approximately zero average Doppler shift during the oscillation. This suggests that this set of footpoints have not been energized into condensation by coronal reconnection, even though those loops are still being elliptically oscillated by the instability. We recall, however, that the C_B component is still significantly brightened during the oscillation; it is possible that this plasma is being energized into enhanced emission via energy transfer from the loop waves (Russell & Fletcher, 2013).

3.5. Discussion

In this paper, we have presented an analysis of a two-ribbon flare using IRIS and AIA imaging and spectral observations. We found, along with the usual ribbon spreading at ∼1–2 km s^{-1}, that the ribbons show a distinct sawtooth substructure with a scale of 1–2 Mm. The sawtooth appears in both ribbons, maintains its shape coherently over time, and drifts along the ribbon from east to west at a speed of $v_{st} \simeq 15$ km s^{-1}. The period of this sawtooth oscillation was found to average ∼140 s, and the oscillation speed is ∼20 km s^{-1}. We also found that the sawtooth substructure appears in a variety of spectral lines, including Si IV, O IV, and C II, with nearly identical amplitude and phase across a wide range of temperatures. We

observed that the line profiles for Si IV and C II in and around the sawtooth have two major components (previously noted by Cheng et al. (2015)), and we developed an automated routine for fitting the two Si IV lines observed by the IRIS SG. O IV does not clearly show two components, but we noted that this may be due to the weaker intensity or different formation mechanism of the forbidden O IV lines. We showed that the two components of Si IV tend to persist over time and we identified the two components by their relative Doppler shifts, with the redder component labeled C_R and the bluer component C_B.

We found that C_R was redshifted by an average $\sim$50 km s^{-1} during the sawtooth, whereas C_B switched between redshifts and blueshifts. Further, we noted that the Doppler shifts for both components oscillate during the sawtooth with an amplitude of $\pm$20 km s^{-1} (averaging $\sim$50 km s^{-1} for C_R and $\sim$0 km s^{-1} for C_B) and a period of 100–200 s. This Doppler oscillation was found to be correlated with the spatial sawtooth oscillation, and the phase between these was found to be 180°. We also used the flare loops, identified in SDO/AIA 171 Å, to find the approximate conjugate point in the ER. Using an artificial slit constructed from the IRIS SJI 1400 Å and SDO/AIA 1600 Å data, we were able to identify two bands with the same amplitude, period, and phase as the WR sawtooth substructure. We believe this conjugacy of the sawtooth oscillation (along with the continuous and coherent evolution of the

sawtooth) strongly suggests that the sawtooth is *not* the result of the energy transport mechanism, such as an intensity-modulated non-thermal particle beams, but is rather due to physical transverse motion of the loop. We also conclude that the two conjugate ribbon oscillations are being driven by a common coronal source. We use 180° phase difference between the Doppler shift and sawtooth position, as well as the LOS inclination of the magnetic field, to eliminate two simple wave modes as the source for the sawtooth. Finally, we propose an elliptical oscillation motion of the loop, driven by an instability in the coronal current sheet, as the mechanism behind the observed sawtooth ribbon substructure.

The scenario depicted in Figure 3.12 is reminiscent of the kinds of loop oscillations sometimes observed in flares (Aschwanden et al., 1999). Oscillation of loops in 171 Å have previously been observed in association with KH instabilities (Ofman & Thompson, 2011). We failed to observe any oscillations in the AIA 171 Å image sequence which includes Figure 3.3, but this may be due to the ∼30 min delay between the loop formation, by reconnection, and its appearance at that cool wavelength.

Oscillations triggered by flares are interpreted as standing MHD waves, and can have periods in the ∼200 s range, consistent with the Alfvén transit time in the long, high, weak loops which are often found to oscillate. This interpretation is more problematic for our case with short, low, strong loops. The loops, visible in 171 Å (see Figure 3.3) appear to fit field lines of a constant-alpha field with $\alpha \simeq -5 \times 10^{-9}\,\mathrm{m}^{-1}$,

extrapolated form the line-of-sight HMI magnetogram. These field lines range in length from $L = 40$ to 60 Mm, and have field strengths falling to $B \sim 150$ G at their apices, around $z \sim 10$ Mm. For a typical density of $n_e \simeq 10^9\,\mathrm{cm}$, the coronal Alfvén speed would be no smaller than 10 Mm s^{-1}, for which the end-to-end transit times would be 4–6 seconds on these loops. The 140 s sawtooth evident at the ribbon could not, therefore, correspond to a standing wave in loops like those formed after the flare.

We believe a more likely scenario to be that the short, strong field lines are moving quasi-statically (far slower than the Alfvén speed) in response to motion imposed by an elliptical wave occurring at or near the current sheet. This could be the hydrodynamic motion of a KH instability driven by velocity shear across the current sheet (Ofman & Thompson, 2011). For this to be the case, however, the magnetic field would have to be very nearly anti-parallel across the sheet, in order that a guide-field component not stabilize the instability. If the pattern speed, $v_{st} \sim 15$ km/s were related to this component of the Alfvén speed the angle between the fields would have to be within one milliradian (0.006°) of perfectly anti-parallel. A more likely explanation is the tearing mode (TM), which is expected to occur at current sheets, and also exhibits elliptical flow patterns (i.e. the velocity stream function consists of islands). The observed ribbon motion would be related to the inflows and outflows from the X-lines, estimated to be smaller than the Alfvén speed by a factor, $S^{-1/2}$,

where $S \gg 1$ is the Lundquist number of the current sheet. Flow speeds of ~ 20 km/sec would arise from a Lundquist number, $S \sim 10^6$, but this may reflect the turbulent state of the sheet itself. Finally, this instability would need to propagate at a speed lower than Alfvén speed, but comparable to the flow speeds of the instability. However, we have no insights as to what might give the instability the precise phase velocity that we observe.

Another point concerning the proposed scenario in Figure 3.12 which we left unspecified is the location of the loop anchor. Presumably, this anchor point is located deep enough in the atmosphere to allow for the observed sawtooth amplitude. We might expect that the Si IV, O IV, and C II spectral lines , which are normally formed at different heights within the chromosphere and TR and would thus exhibit different amplitudes of the loop motion, providing us with some information about the anchor location. However, as we noted, these lines instead all display identical amplitudes of the sawtooth pattern. We speculate that this is due to the TR being compressed during the flare, such that the normally separated spectral line formation heights are all approximately the same within the ribbon, which eliminates any information about the location of the loop anchor.

We also note that the small mean Doppler shift of C_B indicate that the plasma generating that component of the Si IV emission is not probably undergoing intense

evaporation during the sawtooth. Further, the non-thermal widths for C_B are consistent with those for quiescent AR plasma (De Pontieu et al., 2015). On the other hand, both components of Si IV show strong increases in intensity during the sawtooth, indicating the the plasma has been energized into enhanced emission. We do not know what is causing this brightening of non-evaporating plasma within the context of our proposed scenario, although we have speculated above that wave motion may contribute to the plasma energization.

In their recent work, Li & Zhang (2015) report an observation of ribbon substructure in a different flare (2014 September 10, X1.6-class) that is in some ways very similar to our observations of the 2014 April 18 flare. In particular, they observed a quasi-periodic slipping motion, which manifested as a series of bright knots which appear to move along the ribbon at $\sim$ 20 km s^{-1}, close to our own estimate of v_{st}. Their interpretation of this slipping motion was as an apparent motion, of the kind discussed by Aulanier et al. (2006) and dubbed "slipping reconnection". Unlike our scenario for the 2014 April 18 event, however, they speculate that this slipping reconnection may be the result of density variations in the reconnection region, which are driven by p-mode oscillations above the sunspot. Also in marked contrast to our observations, Li & Zhang (2015) report a relatively steady Si IV redshift, unmodulated by the sawtooth pattern. This is consistent with their interpretation of a pattern projected from the current sheet onto the chromosphere along stationary magnetic

field lines: i.e. slipping reconnection. Our observations, however, reveal clear motion of the plasma, through the Doppler shifts which are correlated with the sawtooth pattern. This rules out the hypothesis that the oscillations are merely projections and, at least in our flare, it rules out slipping reconnection.

It is possible that the discrepancies between these two observations arise purely from the different viewing angles of the different cases. The 2014 September 10 flare occurred very close to disk center, so if there were horizontal plasma motions, tracking the elliptical loop oscillations, they would not give rise to line-of-sight Doppler shifts. Our own case, the 2014 April 18 flare, occurred 40 degrees from disk center, where horizontal motions would, and apparently do, produce line-of-sight Doppler shifts.

The apparently contradictory observations presented in this paper and in Li & Zhang (2015) indicate that additional observations of flare ribbons, located at varying locations and viewing angles, will be necessary to differentiate between the two hypothesis: apparent motion due to slipping reconnection *vs* elliptical loop oscillations driven by KH or TM instabilities. Of course, it has only been recently that instruments with sufficient spatial and temporal resolution have allowed for observations of ribbon substructure. As we have noted, lower resolution and cadence imagers such as SDO/AIA only barely allow for recognizing ribbon substructure at scales less than $1''$, and also do not provide the Doppler information that allows for determining phase relationships of chromospheric phenomena. The authors expect that as future IRIS

observations develop, particularly in conjunction with a coronal spectrograph such as *Hinode*/EIS, we will be able to distinguish between various hypothesis for generating ribbon substructure, and use observations of ribbons to eliminate or support models for reconnection in the corona.

3.6. Acknowledgements

IRIS is a NASA small explorer mission developed and operated by LMSAL with mission operations executed at NASA Ames Research center and major contributions to downlink communications funded by the Norwegian Space Center (NSC, Norway) through an ESA PRODEX contract. The authors would like to thank the anonymous referee who provided suggestions for significant improvement of the original manuscript. The authors would also like to thank Prof. Charles Kankelborg, Dr. Sarah Jaeggli, Dr. Ying Li, Dr. Paola Testa, and Dr. Bart De Pontieu for helpful and productive discussions concerning the IRIS instruments and data analysis. This work was supported by contract 8100002702 from Lockheed Martin to Montana State University, a Montana Space Grant Consortium graduate student fellowship, and by NASA through HSR.

4. OBSERVATIONS OF PSEUDO-BALLISTIC DOWNFLOWS IN A M-CLASS FLARE WITH THE INTERFACE REGION IMAGING SPECTROGRAPH

Contribution of Authors and Co–Authors

Manuscript in Chapter 4

Author: Sean R. Brannon

Contributions: Conceived and implemented study design. Constructed code to analyze data sets. Wrote complete drafting of the manuscript.

Manuscript Information Page

Sean R. Brannon
The Astrophysical Journal
Status of Manuscript:
_x_Prepared for submission to a peer–reviewed journal
____Officially submitted to a peer–reviewed journal
____Accepted by a peer–reviewed journal
____Published in a peer–reviewed journal

To be submitted January, 2016

ABSTRACT

The standard picture of flare loop evolution includes chromospheric evaporation, plasma cooling, and subsequent draining downflows. Despite significant advances in instrumentation, there is as yet no study analyzing spectral observations of on-disk flare loops covering this entire process. Further, no study exists which uses spectral observations of the draining downflows for an entire loop to constrain properties of the plasma velocity profile via synthetic spectra. Without such investigations, it is impossible to fully assess the validity of the standard models of flare loops and flows. In this paper we present an imaging and spectroscopic observation from the Interface Region Imaging Spectrograph (IRIS) of the SOL2015–03–12T11:50:00 M-class flare, at high spatial resolution and time cadence. Our analysis of the Fe XXI 1354.067 Å and Si IV 1402.772 Å spectral data reveals the three-phase process of evaporation and loop filling with plasma at flare temperatures followed by cooling and loop draining in chromospheric lines, manifesting as "C"-shaped redshifts in the Si IV spectra, as well as the loop plasma densities and non-thermal broadening (NTB) of the Si IV line. We use these observations to generally validate the standard picture of flare loop evolution, and use synthetic spectra to constrain a simple free-fall model of the loop downflows.

4.1. Introduction

Solar flares are among the most energetic explosive events that occur within the Solar System, and have a profound impact on the local space environment within which the Earth resides. The standard picture of the evolution of a solar flare begins with the reconnection of magnetic field lines in the corona (Carmichael, 1964; Sturrock, 1966; Hirayama, 1974; Kopp & Pneumann, 1976), forming a series of flare loops. Once reconnected, the loops are then free to retract at the Alfvén speed, compressing and heating the plasma to several tens of MK near the loop tops (Semenov et al., 1998; Longcope et al., 2009). The energy released during this process is generally thought

to be transported down the flux tube from the reconnection site by some combination of non-thermal electron beams (Brown, 1973) and thermal conduction (Craig & McClymont, 1976; Forbes et al., 1989). Whatever the mechanism, once the energy reaches the transition region (TR) and chromosphere at the flare loop footpoints it becomes deposited in the cool dense plasma located there, heating it and resulting in an over-pressure which drives upflows known as *chromospheric evaporation* (Sturrock, 1973). The evaporated chromosphere plasma, which is now at flare temperatures, fills the loop from one or both foot points and results in the loop appearing bright in hot coronal spectral lines.

Once the evaporation process has ceased and the flare loop has been filled with hot plasma, it begins to cool through a combination of radiative and conductive energy transfer (Antiochos & Sturrock, 1978; Antiochos, 1980; Culhane et al., 1994; Cargill et al., 1995). In the case of conduction the magnetic field constrains the energy transport to be along the loops, moving thermal energy down towards the cooler layers in the chromosphere. The radiative losses, meanwhile, are responsible for the observational appearance of the loop in various wavelengths. Models differ on which of these mechanisms dominate the energy loss process: for example, Antiochos (1980) finds support for radiatively-dominated cooling, while Antiochos & Sturrock (1978) finds support for conduction-dominated cooling, and Cargill et al. (1995) finds support for an early conduction phase followed by a later radiative phase. In addition

to these two mechanisms, Bradshaw & Cargill (2010) show that, in the presence of bulk plasma flows, the loop can also lose thermal energy through an enthalpy flux. Whatever the mechanism, the result is that the plasma cools, loses its pressure support in the loop, and begins flowing back down towards the footpoints.

The downflowing plasma in coronal loops is often referred to as *coronal rain* (Foukal, 1978, 1987). Coronal rain has been observed most frequently in Hα (e.g. Brueckner (1981)), but has also been observed in coronal and chromospheric lines using TRACE (Schrijver, 2001a; Winebarger et al., 2001, 2002), SoHO/SUMER (Winebarger et al., 2002), and SoHO/CDS (Brekke et al., 1997a). Brekke et al. (1997a) reports flows of $\sim$60 km s^{-1} along one leg of a loop, indicating possible catastrophic cooling (Cargill & Priest, 1982) on one side. Off-limb observations in Hα and other wavelengths have also reported a wide variety of downflow velocities for coronal rain. Schrijver (2001a) reports velocities in transition region temperatures of $\sim$100 km s^{-1} and a downward acceleration of $\sim$80 km s^{-2}, around 1/3 of the free-fall acceleration under solar surface gravity. Observations of off-limb prominences have also revealed that ballistic (free-fall) plasma flows often occur near the loop apexes but that the plasma experiences reduced accelerations near the footpoints (Wiik et al., 1996; Malherbe et al., 1997; Liang et al., 2004).

Most of the studies discussed above suffer from similar observational limitations. First, with the exception of Brekke et al. (1997a), these studies all depend on feature-tracking methods using imaging observations. These methods require there to be distinguishable density features in the plasma which can be tracked over time; thus, they cannot track steady flows with smooth density gradients, and it is generally impossible to determine whether a bright stationary structure is due to a static piece of plasma or to density compression due to flows or shocks. In Brekke et al. (1997a), the authors attempt to circumvent this issue by using spectroscopic observations from SoHO/CDS. As they report, however, the off-limb nature of the prominence makes it impossible to determine whether the flows are upflows or downflows. Finally, the majority of studies involve observations of off-limb prominences which persist for hours or even days, and thus the flows described are not relevant to actively flaring loops.

Ideally, the loops involved would be located near disk-center and oriented normal to the solar surface, to avoid ambiguities in flow direction, and would either be currently undergoing, or have recently undergone, flaring activity. Unfortunately, such direct spectroscopic observations of flare loop flows are difficult to obtain: the instrument must be pointed directly at the loops as they flare, and limitations in cadence and spatial resolution means the loop flows may not be adequately resolved.

Studies of cooling plasma in on-disk flare loops that were filled during a flare evaporation event are therefore scarce, despite the importance of direct observations of post-cooling loop flows. One notable example is found in Czaykowska et al. (1999), which reports chromospheric evaporation in flare ribbons in the form of blueshifted Fe XVI and O V lines from a SoHO/CDS observation. In Figure 1 of that paper, redshifted O V lines can be noted in the loop arcade in those results. The authors primarily focused on the redshift-to-blueshift gradient across the ribbon boundary, however, and did not address the source of the arcade flows or attempt to fit a model loop velocity profile to the observed data. To the best of our knowledge, therefore, no previous studies have reported on the full spectral evolution of on-disk flare loops from evaporation to draining. As a result, there exists no complete observational confirmation of our theoretical model of loop filling and draining.

Launched on 23 June 2013, the Interface Region Imaging Spectrograph (IRIS) has high-resolution and high-cadence imaging and spectroscopic instruments, recording several diagnostic lines spanning a wide range of chromospheric, transition region, and coronal temperatures. IRIS therefore is an ideal instrument for taking observations of flare loop flows during the evaporation, cooling, and subsequent draining phases of a flare. In this paper we analyze an IRIS observation of a near-disk center flare and the associated flare loops, and use the results to determine the velocity profile of the cooling plasma. The outline of the paper is as follows: in Section 4.2 we describe the

IRIS instrumentation; in Section 4.3 we give the details of the active region and the particular flare of our interest; in Section 4.4 we delve into the imaging and spectral data of the flare evolution, calculate Doppler shifts and line widths, and analyze the plasma density and cooling time; in Section 4.5 we present a simple ballistic flow model and calculate synthetic IRIS spectra; finally, in Section 4.6, we will briefly discuss our results and open questions.

4.2. Instrument

IRIS is a NASA Small Explorer mission located in low-Earth orbit, and features two primary instruments: a dual-range UV spectrograph (SG) and a 4-band slit-jaw imager (SJI). The SG and the SJI have identical pixel size ($0''.16$). The SG slit is $0''.33$ wide (giving an effective spatial resolution of $0''.4$) and $175''$ long, and covers two FUV passbands (1332 Å to 1358 Å and 1389 Å to 1407 Å) and one NUV passband (2783 Å to 2835 Å). The passbands contain spectral lines formed over a wide range of temperatures, from photospheric (5000 K) to coronal (11 MK), however the primary mission focus is on chromospheric and transition region lines. The SG slit may be placed in a single location ("sit-and-stare") or it may be rastered to provide 2-D coverage. The SJI is used to provide context and coalignment imaging of the observation region. The SJI FOV is identical to the SG ($175'' \times 175''$), and records in four passbands (1335 Å, 1400 Å, 2796 Å, and 2832 Å). The SJI typically operates at a

reduced cadence (1/2 to 1/4) compared to the SG, due to cycling between passbands (De Pontieu et al., 2014).

The rest wavelengths of spectral lines for the IRIS SG are generally dynamically shifted to some degree due to the orbital motion and thermal variations of the IRIS spacecraft. The absolute wavelength calibration must therefore be individually corrected for each spectrograph exposure. To do this we use the SSWIDL (Freeland & Handy, 1998) routine `iris_orbitvar_corr_l2`, which fits the Ni I 2799.474 Å line to determine the appropriate wavelength shift for the FUV bandpass (De Pontieu et al., 2014; IRIS Technical Note 20). We then apply this correction to the wavelength axis for each exposure.

4.3. Flare Details

The data for this paper were taken from an IRIS observation on 12 March 2015 which began at 05:45:19 UT and ended at 17:40:59 UT. This observation was a large sit-and-stare flare watch, performed in conjunction with HOP 245 with the *Hinode* spacecraft. The observation cadence was ∼5 s for the SG and ∼15 s for each passband of the SJI (1330 Å, 1400 Å, and 2832 Å). The SJI FOV was (120″,119″) and was initially centered at (−235″,−190″). The target for this particular observation was NOAA AR 12297, which on that day was a large active region located somewhat south and east of disk center. In Figure 4.1 we display an SDO/HMI magnetogram

(standard color table) taken at 11:34:14 UT which shows the line-of-sight magnetic field of the region. The IRIS SJI FOV at this time is overlaid as the solid black context box, and the position of the SG slit is overlaid as the vertical black dashed line. AR 12297 rotated around the solar east limb on 6 March 2015, and at that time already possessed a complex magnetic geometry with several polarities and polarity inversion lines. During the IRIS observation on 12 March 2015 a strongly bipolar region centered at $(-170'',-170'')$ can be seen dominating the eastern side of the AR in Figure 4.1, with a negative polarity in the north and positive polarity in the south (an intrusion of positive polarity within the negative region can also be seen, which appeared and vanished several times during the preceding days).

Numerous flares occurred within AR 12297 during the week of 12 March 2015. Several of these flares occurred within the IRIS SJI FOV during the course of this observation, and the SG slit was well positioned over the polarity inversion line for the strong bipolar region mentioned above (see Figure 4.1). Some of these flares produced flare ribbons and/or loops which were crossed by the SG slit; these include a C4.3 at 08:15 UT (all times refer to GOES peak X-ray flux), a C8.4 at 09:14 UT, an M1.6 at 11:50 UT, and an M1.4 at 12:14 UT. The flare we have chosen to analyze in this paper was the M1.6, which initiated at 11:38 UT and continued until the initiation of the subsequent M1.4 flare at 12:09 UT. This flare produced two chromospheric ribbons, one on either side of the polarity inversion line, which were easily visible in SDO/AIA

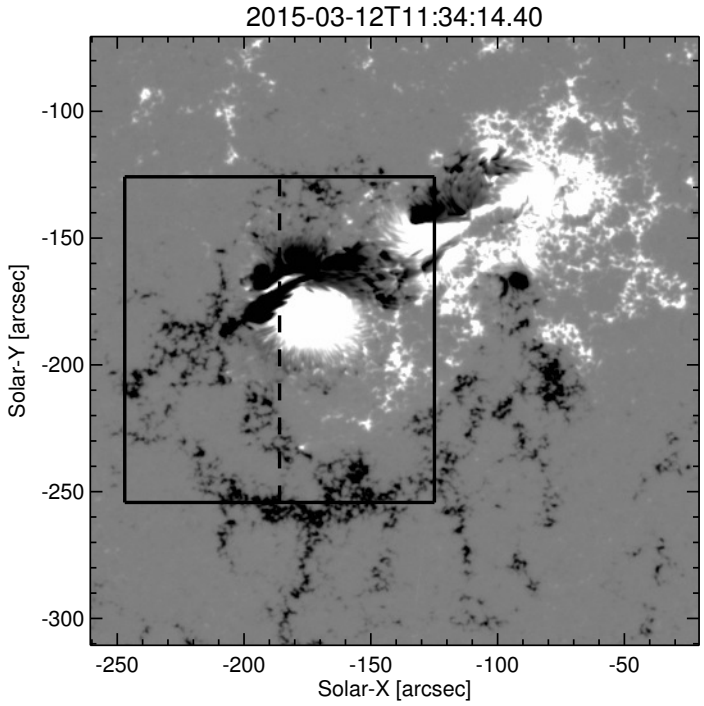


Figure 4.1. Image of the SDO/HMI magnetogram (normal color scale) for AR 12297, taken shortly before the flare start at 11:34:14 UT. The IRIS SJI FOV is indicated for context by the solid box, and the SG slit pointing is indicated by the vertical dashed line.

1600 Å. In Figure 4.2 we show a 1600 Å image taken at 12:02:40 UT which shows these northern and southern ribbons; note that we use a reversed $\log_{10}$ black-white (RLBW) color scale, where white is lowest and black is highest intensity.

We also note several tenuous strands of 1600 Å emission which appear to connect the two ribbons. The strands generally follow paths leading from northeast to southwest, and are much fainter than the ribbons. These strands appear to coincide with the paths of the flare loops, as can clearly be seen by inspecting the SDO/AIA 171 Å

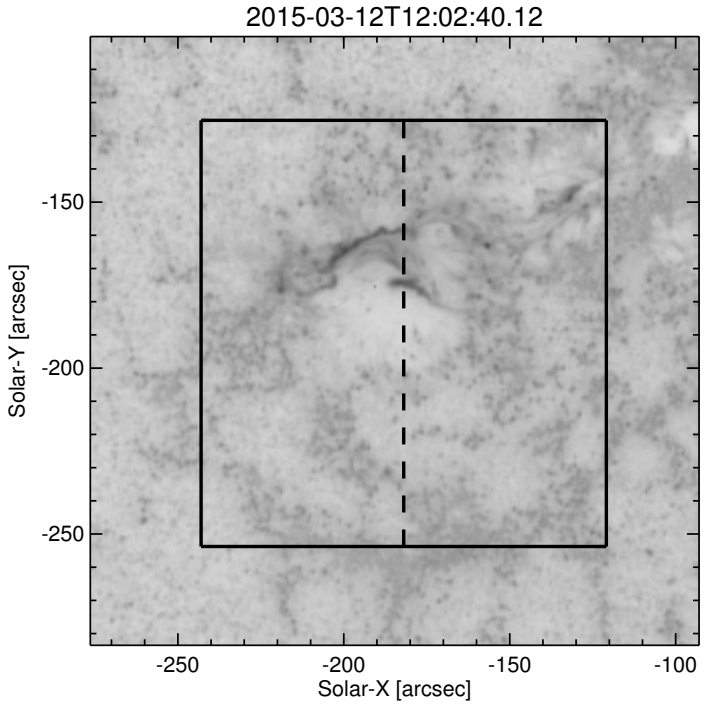


Figure 4.2. Image of the flare ribbons taken by SDO/AIA 1600 Å during the flare at 12:02:40 UT, in RLBW color scale (defined in Section 4.3). The IRIS SJI FOV is indicated for context by the solid box, and the SG slit pointing is indicated by the vertical dashed line.

image in Figure 4.3 (also RLBW). Note that the time for this image is 12:28:47 UT, which is ∼26 minutes later than the 1600 Å image. This is due to significant saturation of pixels in the 171 Å passband at earlier times, and also to the fact that cooling flare plasma typically appears in 171 Å later than the formation of the loop by the flare. We see, however, that the flare loops are clearly visible arcing from northeast to southwest between the northern and southern ribbons along very similar trajectories as the strands in 1600 Å. Combined with the fact that the strands appear in 1600 Å

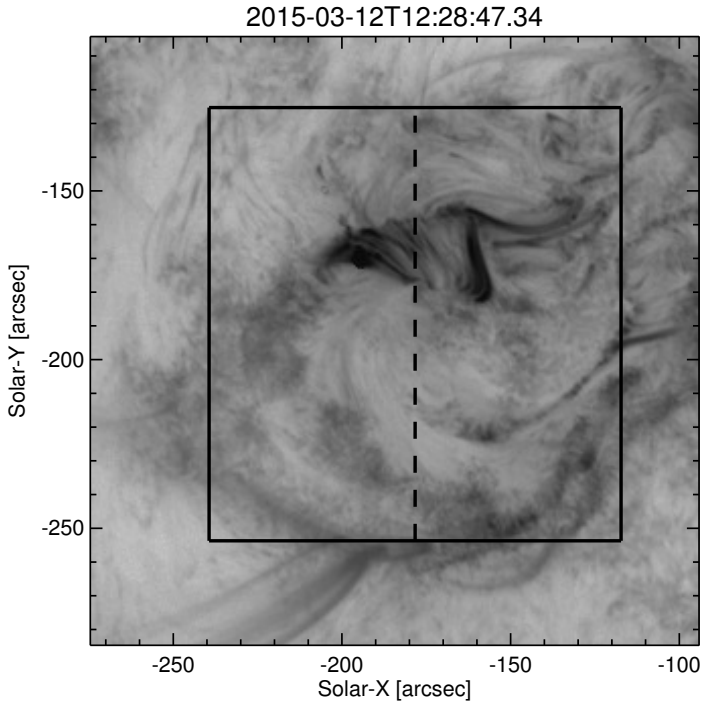


Figure 4.3. Image of the flare loop arcade taken ∼40 minutes after the flare peak by SDO/AIA 171 Å, in RLBW color scale. The IRIS SJI FOV is indicated for context by the solid box, and the SG slit pointing is indicated by the vertical dashed line.

only after the flare peak at 11:50 UT, this leads us to believe that the strands are in fact emission from the flare loops despite the chromospheric temperature $\log T = 4.7$ of the C IV lines which dominate the 1600 Å passband (Lemen et al., 2012).

The IRIS SJI observations of this flare confirm many of the same features noted above in the AIA images. In Figure 4.4 we show the full-FOV image for the IRIS SJI 1400 Å passband taken at 12:02:44 UT (approximately the same time as for Figure 4.2) in RLBW. In the image the SG slit can be seen as a pale line running vertically down the center at $-182''$. For context with the SDO images, note that in Figures

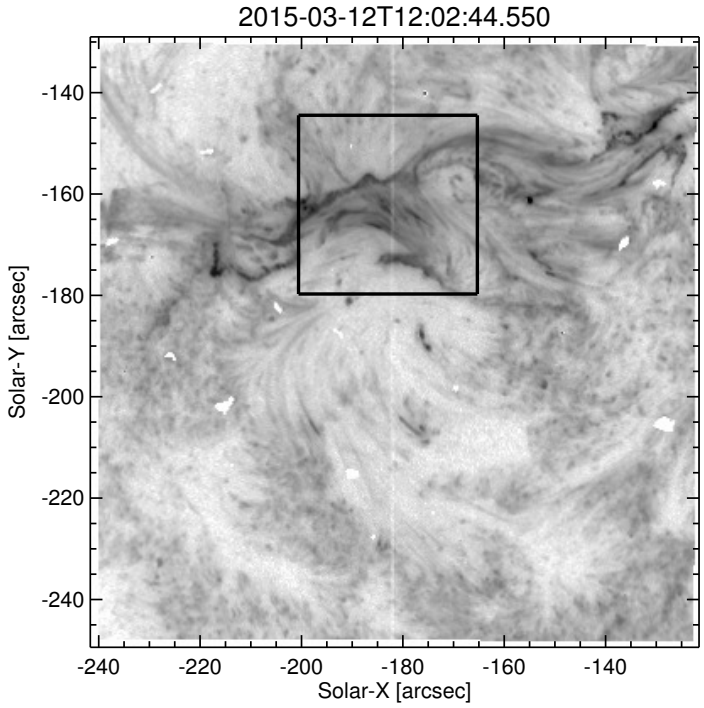


Figure 4.4. Full-FOV image from the IRIS SJI 1400 Å passband taken during the flare at 12:02:44 UT (approximately the same time as Figure 4.2), in RLBW color scale. The SG slit is visible as a pale line running vertically down the center of the image. The solid box indicates the zoom region in Figure 4.5.

4.1–4.3 we have indicated the IRIS SJI FOV by the solid black inset boxes and the SG slit position by the vertical black dashed lines. We note first that the fortuitous positioning of SG slit, perpendicular to the polarity inversion line, provides excellent coverage over both ribbons and loops for this flare. In Figure 4.4, we can see both the northern and southern flare ribbons running east-to-west and crossing the slit at approximately $y = -160''$ and $y = -175''$ respectively. Connecting the ribbons, we again see the flare loop strands, discussed above for the 1600 Å image, clearly

visible running from northeast to southwest in 1400 Å and crossing the SG slit at multiple positions between the two ribbons. We also note that the loop strands are significantly more distinct in this image than in Figure 4.2. This may be because the 1400 Å SJI passband is dominated by plasma at $\log T = 4.8$, and is thus slightly hotter than the AIA 1600 Å passband. We might thus expect that flare loops would be somewhat brighter and more distinguishable at the higher temperature.

4.4. Results

4.4.1. Flare Evolution

In order to further investigate the flare evolution, in Figure 4.5 we have plotted the SJI 1400 Å images (left column) for the inset box in Figure 4.4 taken at four representative times during the evolution of the flare (Row 1: 11:43:19 UT; Row 2: 11:50:09 UT; Row 3: 11:55:24 UT; and Row 4: 12:03:16 UT). The SG slit can again be seen as a pale vertical line in the center of each plot. We have also plotted the SG data along the slit (at the same times) for the O I 1355.598 Å (middle column) and Si IV 1402.772 Å (right column) passbands. The O I 1355.598 Å passband contains the Fe XXI 1354.067 Å spectral line at $\log T = 7.0$, and the Si IV 1402.772 Å passband is dominated by the Si IV 1402.772 Å spectral line at $\log T = 4.8$ but also contains the O IV 1399.780 Å and O IV 1401.157 Å spectral lines at $\log T = 5.2$. The x-axes for the spectral data are in km s^{-1}, calibrated to respectively place the Fe XXI 1354.067

Å and Si IV 1402.772 Å rest wavelength at 0 km s^{-1}, and the rest wavelength is indicated in each plot by the vertical dashed lines. All plots use the RLBW color table.

In the first row (11:43:19 UT), the flare is already several minutes in progress. We note a bright flare ribbon running roughly east to west and crossing the slit at $-160''$, and another ribbon located off the slit in the southwest corner of the image. As in the SDO/AIA 1600 Å image, various flare loops connecting the two ribbons can be already be observed, even though the SJI 1400 Å images primarily represent plasma at $\log T = 4.8$. Meanwhile, in the Fe XXI passband, we observe a bright horizontal line of emission, co-spatial with the northern ribbon position crossing the slit in the SJI at $-159''$, that stretches across the entire passband. This bright line is also visible in the Si IV passband, and is most likely an enhancement of the continuum due to energized plasma at the flare ribbon. We also note a brightening of the Si IV 1402.772 Å line at that same position which is strongly redshifted, most likely due to chromospheric condensation. Other regions of intermittent Si IV 1402.772 Å emission, mostly redshifted, are visible between $-160''$ and $-170''$, one of which (around $-168''$) also shows O IV 1399.780 Å and O IV 1401.157 Å emission. Finally, we note a distinct "comma" shaped patch of Fe XXI 1354.067 Å emission, located between $-160''$ and $-166''$, with strong (100–200 km s^{-1}) blueshift in the north transitioning to stationary farther south.

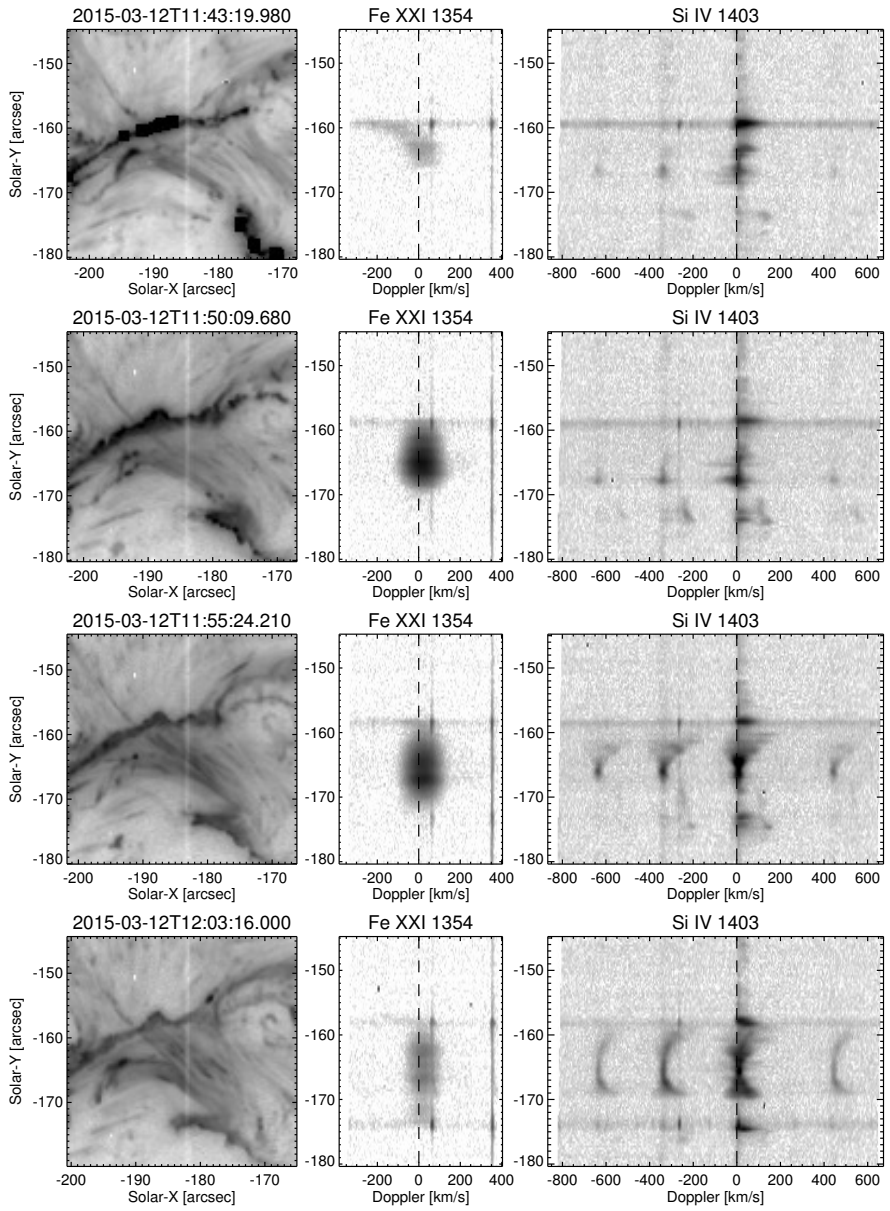


Figure 4.5. A time series of IRIS SJI and SG images, in RLBW color table, for four different times (by row: 11:43:19 UT, 11:50:09 UT, 11:55:24 UT, 12:03:16 UT) showing the imaging and spectral evolution during the flare described in Section 4.4.1. The SJI 1400 Å images (left column) correspond to the solid inset box in Figure 4.4. The two SG passbands shown are O I 1355.598 Å (middle column), which contains the Fe XXI 1354.067 Å spectral line, and Si IV 1402.772 Å (right column), which also contains the O IV 1399.780 Å and O IV 1401.157 Å spectral lines. The x-axes for the spectral plots are in km s^{-1}, calibrated to respectively place the Fe XXI 1354.067 Å and Si IV 1402.772 Å rest wavelength at 0 km s^{-1}. The rest wavelength is indicated in each plot by the vertical dashed lines.

In the second row (11:50:09 UT), we note many of the same features persisting from Row 1. The loops are visible at similar intensities and have much the same paths from northeast to southwest as before. The southern ribbon remains mostly off the slit in the southwest, although it has extended somewhat towards the northeast, and the redshifted emission in the Si IV 1402.772 Å line at $-173''$ suggests it may be beginning to cross the SG slit. The continuum enhancement from the northern ribbon also persists in both SG passbands, and it continues to do so for the remainder of the rows. The Si IV and O IV features south of the ribbon are still present but have intensified. The most notable change, however, is in the Fe XXI 1354.067 Å line, which has lost the strong blueshifts in the north, extended farther south, and intensified to become a wide (>100 km s^{-1} half-width) region of bright flare plasma emission.

In the third row (11:55:24 UT), several important changes have occurred in both the SJI and the SG over the intervening 5 minutes. First, the northern ribbon has significantly lower intensity than in the previous row, although it maintains a very similar shape. The southern ribbon, meanwhile, has continued to extend to the northeast, and has begun to clearly cut across the SG slit, and we see a notable enhancement in the redshifted Si IV 1402.772 Å emission at the same position of $-173''$ as before. The flare loops in the SJI have still not significantly altered their shapes, but they have become brighter than before, and thus are more distinct. The

Fe XXI 1354.067 Å emission remains stationary or slightly redshifted, but has faded somewhat over the 5 minute timespan. The most significant change, however, is in the Si IV and O IV lines located between $-160''$ and $-170''$. These lines have all brightened, quite significantly in the case of the Si IV 1402.772 Å line, and have adopted a distinct quarter-circle shape with fainter redshifts in the north ($-162''$) and bright stationary plasma farther south ($-165''$).

In the final row (12:03:16 UT), we see that the southern ribbon has finally cut all the way across the SG slit, resulting in a horizontal line of continuum enhancement at $-174''$ similar to the one in the north. Both ribbons have continued to fade in intensity, and the connecting loops have now begun to fade somewhat as well. The Fe XXI 1354.067 Å emission has faded significantly since the previous image, enough so that the O I 1355.598 Å line is now visible running north–south. However, the Si IV 1402.772 Å, O IV 1399.780 Å, and O IV 1401.157 Å lines between $-160''$ and $-170''$ have continued to evolve into distinct "C" shaped arcs with bright stationary emission near the center at $-165''$ and fainter (but still bright) redshifted (40-50 km s^{-1}) regions to the north and south. Although we do not show the SG images for other times in this paper, we observe that this "C" shape in these three spectral lines persists for up to 20 minutes starting at ∼11:56 UT and continuing, albeit at fading intensity, until ∼12:16 UT.

4.4.2. Spectral Intensity Evolution

There are two IRIS SG passbands which are of interest for this paper. One is the O I 1355.598 Å FUV passband, which contains the Fe XXI 1354.067 Å spectral line formed at $\log T = 7.0$. The other is the Si IV 1402.772 Å FUV passband, which is dominated by the Si IV 1402.772 Å spectral line formed at $\log T = 4.8$ but also contains the O IV 1399.780 Å and O IV 1401.157 Å spectral lines formed at $\log T = 5.2$ (De Pontieu et al., 2014). In Figure 4.6 we have plotted time-distance stack plots of the total intensity for these two passbands during the flare, with O I 1355.598 Å appearing in the upper plot and Si IV 1402.772 Å in the lower plot. The x-axis is time (in UT) which runs between 11:36 UT and 12:36 UT, and the y-axis is Solar-Y (in arcsec) along the SG slit which runs between $-155''$ and $-180''$. The color table for both plots is RLBW, and the color scale is shown to the right of each plot.

Several features are readily apparent in these two stack plots. First we note two bright, roughly horizontal, bands located in both plots at $\sim -159''$ and $\sim -175''$. These correspond to the northern and southern ribbons respectively, which is confirmed by inspection of the ribbon locations from Figure 4.5. The northern ribbon emission brightens abruptly at ∼11:42 UT, however the southern ribbon does not significantly brighten in the SG until ∼12 minutes later (although fainter emission can be seen back to 11:42 UT as well); this is true for both passbands. The delay is explained by recalling from Figure 4.5 that the southern ribbon does not begin to cut across the

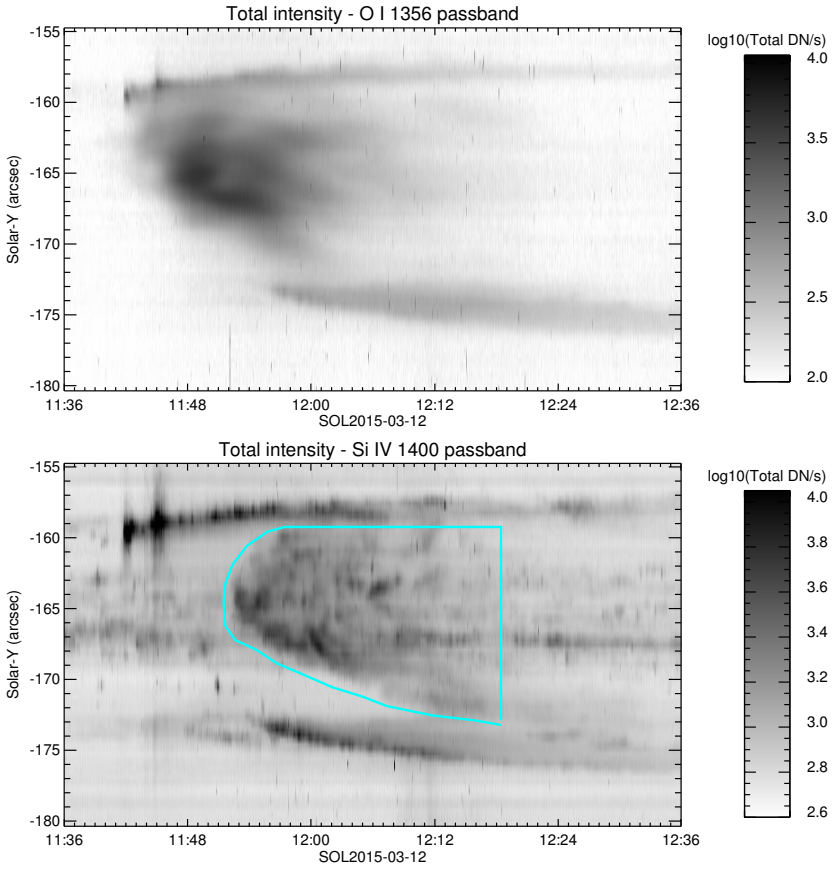


Figure 4.6. Time-distance stack plots showing the intensity evolution for the O I 1355.598 Å (upper plot) and Si IV 1402.772 Å (lower plot) SG passbands. The x-axis for each plot is in UT, and the intensity color table is shown at right of each plot. Note the cyan contour, which is described in Section 4.4.2 and which we refer to as the "bullet".

SG slit until after 11:50 UT. We additionally note that the emission for both ribbons appears to fluctuate in intensity during the flare (this is more apparent in the Si IV 1402.772 Å passband), which may be related to similar observations of footpoint ribbon emission in other papers (Brannon et al., 2015; Brosius & Daw, 2015).

Between the two ribbons in both plots is a large diffuse region of emission, located between $-160''$ and $-173''$, which corresponds to the flaring loops seen in Figures 4.3 and 4.5. This loop emission appears first in the hotter Fe XXI line between $-160''$ and $-165''$, shortly after the northern ribbon brightens at 11:42 UT. Subsequently, the Fe XXI emission moves southward and expands to fill most of the region between the ribbons. We note two particularly intense loop emission events, occurring at $-163''$ and $-168''$ respectively, during the time interval between 11:48 UT and 11:54 UT, with the more northern one occurring first and followed shortly thereafter by the southern brightening. After $\sim$11:57 UT, we observe that the Fe XXI emission in the loops begins to fade (although significant emission remains in the parts of the loops until after 12:06 UT).

The loop emission in the Si IV 1402.772 Å passband follows a similar pattern of evolution to Fe XXI, albeit shifted forward somewhat in time. From Figure 4.6, we see that the Si IV emission appears first at $-165''$ and 11:53 UT ($\sim$ 11 minutes after the Fe XXI first appears) before expanding north and south to fill the inter-ribbon

region. We observe particularly intense emission events at $-165''$ and $-168''$, co-spatial with the Fe XXI emission events mentioned above and of similar durations but $\sim$6 minutes later. Finally, we note that the Si IV emission begins to fade after $\sim$12:12 UT, although a distinct band of emission remains between $-167''$ and $-168''$ until well after 12:36 UT.

To aid in our subsequent analysis of the flare loops, we have identified the Si IV emission which we believe to be associated with the loops by the cyan contour in Figure 4.6. The contour begins with the appearance of significant Si IV emission at 11:52 UT near $-165''$, and then extends north and south eventually encompassing all SG pixels between $-160''$ and $-173''$. Note that we have deliberately excluded the ribbon emission at the footpoints to the north and south, since the emission there is likely complicated by the more complex chromospheric footpoint geometry. We end the contour arbitrarily at around 12:19 UT, by which point the majority of the Si IV emission has faded. Due to its shape we shall henceforth refer to this contour as the "bullet", and we will refer to all points (in space and time) as "pixels".

4.4.3. Doppler Velocities and Line Widths

The SG images for the Si IV 1402.772 Å passband, shown in Figure 4.5 and discussed above, reveal a variety of different behaviors for the spectral lines in that passband, which vary in both space and time during the flare. For a more detailed look at the spectral data, we have selected the Si IV 1402.772 Å spectral profiles for

nine different pixels located within the bullet and plotted them in Figure 4.7. A copy of the Si IV intensity stack plot and bullet contour is provided at the top of Figure 4.7 for context, and the spectral data for each pixel is plotted below. The nine pixels we selected are indicated in the context map by the "+" symbols, and we have labeled these "1"–"9" corresponding to the labels at the top of each spectral plot. The x-axes for all plots are in km s^{-1} calibrated to the reference wavelength of Si IV 1402.772 Å (indicated by the vertical dotted line at $v = 0$), and the y-axes are in DN s^{-1}. Finally, we note that the times for pixels 2–3, for pixels 4–6, and for pixels 7–9 are identical within each of those three sets.

We note first many of the same features we have already discussed above. Early in the bullet, the Si IV line is nearly stationary, with very slight redshifts of $<$10 km s^{-1}. A few minutes later, positions away from the bullet center begin to indicate redshifted plasma and in some positions (pixel 3) increased intensity. Then, as time passes, the spectral profiles mature into the structure noted in Figure 4.5, with pixels to the north (4 and 7) and south (6 and 9) displaying strongly redshifted plasma and broader line widths and pixels in the center (nearer to the loop tops) displaying spectral lines that are narrower, more intense, and generally stationary. We additionally note that the Si IV profiles of many pixels (e.g. pixels 4, 6, 7, and 9) generally possess significant redshifted wings and/or multiple peaks which do not conform to the standard single Gaussian spectral line profile.

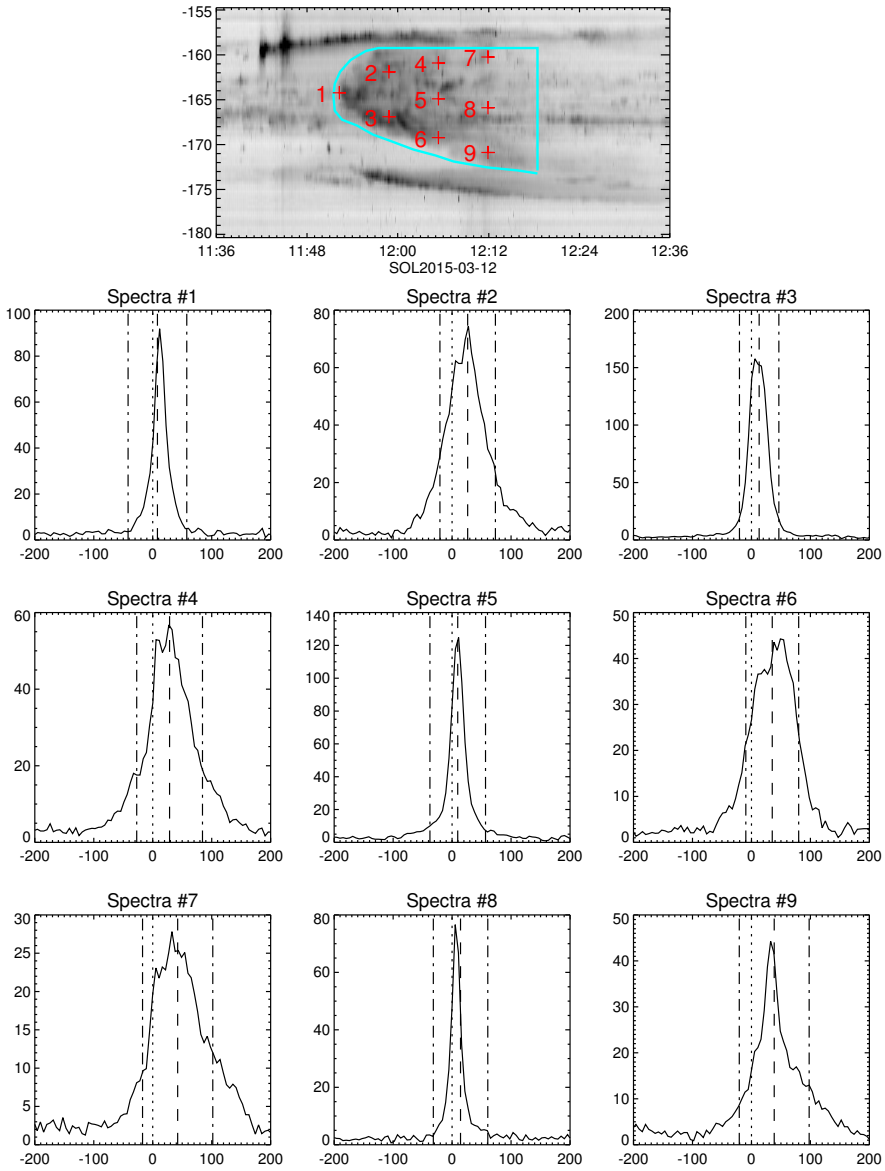


Figure 4.7. Si IV 1402.772 Å spectral lines for nine different pixels selected from within the bullet defined above. The Si IV 1402.772 Å intensity stack plot from Figure 4.6 and the cyan bullet contour is provided at top for context, with the nine selected pixels indicated by the "+" symbols and labelled "1"–"9". The x-axis for each spectral plot is in km s^{-1}, calibrated to the Si IV 1402.772 Å rest wavelength (indicated by the vertical dotted line). Note that the times for pixels 2–3, for pixels 4–6, and for pixels 7–9 are identical within each of those three sets. The vertical dashed and dash-dotted line are the Doppler velocity and line width, respectively, as described in Section 4.4.3.

In discussing Figures 4.5 and 4.7, we have only addressed qualitative features of the spectral data. To facilitate a quantitative analysis, we first select the wavelength range 1401.837 Å to 1403.707 Å ($\pm$200 km s^{-1}) and set a lower data bound of 5 DN s^{-1} (to eliminate the background) to create a reduced data set for each pixel. We then use the SSWIDL routine `moment` to extract the first four statistical moments of the reduced data. We have opted for this method rather than fitting the data with Gaussian profiles because, as mentioned above, the spectral lines for many pixels have significant spectral wings that are not single-Gaussian, and multiple Gaussian profiles introduce bookkeeping difficulties in consistently tracking components. In Figure 4.7 we have plotted the first two moments for the data in each plot, with the mean $\bar{v}$ as the vertical dashed lines and the standard deviation σ (actually $\bar{v} \pm \sqrt{2}\sigma$) as the vertical dash-dotted lines. We note that, for all pixels, the mean tracks very closely with the spectral peak, and we shall thus refer to the mean velocity simply as "the Doppler shift" of that pixel. Likewise we shall refer to the variance quantity $\sqrt{2\sigma}$ as "the line width", even though in some pixels (e.g. pixel 1) it actually appears to be somewhat wider than the actual line width (acting as an upper bound).

We can now examine the evolution of the Si IV 1402.772 Å spectral line for the bullet. In the upper plot of Figure 4.8 we show a time-distance stack plot (same pixels as Figure 4.6) for the Doppler velocity found using the above analysis. The bullet pixels are indicated with the cyan contour, and the velocity scale is given

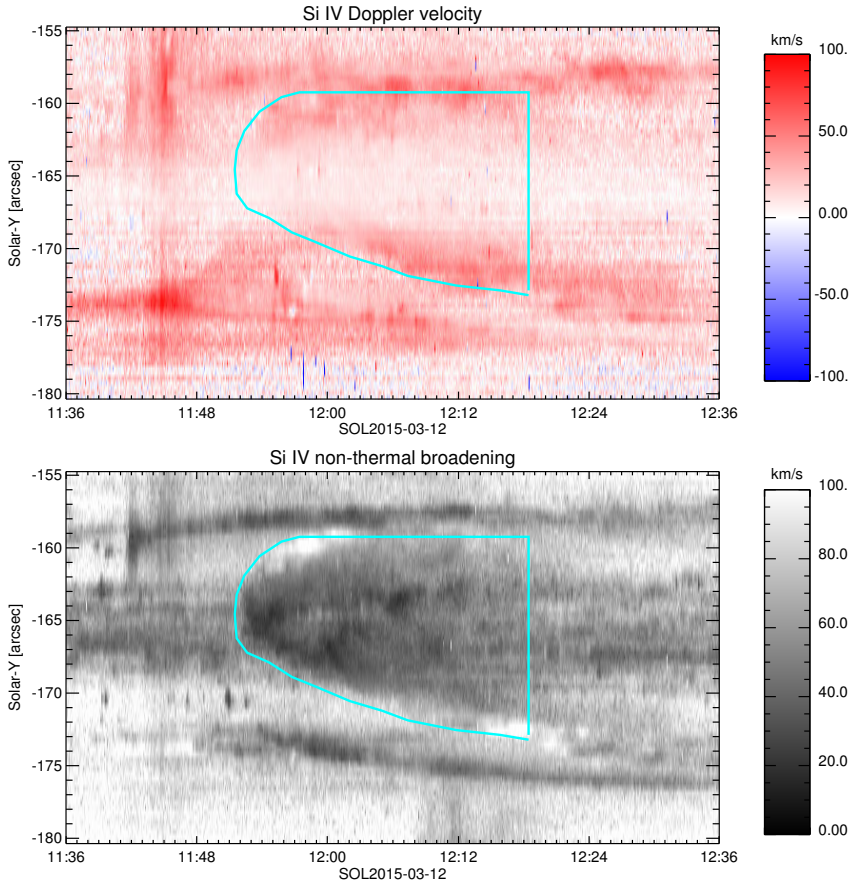


Figure 4.8. Time-distance stack plots showing the evolution of the Doppler shift (upper plot) and NTB (lower plot) for the Si IV 1402.772 Å spectral line, as described in Section 4.4.3. The x-axis for each plot is in UT, and the velocity color tables are shown at right of each plot. The bullet is indicated in each plot by the blue contour.

at right. We immediately note the strong redshifts in the north and south at the positions of the ribbons observed in Figure 4.6. These redshifts appear at all times for the ribbons, indicating that even early in the flare the Si IV plasma at $\log T = 4.8$ is flowing down towards the footpoints characteristic of chromospheric condensation flows. Within the bullet we observe that the plasma located near the center (near $-165''$) is stationary, whereas plasma located farther north and south of the center becomes increasingly redshifted towards the edges reaching Doppler redshifts of 40–50 km s^{-1}. Interestingly, the sound speed in a $\log T = 4.8$ plasma (as for Si IV) is 50 km s^{-1}, and thus the flows near the loop footpoints at the edge of the bullet are approaching supersonic.

We also calculate the non-thermal broadening (NTB) for Si IV 1402.772 Å, given by

$$\sigma_{nt} = \sqrt{\sigma^2 - \sigma_{th}^2 - \sigma_{inst}^2}, \tag{4.1}$$

where σ is the total $1/e$ line half-width, $\sigma_{th} = 6.86$ km s^{-1} is the thermal broadening and $\sigma_{inst} = 3.9$ km s^{-1} is the instrumental broadening for Si IV 1402.772 Å (De Pontieu et al., 2015). The calculated NTB is shown in the lower plot of Figure 4.8, with the bullet again indicated by the cyan contour and the scale shown at right. Note specifically here that white indicates the broadest line, and black the narrowest. However, due to the moment analysis method used, spectral profiles with significant background emission would produce a very large variance, and thus result in a large

apparent NTB, despite no Si IV line being present. However, for most pixels within the bullet, we find the NTB varies between 10–60 km s^{-1}. This value is somewhat higher than the previously reported 15–20 km s^{-1} NTB for Si IV in active regions (De Pontieu et al., 2015), although NTB of 60–80 km s^{-1} have been reported for other TR temperature spectral lines (e.g. He II, O VI) during flares (Milligan, 2011).

4.4.4. Plasma Density

It has been well established that the O IV 1399.780 Å and O IV 1401.157 Å lines, included in the Si IV 1402.772 Å passband, are a density sensitive line pair for chromospheric plasma at $\log T = 5.2$ (Flower & Nussbaumer, 1975; Keenan et al., 2009). Thus, for the approximate density range $10^8 < n_e < 10^{13}$, the ratio of spectral intensities for these lines correlates in a one-to-one manner with the total electron number density n_e. Although the densities found using this method are technically only valid for that temperature, it is a effective method of estimating the density of the plasma recorded by the pixel. To find the densities, we first consider a wavelength band of 0.5 Å on each side of the two O IV lines, corresponding to $N = 38$ or 39 data bins in each band, as well as a "continuum" band λ_{cont} from 1403.705 Å and 1404.640 Å (taken to be the generally flat zone between the Si IV 1402.772 Å line and the O IV 1404.806 Å line). Using the continuum band, we calculate a median continuum intensity I_{cont} by first finding the median of the data over the band and then multiplying by the number of spectral bins N. We then sum over each of the

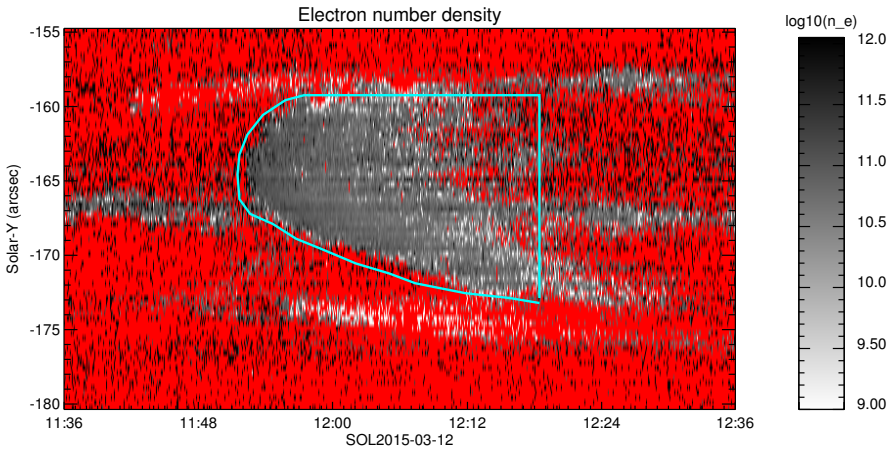


Figure 4.9. Time-distance stack plot showing the evolution of the plasma density within the bullet, derived from the ratio of the O IV spectral intensities, as described in Section 4.4.4. The x-axis for each plot is in UT, and the density color table is shown at right. The bullet is indicated by the blue contour.

O IV bands and subtract the continuum intensity I_{cont} to obtain absolute intensities I_{1400} and I_{1401} for the two spectral lines.

In many pixels one or both of the O IV lines is too weak to be reliable. We set a lower bound criterion $(I_{1400}, I_{1401}) > 40.0$ (this corresponds to approximately 1 DN s^{-1} above the continuum per data point), and any pixels failing this criterion are flagged as "unreliable". For all other pixels, we calculate the ratio $R = I_{1400}/I_{1401}$ and use a look-up table based on the results from Keenan et al. (2009) to obtain the electron number density for that pixel. In Figure 4.9 we show the resulting densities, in RLBW, for the same range of positions and time as for Figure 4.6. The unreliable pixels are colored red, and all other pixels are gray-shaded according to the color bar on the right. The bullet is again indicated by the cyan contour. Note that the vast

majority of pixels outside the bullet have O IV lines that are too weak to be reliable; however, within the bullet, and especially early and to the south, we find that a significant majority of pixels ($\sim$85.5%) are reliable. Of those reliable bullet pixels, we find that $\sim$5.6% have densities of $n_e > 10^{12}$ cm^{-3} (pure black pixels) and $\sim$5.7% have densities of $n_e < 10^{9}$ cm^{-3} (pure white pixels). Finally, $\sim$88.7% of reliable bullet pixels were found to have densities in the range 10^{9} cm$^{-3} \leq n_e \leq 10^{12}$ cm^{-3} (we will refer to these as "good" pixels).

A visual inspection of the good pixels in Figure 4.9 reveals that the majority are shaded in the mid-to-light gray range, especially during the first half of the bullet evolution, centered around a density of 10^{11} cm^{-3}, which is very similar to expected values for flare loops. We confirm this impression by calculating the median of the densities for the good pixels, which yields $n_e \approx 10^{11}$ cm^{-3}. We also note that the density within the bullet tends to be higher ($>10^{11.5}$ cm^{-3}) at earlier times than at later times; this is particularly notable for pixels in the lower right portion of the bullet, where the density in many pixels is below $10^{10.5}$ cm^{-3}, indicating that the density along the loop legs is decreasing somewhat over time. Unfortunately, the presence of unreliable pixels in the middle and upper right of the bullet (especially after 12:12 UT and north of $-167''$) somewhat obscures the later density evolution for portions of the loops. However, we recall that the "C"-shaped features in the spectral data have fully developed well before this time, and we note that between 12:00 UT

and 12:05 UT (when the "C" spectral feature is most apparent) the density is fairly uniform along the slit. Therefore, based on these observations, we conclude that the density at $\log T = 5.2$ may be reasonably approximated as constant, in both space and time, within the loops with a value of $n_e \sim 10^{11}$ cm^{-3}.

4.4.5. Cooling Time

As noted in Section 4.4.2, the loop emission appears first in Fe XXI and subsequently appears ∼11 minutes later in Si IV and O IV. The similar spatial location and appearance of the intensity stack plots in Figure 4.6 suggests that the Si IV emission originates from the same evaporated plasma as the Fe XXI emission, which has subsequently cooled into the cooler passband. Further, the nearly constant density in the loops (at early times) suggests that the cooling process is approximately isovolumetric. To estimate the cooling time, therefore, we recall from Aschwanden (2005) that the radiative and conductive cooling times (in seconds) are given respectively by

$$\tau_{\rm rad} = \frac{m_p c_v T}{n_e \Lambda\left(T\right)} = \left(3.4 \times 10^3\right) \frac{T^{3/2}}{n_{\rm e}} \tag{4.2}$$

and

$$\tau_{\rm cond} = \frac{L^2 n_e m_p c_v}{\kappa_0 T^{5/2}} = \left(3.7 \times 10^{-10}\right) \frac{n_{\rm e} L^2}{T^{5/2}}. \tag{4.3}$$

where T is the plasma temperature (in K), $n_{\rm e}$ is the electron number density (in cm^{-3}), and L is temperature gradient length scale (in cm); we have also defined the proton mass m_p, the heat capacity at constant volume c_v, the conductive coefficient $\kappa_0 =$

1.1×10^{-6}, and the radiative loss function $\Lambda(T) = (1.2 \times 10^{-19})\, T^{-1/2}$ (Aschwanden, 2005). For our purposes, we will approximate the temperature gradient length scale as the loop half-length. From inspection of Figure 4.3 (which best shows the coronal loops) we find that the footpoint separation for the loops which cross the slit is about 21.7″. As this observation was relatively close to disk center at the time of the flare, for the purposes of this study we will adopt a conversion factor of 730 km arcsec^{-1} to obtain a footpoint separation of ∼15.8 Mm and a loop half-length (assuming a elliptical loop with eccentricity $e = 0.8$, see Section 4.5) of ∼10.1 Mm. From Equations (4.2) and (4.3) we note that, for a 10.1 Mm loop that begins at ∼11 MK at density ∼10^{11} cm^{-3}, the conductive cooling time is significantly shorter than the radiative cooling time and will dominate the energy losses. However, by the time the loop plasma has cooled to the Si IV and O IV passbands, it is the radiative energy losses that dominate. To estimate a timescale for the overall cooling from the Fe XXI to the Si IV passband, we equate these two timescales and solve for T. This yields an approximate crossover temperature, T^*, at which the two energy loss processes are approximately equal, given by

$$T^* = \left(5.7 \times 10^{-4}\right) \sqrt{n_e L}. \tag{4.4}$$

For a loop as described above, this yields a crossover temperature of $T^* \approx 5.7$ MK, and substituting back into Equations (4.2) or (4.3) above gives a timescale for the

loop cooling from the Fe XXI passband to the Si IV and O IV passbands of $\tau^* \approx 7.8$ minutes, which is somewhat faster than the observed timescale.

The above estimate is obtained by considering each mechanism independently. The actual cooling process involves both mechanisms acting together, governed by the energy equation for a plasma (Aschwanden, 2005),

$$\frac{dT}{dt} = -\frac{T^*}{\tau^*}\left[\left(\frac{T}{T^*}\right)^{-3/2} + \left(\frac{T}{T^*}\right)^{5/2}\right], \tag{4.5}$$

for T^* and τ^* as defined above. We can solve this approximately for the cooling timescale by rearranging and integrating to obtain the relation

$$\int_0^{\tau_{\rm cool}} dt \approx -\int_0^{\infty} \frac{dT}{(dT/dt)} = \tau^* \int_0^{\infty} \frac{dx}{x^{-3/2} + x^{5/2}}, \tag{4.6}$$

where we have substituted $x = T/T^*$. Numerically integrating the final relation above, we obtain $\tau_{\rm cool} \approx 0.85 \cdot \tau^* \approx 6.6$ minutes.

One final note regarding the cooling process: note that the radiative time scale, given in (4.2), matches the sound-transit time,

$$\tau_{st} = \frac{L}{c_s} = \left(5.9 \times 10^{-5}\right) \frac{L}{T^{1/2}}, \tag{4.7}$$

when each is roughly $\tau = 90$ s at $\log T = 5.4$. Once the temperature falls below this it enters a phase of catastrophic cooling (Cargill & Priest, 1982). In this phase the pressure balance can no longer be maintained along the loop and the cooling plasma can be expected to fall downward under gravity, giving rise to a free-fall acceleration of the plasma.

4.5. Synthetic Spectra

The structure of Doppler shifts within the bullet, shown in Figure 4.8, indicates that the plasma within the flare loops, seen in Figure 4.3, is flowing down the loops on either side from the loop tops towards the footpoints. This is in contrast to a siphon flow, which would presumably display blue-shifts along one side of the loops. We also recall from Figures 4.3 and 4.5 that the coronal loops seen in 171 Å and 1400 Å cross the slit at an angle of 20° to 30°, and thus technically the Doppler shifts we observe along the north–south axis are from different loops. However, the close spacing and similar visible geometries of the loops means that we are sampling the Doppler shift for each loop at sequential positions along the loop geometry, supported by the smooth transition from stationary to redshifted spectral lines moving north and south from loop center. Also recall that, in Section 4.4.5, we found that the densities within the bullet, and hence across each of the sampled loops, are very uniform, supporting the idea that the loops are relatively similar in their evolution.

We therefore consider a simplified model in which the observed Doppler shifts are treated as resulting from flows along a single flare loop, which is then sampled at various positions along the SG slit. We will assume that the flare loop geometry may be approximated by a static ellipse with eccentricity $e = \sqrt{1 - 4h^2/d^2}$, where h is the maximum loop height and d is the footpoint separation. From Section 4.4.5, we recall that the footpoint separation was ∼15.8 Mm. In Panel (a) of Figure 4.10 we

show the height profiles for two loops with eccentricities $e = 0.0$ (circle, dashed line) and $e = 0.8$ (ellipse, solid line), which have maximum loop heights of $\sim$7.9 Mm and $\sim$4.8 Mm respectively. These are side-on views of the loops, with the north–south footpoint separation (in Mm) on the x-axis and the loop height (in Mm) on the y-axis, and the observer would be located above looking down. Note that we are *not* suggesting that these two loops exist together as shown; although that might indeed be the case, we are simply considering two possible loop geometries separately.

We will further make the assumption that the flows we are observing represent plasma that begins at rest near the loop tops and falls freely under gravity down the sides of the loops. The first point is generally supported by our observation of strong Fe XXI emission at the loop tops which does not display any significant Doppler shift, which is followed later by the "C"-shaped redshifts in Si IV and O IV. In Panels (b) and (c) in Figure 4.10 we show the velocity profiles for the full velocity (dashed lines) and Doppler velocity component (solid line), for each of the two loops $e = 0.0$ (Panel (b)) and $e = 0.8$ (Panel (c)). Here note that the x-axis is velocity (in km/s) and the y-axis corresponds to the x-axis in Panel (a). We also note that, at this stage, the Doppler component of the velocity for both loops is significantly more "C"-shaped than the full velocity is, an indirect representation of the elliptical loop shape on the angle of the plasma velocity to the observer.

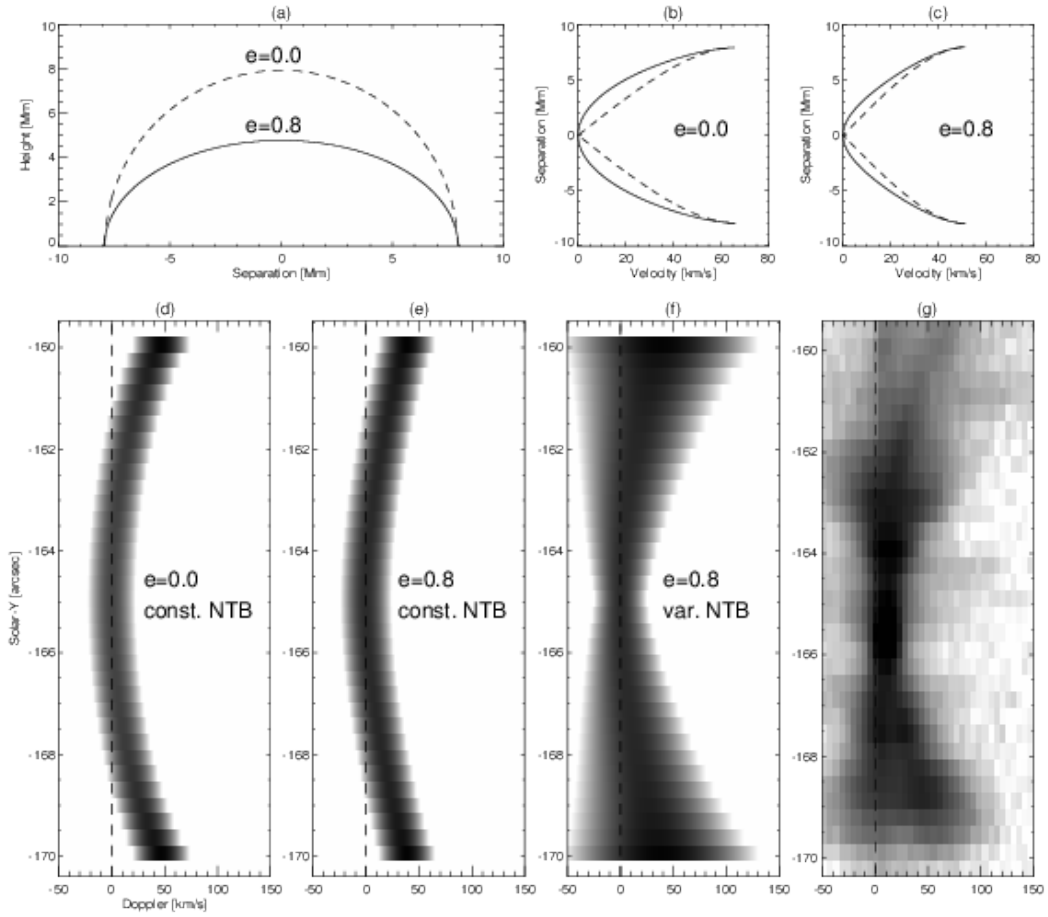


Figure 4.10. Model loops and synthetic spectra as described in Section 4.5. (a) Two possible loop geometries, with eccentricities e=0.0 (dashed line) and e=0.8 (solid line). (b) Free-fall velocity (dashed line) and Doppler component (solid line) for the e=0.0 loop. (c) Free-fall velocity (dashed line) and Doppler component (solid line) for the e=0.8 loop. (d) Synthetic spectra for the e=0.0 loop and constant NTB model. (e) Synthetic spectra for the e=0.8 loop and constant NTB model. (f) Synthetic spectra for the e=0.8 loop and scaled NTB model. (g) Si IV 1402.772 Å spectral data from 12:03:16 UT displaying "C"-shaped redshifts (reprinted from Row 4 of Figure 4.5).

To construct our synthetic IRIS spectra, we first construct a synthetic Si IV 1402.772 Å spectral line for every point along the loop of the form

$$I(\lambda) = \exp\left[-\left(\frac{\lambda - 1402.772 - \Delta\lambda}{\sigma_{th}^2 + \sigma_{inst}^2 + \sigma_{nt}^2}\right)^2\right], \tag{4.8}$$

where $\Delta\lambda = 1403.772 v_{dop}/c$ is the Doppler shift and where $\sigma_{th} = 6.86$ km s^{-1} and $\sigma_{inst} = 3.9$ km s^{-1} as given above. We use two different models for the NTB σ_{nt}. The first is a constant NTB $\sigma_{nt} = 12.0$ km s^{-1} (chosen to match the NTB of the central pixels in the bullet), and the second is a scaled NTB given by

$$\sigma_{nt} = 12.0 + 48.0\frac{v}{\max(v)} \tag{4.9}$$

which scales as the total flow velocity along the loop and yields a maximum NTB of 60 km s^{-1} near the footpoints. We next construct synthetic IRIS pixels by first divided the loop into 35 equal-sized bins (in Solar-Y, i.e. along the x-axis in Panel (a) of Figure 4.10), corresponding to the ∼35 IRIS pixels wherein we observe the "C"-shape. We weight each synthetic spectral line by the appropriate emission measure $EM = n_e^2 \cdot dz$, where dz is the size of each segment of the loop (which is larger near the ends due to the projection of the uniform grid in Y onto the elliptical loop) and $n_e = 10^{11}$ cm^{-3} is the uniform loop density inferred above. Finally, we sum the weighted spectral lines over each of the 35 bins and normalize the result across all bins to a maximum intensity of 300 DN/s, corresponding roughly to the maximum intensities that we observe in the IRIS spectra for the "C".

The resulting synthetic spectra are shown in Panels (d)–(f) in Figure 4.10. In all three plots, the x-axis is Doppler shift in km s^{-1} and the y-axis is Solar-Y in arcsec, and the vertical dashed line represents stationary Doppler shift (exactly as for the spectra displayed in Figure 4.5). For comparison, we have also plotted in Panel (g) the Si IV 1402.772 Å spectral data from Row 4 in Figure 4.5 to show the characteristic "C"-shape on the same spatial and spectral scale as Panels (d)–(f). In Panel (d) we show the synthetic spectra for the $e = 0.0$ loop (dashed line in Panel (a)) with the constant NTB model. We note that something like the "C" shape in the observed spectra does indeed appear; however, we also note that the maximum Doppler redshift, at $-160''$ and $-170''$, is somewhat too high (>50 km s^{-1} rather than the observed 40–50 km s^{-1}, which is not surprising given the free fall flow speeds in Panel (b)), and that the broadening near the ends of the "C" is too narrow compared with the observations. Next, in Panel (e), we have plotted the synthetic spectra for the $e = 0.8$ loop (solid line in Panel (a)), also with the constant NTB model. Here we note the sight reduction in the maximum Doppler shift down to ∼40 km s^{-1}, as we would expect from the reduced maximum free fall flow speed seen in Panel (c). Once again, though, we note that the broadening at the endpoints is too narrow.

Finally, in Panel (f), we show the synthetic spectra for the $e = 0.8$ loop with the scaled NTB model described above. The most striking difference between this plot and the Panels (d) and (e) is the significantly enhanced broadening at the ends of

the "C". Since it results from the same flow velocity as Panel (e), the peak Doppler shifts at the north and south ends is again ∼40 km s^{-1}. If we compare Panel (f) to the Si IV 1402.772 Å passband spectra shown in Row 4 of Figure 4.5, we see that the synthetic spectra qualitatively matches the observed data quite well in many respects. There is, however one important exception; namely that the observed data has the highest intensity in the "C" near the center, as opposed to the synthetic data which has higher intensity at the north and south. In the synthetic data, this is because the EM weighting we applied is greater near the ends, as the segment length dz becomes longer. We will speculate on possible reasons for the discrepancy with the observed data in the Discussion below.

4.6. Discussion

In this paper we have presented the results of our analysis of an on-disk spectroscopic observation of flare loops using the IRIS instrument. We found that the fortuitous positioning of the SG over the flare loops provides coverage of three important phases in the evolution of the loops during the flare: the filling of the loop with hot plasma via chromospheric evaporation (which we did not focus on substantially); the subsequent cooling of the flare loop plasma back into chromospheric lines; and finally the loop draining as revealed in the distinct redshifted spectral profile. Although previous studies have investigated all three of these phases of flare loop

evolution individually (Brekke et al., 1997a; Czaykowska et al., 1999; Schrijver, 2001a; Winebarger et al., 2001, 2002), those observations suffered from significant limitations (e.g. off-limb loops or feature-tracking in imaging observations), and no study was able to capture all three phases from a single observation. Additionally, no study has attempted to construct a complete flow profile for a flare loop during draining; Figure 1 in Czaykowska et al. (1999) shows redshifts interior to the ribbons in the arcade region, but the authors did not explore these loop flows in depth or attempt to model them. To the best of our knowledge, therefore, our work represents the first time the spectral evolution of on-disk flare loops from evaporation to draining has been observed and interpreted by using a flow model to generate synthetic spectra.

We will briefly summarize our results. We used time-space stack plots of the IRIS SG Fe XXI 1354.067 Å and Si IV 1402.772 Å passbands to find an ∼11 minute delay between the appearance of the hot, initially blueshifted, Fe XXI line signifying evaporation and the cooler Si IV line that was seen to be redshifted along the loop, and to identify a bullet-shaped region of interest using the Si IV intensity. After noting that the Si IV 1402.772 Å spectral line displays inconsistent components and significant redshifted wings, we opted to use a moment analysis to determine the Doppler shift and the NTB of the Si IV 1402.772 Å line. As expected from the spectral images, we determined that the Si IV 1402.772 Å line displays ∼40 km s^{-1} redshifts near the loop footpoints and is stationary near the loop tops. We noted

significant NTB in the Si IV 1402.772 Å line, varying from ∼12 km s^{-1} near the loop tops up to ∼60 km s^{-1} to the north and south near the footpoints. We used the density-sensitive O IV line pair to determine the densities within the bullet, finding a roughly constant density in the loops of $n_e \approx 10^{11}$ cm^{-3} for times within the bullet, and we used this density to estimate the cooling time within the loops to be ∼6.6 minutes. Finally, we developed a simple model, assuming free-falling plasma along the loop and using the observed Doppler shifts and NTB to constrain parameters, to create synthetic spectra which are remarkably similar to the observed spectral images.

We note that our estimate in Section 4.4.5 for the cooling time between the ∼11 MK Fe XXI 1354.067 Å and the ∼80,000 K Si IV 1402.772 Å passbands is ∼40% shorter than we determined using the intensity stack plots in Section 4.4.2. However, it is not uncommon for theoretical cooling times to be significantly faster than observations, and our estimate is certainly within the correct order-of-magnitude. Additionally, in Section 4.4.2 we noted two emission brightening events which do indeed transition between the Fe XXI 1354.067 Å and Si IV 1402.772 Å stack plots with an ∼6 minute delay, indicating that our estimate may in fact be accurate for at least some portions of the loops.

One final point in our estimation of the cooling time that is worth remarking on is that we implicitly assumed that the plasma was stationary in the loop. In the presence of bulk plasma flows, which certainly is the case in this observation, there exists an

enthalpy flux along the loop that can add to or subtract from the total heat energy of the plasma (Bradshaw & Cargill, 2010). In the case of siphon flows, this means that energy can flow from one footpoint to the other, possibly maintaining the plasma temperature against the losses described above. In our observation, however, the flows are always directed away from the loop top and towards the footpoints, meaning that any energy transport by enthalpy flux will only contribute to the total losses and potentially decrease the cooling time from what we found above. However, as noted in Section 4.4.3, throughout the majority of the loop volume the Si IV 1402.772 Å redshifts indicate plasma flows that are subsonic at the line formation temperature ($<$50 km s^{-1} at 80,000 K), although the velocity may approach the sound speed near the footpoints. Subsonic flow velocities are too slow to contribute significantly to the total energy losses, and thus the flows do not likely affect the cooling timescale in our case.

There are also two significant open questions regarding our synthetic spectral model which we would like to address. The first concerns the scaled NTB model we developed to replicate the excess NTB near the footpoints in the observed Si IV spectra. At face value, we have no particular reason to choose the NTB model that we did, other than it makes the synthetic and observed spectra more similar. Nonetheless, the observed spectra do indeed show additional NTB nearer the footpoints, and we are left to speculate why this may be occurring. One reason that we might expect the

NTB to increase as the flow velocity increases is that there is more energy available to cascade down into turbulence, resulting in a greater NTB. If that were the case, then Equation (4.9) would be the simplest model for this dependence; other functional dependences, however, might also be proposed to model the excess NTB. Another possibility is that, as noted above, the flow velocity in Si IV near the loop ends does approach the sound speed. This implies that shocks may be forming near the footpoints, and that the observed excess NTB is due to the sharp velocity gradients across the shocks. The fact that the excess NTB appears to smoothly increase from loop top to footpoints, however, would seem to contradict that scenario.

The other open question, as mentioned at the end of Section 4.5, is the apparent discrepancy between the observed and synthetic spectral intensity structure. Recall that the intensity of the observed spectra are greater near the loop tops than at the footpoints, whereas our synthetic spectrum displays the opposite behavior. We noted that the synthetic spectral intensity is greater to the north and south due to the nature of the EM weighting we applied. We speculate two possible explanations for the discrepancy. First, it would be expected from mass conservation that the flows would reduce the plasma density in the loops near the footpoints, which would reduce the emission there. When we calculated the densities in the loops in Section 4.4.4, however, we noted that the density profile running north–south was relatively uniform, and did not show significant gradients near the ends, although even a slight

reduction in the density n_e would result in a more substantial decrease in the emission measure $EM \sim n_e^2$. The other possibility is the the plasma is becoming more optically thick near the footpoints closer to the ribbon. Unfortunately, this IRIS observation only recorded the Si IV 1402.772 Å passband and did not record the Si IV 1393.757 Å passband, meaning that checking the optical thickness using those lines is not possible. That being said, the central result of using an elliptical loop with free-fall plasma draining to model the observed spectra appears to work quite well in this case, and we believe this to be this first study to use such a model to interpret observed flare loop spectra during the draining phase.

In closing, we repeat our statement from the introduction that IRIS provides a unique platform for performing observations of on-disk flare loops during the evaporation/cooling/draining process. Our analysis of this observation has revealed one particular possibility for describing for this process, but leaves open significant questions regarding both the plasma cooling process and the NTB of chromospheric lines. We believe that additional spectroscopic observations with IRIS (perhaps using different observation modes) will be needed to resolve these issues, and to determine if the simple plasma draining model we developed in this case holds up to further scrutiny.

4.7. Acknowledgements

IRIS is a NASA small explorer mission developed and operated by LMSAL with mission operations executed at NASA Ames Research Center and major contributions to downlink communications funded by ESA and the Norwegian Space Centre. The author would like to especially thank Prof. Dana Longcope for his role as a graduate advisor during this research, and for his feedback on the manuscript. The author would also like to acknowledge Prof. Charles Kankelborg, Dr. Sarah Jaeggli, Prof. David McKenzie, and Bryan Joseph for helpful and productive discussions concerning this work. This work was supported by contract 8100002702 from Lockheed Martin to Montana State University.

5. DISCUSSION

In the Introduction to this dissertation, we formulated three open questions in the topic of plasma flows driven by solar flares. First, is it possible to use properties of the evaporation flows to infer physical parameters of the corona? Second, can the evolution of flare ribbons be used to diagnose dynamics of the reconnection? Third, and finally, are there observations of flare loop downflows that can be used to constrain models of the loop draining process?

We then proceeded, in the three chapters which form the bulk of this dissertation, to relate our results from three separate investigations into this topic. Each of these investigations attempts to answer, at least in part, one of our posited questions. In so doing, the body of research we have described combines to form a larger story arc on the evolution of flare loops, with each of the three investigations corresponding to a different phase in the formation and evolution of plasma flows within a solar flaring loop. The primary objective of all of these studies has been to investigate how these plasma flows influence observational properties of flare loops, either through simulations or by analysis of observations. A secondary goal has been to establish relationships between observational properties of flare loops and more fundamental physical parameters of the coronal conditions and reconnection properties.

We therefore would like to take this chapter as an opportunity to reflect briefly on the position each investigation occupies in the larger scope of solar flare physics.

To this end, we will summarize what we believe to be the main objective of each study and how we believe the results may be useful to the solar physics community. Additionally, as in any research, we encountered many issues along the way which we have left as open questions. We will therefore address what we believe to be the most critical unresolved issues for each of our investigations, and we will also present any speculations on potential resolutions. Along the way, we will state our opinions on potential future avenues of research, and in particular how we or other researchers may expand on the results of our investigations so far.

First, in Chapter 2 (published in Brannon & Longcope (2014)), we used the simulation code we developed to cover a parameter space of ambient coronal and post-shock flare temperatures, and we were able to extract power-law relationships between those physical parameters and parameters of the chromospheric evaporation which are (at least in principle) observable in flare loops using spectroscopic instruments. Previous simulation studies tended to focus on studying the results in detail for a single simulation, or on matching observed evaporation parameters for a particular flare (see, e.g., Nagai (1980), Cheng et al. (1984), MacNeice (1986), and Fisher (1986)). Our work thus introduced a potentially useful diagnostic tool for indirectly diagnosing fundamental flare parameters such as the ambient coronal temperature and reconnection angle, which are difficult to directly observe otherwise, by using somewhat more accessible properties of the evaporation flows.

We successfully used the results of our simulations to fit evaporation flow velocities from an observation performed by Milligan (2011), and we extracted quite reasonable values for both the pre-flare coronal temperature and the post-flare loop top temperature. However, when we attempted to fit data from other studies (e.g. Li & Ding (2011), Raftery et al. (2009)) we discovered that our results performed less than adequately. The exact reason for this failure was not evident at the time of publication, and remains unresolved. Our belief at the time was that there might be some impact on the chromospheric evaporation flow velocities by the so-called "magnetic canopy" at the loop footpoints. As the coronal flux tubes dive into the chromosphere, the cross-sectional area of the loops is constricted (a "nozzle"). The functional form of this canopy nozzle depends on the large-scale magnetic geometry of the region.

Preliminary work by the author showed that, depending on the location (relative to the transition region) and degree of constriction of the nozzle, the velocities of the chromospheric flows can be significantly altered, which may result in better fits to observable data. Unfortunately, with only two observable parameters (coronal and flare temperatures) it is impossible to develop invertible relationships as we did in Chapter 2. One possible method around this which we have considered is to calculate Doppler shifts for specific spectral lines, instead of the more general parameters we

used before, which might display trends we could exploit to determine the nozzle properties.

Next, in Chapter 3 (published in Brannon et al. (2015)), we used imaging and spectral observations of a flare ribbon from the Interface Region Imaging Spectrograph (IRIS) and the Solar Dynamics Observatory / Atmospheric Imaging Assembly (SDO/AIA) to determine properties of the reconnection current sheet. Specifically, the flare ribbon in our observation displayed a distinct quasi-periodic oscillation with a 180° phase difference between the position and Doppler velocity. We used these observations to determine that the flare loops were likely undergoing elliptical oscillations driven by a Kelvin-Helmholtz or tearing-mode instability in the reconnection current sheet. Observations of ribbon and footpoint motions have been used previously to diagnose the coronal reconnection (Schmieder et al., 1987; Falchi et al., 1997; Isobe et al., 2005; Miklenic et al., 2007), and particularly the reconnection rate and coronal electric field (Qiu et al., 2002). However, to the best of our knowledge, this work represents the first use of a flare ribbon observation to indirectly diagnose an instability in the corona, which has proven otherwise difficult by direct observation (Aschwanden et al., 1999; Ofman & Thompson, 2011).

Although a potentially significant result, at least two serious questions remained open at the time of publication. First, we observed a definite two-component profile to the Si IV spectral line, which at the time we attributed to plasma in two different

sets of loops which were in different phases of reconnection during the instability. However, both sets of loops showed similar brightening of the Si IV spectral line, and it is unclear what the mechanisms energizing the two loops were. We also note that, although we posited the Kelvin-Helmholtz and tearing-mode instabilities due to the fact that they both can produce elliptical motions, we did not do any further work to establish the mechanism by which the flare loops could be elliptically transported during the reconnection process. Further, the entire quasi-periodic oscillation displays a net phase velocity of $\sim$15 km s^{-1} down the ribbon, and it remains unresolved how either instability might give rise to this phase velocity. Additional 2-D modeling using simple simulations of these instabilities might uncover more details of this process.

Finally, in Chapter 4 (in preparation for publication), we used an IRIS observation of a near-disk center flare to determine the full footpoint-to-footpoint velocity profile for the flare loops in the post-evaporation draining phase of the flare. Although other studies have determined draining velocities in off-limb prominences using either image feature tracking or spectral observations, we believe that this is the first time such a velocity profile has been reported for on-disk flaring loops in the post-evaporation phase. This observation also represents a significant improvement in spatial resolution and time cadence of the entire evolution of a flare loop from formation through cooling to draining. We were able to use the IRIS density sensitive O IV line pair to determine the loop densities, and we found that the cooling time using

a combined conductive/radiative model was ∼60% the delay we measured between the initial Fe XXI and the subsequent Si IV emission (but still well within the correct order-of-magnitude). We culminated by using a simple free-fall calculation to produce synthetic spectral profiles for the loop plasma which match the observed data quite well, the first time, to the best of our knowledge, that such a model has been compared to flow velocities at such high spatial resolution.

In fairness, however, many aspects of that investigation represent only a preliminary understanding of the observed flows. One example is that our model only matched the IRIS spectra after the application of an *ad hoc* non-thermal broadening model to the spectral lines. We have speculated on possible mechanism which could produce this effect, including the possibility of shocks forming near the footpoints, but the fact remains that we do not understand why the lines are so substantially broadened at this time. Further, the intensity distribution of our synthetic spectra was the reverse of that for the observed data. We have speculated that there may be optical depth effects in play, but due to the particulars of the observation we have no way to definitively show whether that is the case. Finally, there is the fact that the only observational support for the elliptical loop profile we selected is the fact that it reduces the synthetic Doppler shifts to match the observed shifts. One suggestion would be to perform a magnetic field extrapolation for the flare loops in question,

which would either support our elliptical loop profile as reasonable, or show that the reduced velocities are due to some other effect.

In short, there remains substantial room for additional work in the field of plasma flows driven by solar flares, both in terms of theoretical understanding and in using new instrumentation to reveal previously unknown properties. Nevertheless, we believe that the research we have presented here provides significant new insights into the topic, and has answered the need for additional understanding even as it opens further questions. We therefore will simply conclude by expressing our hope that these results continue to find applicability in the field of solar flare physics.

REFERENCES CITED

Acton, L.W., Canfield, R.C., Gunkler, T.A., et al. 1982, ApJ 263, 409

Antiochos, S.K., Sturrock, P.A. 1978, ApJ, 241, 385

Antiochos, S.K. 1980, ApJ, 220, 1137

Antonucci, E., Dennis, B.R., Gabriel, A.H., et al. 1985, SoPh, 96, 129

Antonucci, E., Dodero, M.A., & Martin, R. 1990, ApJS, 73, 137

Aschwanden, M.J., Fletcher, L., Schrijver, C.J., et al. 1999, ApJ, 520, 880

Aschwanden, M.J. 2005, Physics of the Solar Corona, (Springer Publishing)

Aulanier, G., Pariat, E., Démoulin, P., et al. 2006, SoPh 238, 347

Bradshaw, S.J., & Cargill, P.J. 2010, ApJ, 717, 163

Brannon, S., Longcope, D. 2014, ApJ, 792, 50

Brannon, S.R., Longcope, D.W., & Qiu, J. 2015, ApJ, 810, 4

Brekke, P., Kjeldseth-Moe, O., Brynildsen, N., et al. 1997a, SoPh, 170, 163

Brosius, J.W., Davila, J.M., Thomas, R.J., et al. 1996, ApJS 106, 143

Brosius, J. W., & Phillips, K. J. H. 2004, ApJ 613, 580

Brosius, J. W., & Daw, A. N. 2015, ApJ 810, 1

Brown, J.C. 1973, SoPh 31, 143

Brueckner, P.K. 1981, in Solar Active Regions: A monograph from Skylab Solar Workshop III, ed. F. Q. Orrall (Boulder, CO: Colorado Associated University Press), 113

Canfield, R.C., & Gunkler, T.A. 1985, ApJ, 288, 353

Canfield, R.C., Zarro, D.M., Wülser, J.P., et al. 1991, ApJ, 367, 671

Cargill, P.J., & Priest, E.R. 1982, Geophys. & Astrophys. Fluid Dyn., 20, 227

Cargill, P.J., Mariska, J.T., & Antiochos, S.K. 1995, ApJ, 439, 1034

Carmichael, H. 1964, in Proc. of the AAS-NASA Symp., The Physics of Solar Flares, ed. W. N. Hess (Washington, DC: NASA), 451

Carrington, R.C. 1859, Monthly Notices of the Royal Astronomical Society, 20, 13

Cheng, C.C., Karpen, J.T., & Doschek, G.A. 1984, ApJ 286, 787

Cheng, X., Ding, M.D., & Fang, C. 2015, ApJ, 804, 82

Courant, R., Friedrichs, K., & Lewy, H. 1967, IBM J. 11, 215

Craig, I.J.D. & McClymont, A.N. 1976, SoPh 50, 133

Crank, J. & Nicolson, P. 1947, Proc. Camb. Phil. Soc. 43 (1): 50-67

Culhane, J.L., Phillips, A.T., Inda-Koide, M., et al. 1994, SoPh, 153, 307

Czaykowska, A., DePontieu, B., Alexander, D., et al. 1999, ApJ 521, L75

De Pontieu, B., Title, A.M., Lemen, J.R., et al. 2014, SoPh 289, 2733

De Pontieu, B., McIntosh, S., Martinex-Sykora, J., et al. 2015, ApJL 799, L12

Emslie, A.G. & Nagai, F. 1985, ApJ 288, 779

Falchi, A., Qiu, J., & Cauzzi, G. 1997, A&A 328, 371

Fisher, G.H., Canfield, R.C., & McClymont, S. 1985(abc), ApJ 289, 414

Fisher, G.H. 1986, Lec. Notes in Phys. 255, 53

Fisher, G.H. 1987, ApJ 317, 502

Fisher, G.H. 1989, ApJ 346, 1019

Fletcher, L., & Warren, H. P. 2003, 'Energy Conversion and Particle Acceleration in the Solar Corona', L. Klein (ed.), Springer Lecture Notes in Physics 612, 58

Fletcher, L., Pollock, J.A., & Potts, H.E. 2004, SoPh 222, 279

Flower, D.R., & Nussbaumer, H. 1975, A&A 45, 145

Fontenla, J.M., Avrett, E.H., & Loeser, R. 1990, ApJ 355, 700

Forbes, T. G., & Priest, E. R. 1984, SoPh 94, 315

Forbes, T.G., Malherbe, J.M., Priest, E.R. 1989, SoPh 120, 285

Foukal, P.V. 1978, ApJ, 223, 1046

Foukal, P.V. 1987, in Theoretical Problems in High Resolution Solar Physics II NASA-GSFC, 15

Foullon, C., Verwichte, E., Nakariakov, V. M., et al. 2011, ApJL, 729, L8

Freeland, S.L., & Handy, B.N. 1998, SoPh, 182, 497

Furth, H.P., Killeen, J., & Rosenbluth, M.N. 1963, PhFl, 6, 459

Gary, G.A. 2001, SoPh 203, 71

Guidoni, S.E. & Longcope, D.W. 2010 ApJ 718, 1476

Handy, B. N., Acton, L. W., Kankelborg, C. C., et al. 1999, SoPh 187, 229

Harra, L.K., Matthews, S., Culhane, J.L., et al. 2013, ApJ, 774, 122

Hirayama, T. 1974, SoPh, 34, 323

Hodgson, R. 1859, Monthly Notices of the Royal Astronomical Society, 20, 15

Ichimoto, K., & Kurokawa, H. 1984, SoPh 93, 105

Isobe, H., Takasaki, H., & Shibata, K. 2005, ApJ 632, 1184

Karpen, J.T., Antiochos, S.K., & DeVore, C..R. 1995, ApJ 450, 422

Keenan, F.P., Crockett, P.J., Aggarwal, K.M., et al. 2009, A&A, 495, 359

Kerr, F.M., Rose, S.J., Wark, J.S., et al. 2005, ApJ 629, 1091

Kliem, B., Karlický, M., & Benz, A.O. 2000, A&A 360, 715

Kopp, R. A., & Pneuman, G. W. 1976, SoPh 50, 85

Lemen, J.R., Title, A.M., Akin, D.J., et al. 2012, SoPh 275, 17

Li, Y. & Ding, M.D. 2011, ApJ 727, 98

Li, T., & Zhang, J. 2015, ApJL, 804, L8

Liang, H., Zhan, L., Xiang, F., et al. 2004, New Astronomy, 10, 121

Lin, J., & Forbes, T.G. 2000, Journal of Geophysical Research, 105, 2375

Longcope, D., Beveridge, C., Qiu, J., et al. 2007 SoPh 244, 45

Longcope, D.W., Guidoni, S.E., & Linton, M.G. 2009 ApJ 690, L18

Longcope, D.W. & Bradshaw, S.J. 2010 ApJ 718, 1491

Longcope, D.W. 2014, ApJ, 795, 10

Lysak, R.L., & Song, Y. 1996, Journal of Geophysical Research 101, 15411

MacNeice, P., McWhirter, R.W.P., Spicer, D.S, et al. 1984 SoPh 90, 357

MacNeice, P. 1986, SoPh 103, 47

Malherbe, J.-M., Tarbell, T., Wiik, J.E., et al. 1997, ApJ, 482, 535

Mathioudakis, M., McKenny, J., Keenan, F.P., et al. 1999, A&A Letter 351, L23

Miklenic, C. H., Veronig, A. M., Vršnak, B., et al. 2007 A&A 461, 697

Milligan, R.O., Gallagher, P.T., Mathioudakis, D., et al. 2006, ApJ 638, L117

Milligan, R.O. & Dennis, B.R. 2009, ApJ 699, 968

Milligan, R.O. 2011, ApJ 740, 70

Mignone, A., Bodo, G., Massaglia, S., et al. 2007, ApJS, 170, 228

Nagai, F. 1980, SoPh 68, 351

Nagai, F. & Emslie, A.G. 1984, ApJ 279, 896

Neupert, W.M. 1968, ApJ, 153, L59

Nishizuka, N., Asai, A., Takasaki, H., et al. 2009, ApJL 694, L74

Ofman, L., & Thompson, B.J. 1982, ApJL 734, L11

Parker, E.N. 1963, ApJS, 8, 177

Petschek, H.E. 1964, NASA Special Publication, 50, 425

Phillips, O.M. 1977, The Dynamics of the Upper Ocean (Cambridge: Cambridge Univ. Press)

Priest, E.R. 1982, Solar Magnetohydrodynamics (D. Reidel Publishing)

Priest, E.R. 1985 Rep. Prog. Phys. 48, 955

Qiu, J., Lee, J., Gary, D.E., et al. 2002, ApJ 565, 1335

Qiu, J. 2009 ApJ 692, 1110

Raftery, C.L., Gallagher, P.T., Milligan, R.O., et al. 2009, A&A 494, 1127

Russell, A. J. B., & Fletcher, L. 2013, ApJ 765, 81

Semenov, V.S., Volkonskaya, N.N., & Biernat, H.K. 1998, Phys. of Plasmas, 5, 3242

Schmieder, B., Forbes, T. G., Malherbe, J. M., et al. 1987 ApJ 317, 956

Schrijver, C.J. 2001a, SoPh, 198, 325

Schrijver, C.J. 2001b, in 11th Cambridge Workshop on Cool Stars, Stellar Systems and the Sun, ed. R. J. Garcia Lopez, R. Rebolo, & M. R. Zapaterio Osorio, ASP Conf. Ser., 223, 131, 131

Spitzer, L.Jr. & Härm, R. 1953, Phys. Rev. 89(5), 977

Sturrock, P. A. 1966, Nature, 211, 695

Sturrock, P.A. 1973, in NASA Spec. Publ., Vol. 342, ed. R. Stone & R. Ramaty (Greenbelt, MD: NASA), 3

Sweet, P.A. 1958, in IAU Symp. 6, Electromagnetic Phenomena in Cosmical Physics, ed. B. Lehnert (Cambridge: Cambridge Univ. Press), 123, 123

Tanaka, K. 1987, Publ. Astron. Soc. Japan, 39, 1

Tarr, L.A. 2013, "Energetic Consequences of Flux Emergence" (Ph.D. thesis)

Tian, H., Wuelser, J. P., Boerner, P., et al. 2014, "IRIS Technical Note 20: Wavelength Calibration"

Tsuneta, S. 1996, ApJ 456, 840

Uchimoto, E., Strauss, H.R., & Lawson, W.S. 1991, SoPh 134, 111

Vernazza, J.E., Avrett, E.H., & Loeser, R. 1981, ApJS 45, 635

Warren, H.P., & Warshall, A.D. 2001 ApJ 560, L87

Wiik, J.E., Schmieder, B., Heinzel, P., et al. 1996, SoPh, 166, 89

Winebarger, A.R., DeLuca, E.E., Golub, L. 2001, ApJ, 553, L811

Winebarger, A.R., Warren, H., Van Ballegooijen, A., et al. 2002, ApJ, 567, L89

Wülser, J.P., Canfield, R.C., Acton, L.W., et al. 1994, ApJ 424, 459

Zarro, D.M., Slater, G.L., & Freeland, S.L. 1988, ApJ, 333, L99

Zarro, D.M. & Canfield, R.C. 1989, ApJ 338, L33